UNIVERSITY OF SOUTHAMPTON

FACULTY OF ENGINEERING, SCIENCE AND MATHEMATICS

School of Ocean and Earth Sciences

On the heat budget in the equatorial Pacific in the $\frac{1}{4}$ of degree OCCAM simulation

by

Adriana M. Huerta-Casas

Thesis for the degree of Doctor of Philosophy

July 2006

Graduate School of the
National Oceanography Centre, Southampton

This PhD dissertation by

Adriana Mireya Huerta Casas

has been produced under the supervision of the following persons

Supervisor

Dr. David Webb

Chair of Advisory Panel

Prof. Martin Sinha

Member of Advisory Panel

Prof. Harry Bryden

UNIVERSITY OF SOUTHAMPTON

ABSTRACT

FACULTY OF ENGINEERING, SCIENCE AND MATHEMATICS

SCHOOL OF OCEAN AND EARTH SCIENCE

Doctor of Philosophy

ON THE HEAT BUDGET IN THE EQUATORIAL PACIFIC IN THE $\frac{1}{4}$ OF DEGREE OCCAM SIMULATION

by Adriana Mireya Huerta-Casas

Air-sea fluxes in the Tropical Pacific basin have a significant role on the global climate. The study of the key physical processes affecting the heat balance is crucial to improve our understanding of the ocean-atmosphere interaction. This thesis presents a study focused on understanding such processes within the Ocean Circulation and Climate Advanced Model (OCCAM). It concentrates on two main aspects of the region in a run of the $\frac{1}{4}$ degree OCCAM model: The first is an analysis of the volume transport of the main current system; the second is concerned with the physical processes affecting the heat balance. This analysis is carried out for a one year period.

From the volume transport analysis, an idealized sketch of the Tropical Cells in the model is presented. They exhibit a sharp downwelling centred at 5N in the northern branch of the East Pacific, while the southern branch downwelling extends over four degrees in latitude. Zonally, the transport in OCCAM is weaker than those reported using mooring datasets. Above the core of the EUC the meridional convergence in the central Pacific feeds the EUC as it flows eastward. Within its core the meridional convergence and the tilt of the EUC both contribute equally to the upwelling. Below the core, the tilt is the main contribution to the upwelling.

Using the 5-day archived dataset, I investigated the different components of the heat balance. The analysis showed that the use of the 5-day mean data ignores terms associated with high frequency fluctuations at shorter time scales. These high frequency processes are important in the overall heat balance within each subvolume, but are small compared with the net fluxes across each interface.

Using a weighted temperature analysis, I studied how the water changes its temperature as it flows, and the processes associated with such temperature changes. This analysis shows that the EUC increases its temperature due to vertical diffusion, equatorward advective heat flux and meridional fluctuations around the mean flow. Away from the equator, the currents cool as they mix with the colder zonal current system.

Vertical diffusion is analyzed at 1S, 1N and 4N in the east Pacific. This analysis shows that most of the time the vertical diffusion is dominated by the gradient of temperature; however, there are events in the top levels associated with small values of the Richardson number. In the equatorial Pacific, the main large instabilities are the Tropical Instability Waves, which occur during autumn. The model also shows instabilities during the first half of the year, associated with changes in the vertical gradient of temperature and velocity.

DECLARATION OF AUTHORSHIP

I, Adriana Mireya Huerta Casas,

declare that the thesis entitled

'On the heat budget in the equatorial Pacific in the 1/4 of degree OCCAM simulation'

and the work presented in it are my own. I comfirm that:

- this work was done wholly and mainly while in candidature for a research degree at this University;
- where any part of this thesis has previously been submitted for a degree or any other qualification at this University or any other insitution, this has been clearly stated;
- where I have consulted the published work of others, this is always clearly attributed;
- where I have quoted from the work of others, the source is always given. With the exception of such quotations, this thesis is entirely my own work;
- I have acknowledged all main sources of help;
- where the thesis is based on work done by myself jointly with others, I have made clear exactly what was done by others and what I have contributed myself;
- none of this work has been published before submission.

Signed: _____

Date: _____

Acknowledgements

I would like to credit the mexican government, through the Consejo Nacional de Ciencia y Tecnologia (CONACyT), for sponsoring my project and for its effort to invest in scientific education as an integral part of the country's development.

I am completely indebted to my supervisor Dr. David Webb for undertaking this project with me, his scientific advice and patience were an essential ingredient of this work. I am also indebted with Prof. Harry Bryden who encouraged me at various stages of my PhD. Without them I would have never got so far.

Many people have supported me during my project. I would like to thank Beverly De Cuevas, Dr. Andrew Coward and Jeff Blundell for their help in my many computer problems. Many useful discussions were ensued with George Nurser to whom I am thankful to.

Life would had not been as enjoyable as it was without my friends in Southampton Julia D'Arrigo, Raul Lopez, Sofia Lopez-D'Arrigo, Alan Hughes, Martin Gutowski, Violeta Sanjuan, Angela Landolfi, Sara Sorohuet, Asier, Sara Benetti, Florence Nedelec, Cris Barrio, Sinhue Torres, Sara Comelli, Taro Hosoe, Ale Salvin, Paolo Cipollini, Andrey Ak., Fco. Benitez, Moritz and many others. Thank you.

Countless nice moments I lived with my housemates (and friends) Rose Mary, Almudena Fontan, Guy Francis, Isabelle Mary, Stefania Schinaia, Jorg Frommlet and Michael Frenz. I would never forget such good times with you in Kent Road.

I am very happy to also have the support of my friends in Mexico: Erika Schinnerl, Francisco Nettel, Javier Santillan, Horacio Tapia, Diana Avella, Diana Navarro, Jose Zahoul, Tiber Ramirez, Mukuy Guevara, Alejandro Reyes, Miguel Rodriguez, Carlos Robinson, Brian Urbano, Margarita, Rosalba Roman and Adrian Iturriaga. And also *in memory* of 'Papayas', who changed my perception of life.

'You just need to keep going' is the phrase that took me to the end. A big thanks for this and many other encouraging phrases to Ben, your constant support is invaluable.

I found no words to express how grateful I am, principally to my Mum, Carmen; and also to my sisters Liliana and Teresita; and my Dad Enrique. Their love and support are part of this project. Thanks for shortening the distance between England and Mexico.

Contents

List of Tables

List of Figures

Chapter 1

Introduction

1.1 Motivation

A relatively small change in the sea surface temperatures (SST) in the Tropical Pacific can produce weather and climate anomalies over many regions of the globe. The atmosphere plays an important role in those SST changes. A case in point is the reasonably well understood ENSO phenomenon. This is a natural and quasi-periodic coupled ocean-atmosphere phenomenon responsible for patterns of the global circulation which are related to anomalous climatic phenomena in many continental regions around the globe (Philander, 1992).

The scientific community placed greater emphasis on the importance of ENSO to the world climate after the strong event that occured in 1982-83. Several efforts have been undertaken to improve the observational system in the tropical Pacific ocean (McPhaden et al., 1998) including the TOGA COARE experiment and the Tropical Instability Wave Experiment (TIWE).

Other important processes affecting the ocean - atmosphere system are the Madden-Julian oscillation (MJO) - an eastward propagating atmospheric signal, thought to be driven by ocean - atmosphere interactions over the Indian and western Pacific- and the Tropical Instability Waves (TIWs) - two bands of large meanders to the north and south of the equator which are known to be important in mixing the cold tongue waters away from the equator.

The exchange of internal energy between the warm pools of the tropical oceans and the overlying atmosphere is thought to play a central role on the evolving climate system of the Earth. Of particular interest are atmospheric interactions with the tropical warm water pools, as these regions mark sites of intense convection in the

tropical atmosphere, that in turn have profound influence on tropical winds (Walker, 1923, 1924; Bjerknes, 1969).

Westerly Wind Bursts (WWBs) which occur in the region affect all heat balance terms: radiative and turbulent surface heat fluxes, turbulent mixing and advection. As a consequence, they have potential impact on the evolution of longer period climate variability (Cronin and McPhaden, 1997).

To improve our understanding of ocean-atmosphere interactions it is essential to determine the physical processes that control the heat budget in the western equatorial Pacific warm pool and the eastern equatorial Pacific cold tongue. The processes determining heat transfer include advection by currents, absorption of solar energy and loss by evaporation. Understanding the intensity and character of these processes will help us to understand the full ocean-atmosphere interaction in the region.

1.2 Objectives of this study

An outstanding issue in the scientific community is to improve our understanding of ocean-atmosphere interaction. An essential point for this is to determine the key physical processes affecting the heat balance in the equatorial Pacific. The aim of this project is to learn about those physical oceanic processes involved. To reach this aim the following questions are addressed:

- What are the processes affecting the heat transport in the equatorial Pacific? What is the effect of the heat fluxes due to the diffusion processes? How do they vary throughout the year?

To achieve this, the Ocean Circulation and Climate Advanced Model (OCCAM) is used. The main objectives in using the model are:

- Determine how well does the OCCAM 5 day mean dataset capture the actual advective heat transport.
- Investigate the processes affecting heat transport in OCCAM.
- Describe the mean state of the ocean by studying the zonal, meridional, vertical and total advective heat flux, the heat flux due to mean currents, the heat flux due to instabilities and diffusion.

Chapter 2

The Tropical Pacific Mean State.

2.1 Atmospheric Mean Conditions

Major components of the large-scale atmospheric motion in the Tropics are the meridional Hadley Circulation, in which air rises near the equator and sinks in higher latitudes and the zonal Walker Circulation, in which air rises over the warm western tropical Pacific and sinks over the cold eastern tropical Pacific.

The cloudy regions where moist air rises and condenses are convective zones and occur principally over equatorial Africa, Central and South America, and the "Maritime Continent" of the western Pacific and southeastern Asia (figure 2.1). This zonal band of cloudiness just north of the equator in the Pacific and Atlantic Oceans is called the Intertropical Convergence Zone (ITCZ). The band of clouds that stretches southeastward across the southwestern tropical Pacific is the South Pacific Convergence Zone (SPCZ). The seasonal movements of these regions of intense convection over the Indian Ocean sector and western Pacific are along a line that runs in a southeastward direction from northern India to the southwestern tropical Pacific. During the summer of the Northern Hemisphere the ITCZ is strong all across the Pacific, meanwhile the South Pacific Convergence Zone is poorly developed. During the transition to the northern winter, the region of most intense convection moves southeastward so that by January the SPCZ is well developed while the ITCZ over the western Pacific has become weak. From April onward the intense convection moves back northwestward, the ITCZ strengthens over the western Pacific, and the South Pacific Convergence Zone weakens as it moves westward and equatorward (Trenberth, 1976; Meehl, 1987).

The eastern tropical Pacific and Atlantic Oceans are arid except within the ITCZ whose seasonal movements dictate seasonal rainfall variations. The east-west zone of

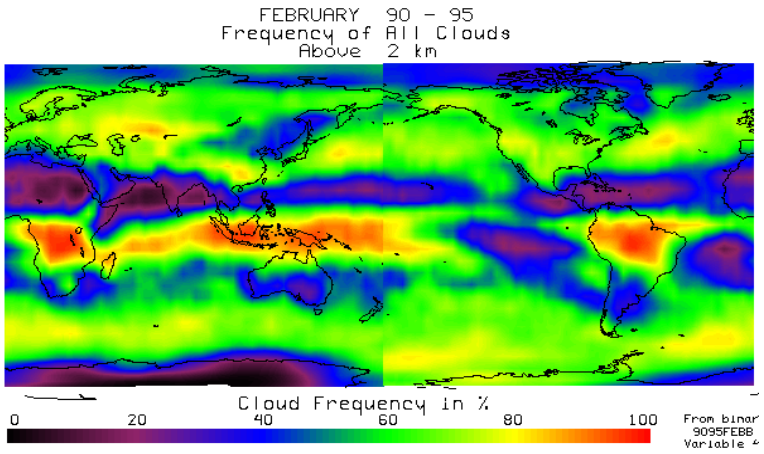

Figure 2.1: Cloud cover for February 1990-1995 according to the cloud climatology of Wisconsin HIRS. Cloud frequency clearing, shows the ITCZ along the equator and the maritime continent between south-east Asia and Australia. http://www.ssec.wisc.edu/

maximum annual mean rainfall coincides with the position of the ITCZ. The small latitudinal extent of the ITCZ produce sharp north-south gradients of rainfall.

The seasonal movements of the convective zones are associated with seasonal changes in the surface winds. Seasonal changes in the trade winds over the Pacific are associated with the movements of the ITCZ onto which the trades converges. The trades attain their maximum around 15 N and S. Equatorward of these latitudes the fluctuations in the intensity of the northeast and southeast trades are out of phase: the southeast trades are intense and the northeast trades are relaxed in September when the ITCZ is farthest north. The situation is reversed in March and April when the ITCZ is close to the equator.

The meridional component of the circulation in the tropics, the Hadley Circulation (figure 2.2), has two meridional cells. They are formed with moist air raising in the ITCZ, then diverging poleward in the upper troposphere and descending over regions to the north and south of the ITCZ. Superimposed on this meridional circulation is a zonal circulation, called Walker cells (figure 2.3), with ascending motion over the western tropical Pacific and descending motion over much of the eastern side of this ocean basin. The trade winds at the surface link these two regions.

Over the oceans the moist air raises where the sea surface temperatures (SST) are highest while dry air subsides where surface waters are cold. The warmest waters are in the western tropical Pacific and in a band of latitudes just north of the equator where the ITCZ is located. A SST of 27.5C seems to be a threshold for organized atmospheric convection, but it is not a sufficient condition as convection is absent in some areas which exceed 27.5C (Gadgil et al., 1984; Graham and Barnett, 1987). The

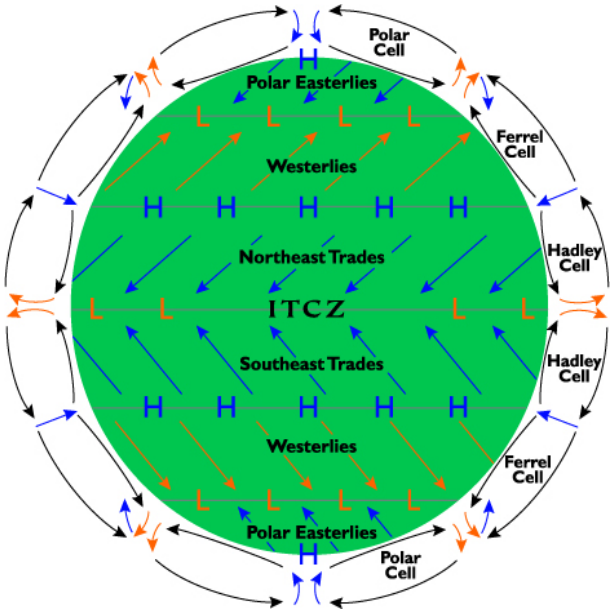

Figure 2.2: Idealized meridional atmospheric circulation.

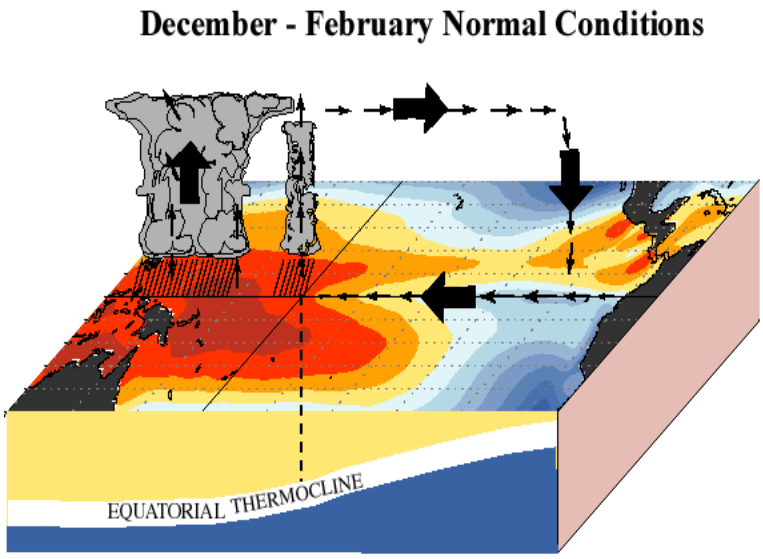

Figure 2.3: Idealized sketch of the Walker circulation in the atmosphere. It shows convergence over the Warm Pool region and convergence over the eastern Pacific. (From: http://www.cpc.ncep.noaa.gov/products/ analysis_monitoring/ensocycle/enso_cycle.shtml)

movements of the atmospheric convergence zones are such that they always remain over the warmest surface waters.

The zonal SST gradient signal is coupled to the surface air temperature and the pressure gradient drives the easterly Trade winds. These form the lower part of the atmospheric Walker circulation cell over the Pacific, with its ascending branch in the Western Pacific and the sinking branch in the Eastern Pacific. The cold water tongue and upwelling of the Eastern Pacific are not maintained only by the Trades, as they are constrained by the Andes, but are also forced by the southerly winds that are drawn north over the Equator by the Inter-Tropical Convergence Zone, which is permanently located in the Northern Hemisphere of the Pacific (Xie, 1998).

2.2 Ocean Mean Conditions

The distribution of temperature and salinity in the Equatorial Pacific Ocean is characterized by zonal asymmetry. The sea surface temperature (SST) in the west is the highest of the world oceans, attaining values over 29C. In the eastern Pacific the SST values can fall to 24C during certain periods of the year. Advection strongly influences SST over much of the tropical Pacific, especially in the eastern part of the basin. During El Nino, for example, the warming of the eastern tropical Pacific is caused by the eastward advection of warm surface waters associated with the elevation of the thermocline in the west and its deepening in the east. This warming by advection competes with cooling caused by upwelling (Philander (1990), p. 59). The prevailing trade winds drive poleward Ekman drift and hence induce equatorial upwelling that leads to a tongue of cold surface water along the equator. This cold tongue is pronounced in summer and autumn of the Northern Hemisphere when the easterly winds along the equator are intense, and is almost absent in spring, when the trades are weak. Since the vertical velocity component vanishes at the surface, mixing processes determine the extent to which upwelling affects sea surface temperatures. The upwelling zones are narrow but currents advect the cold surface waters over considerable distances.

The SST in the tropical oceans are influenced by the heat flux across the ocean surface, advection, upwelling and mixing processes. A change in the balance between these processes causes SST variations. On interannual and seasonal scales such a change in the balance reflects profound changes in the circulation of the entire tropical Pacific Ocean, which is determined primarily by the surface winds.

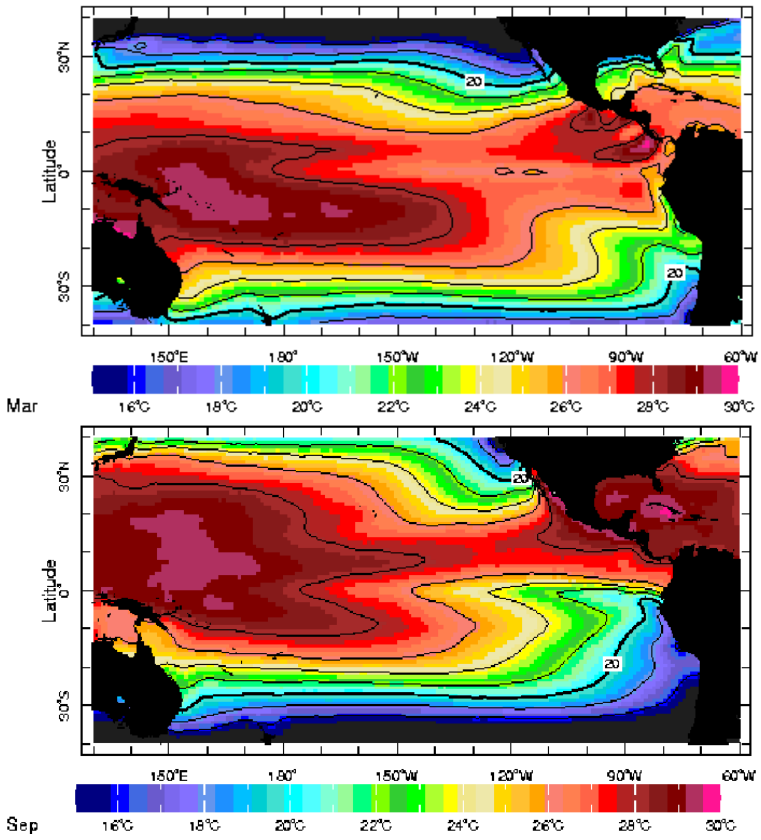

Figure 2.4: Climatological sea surface temperatures (in C) for the tropical Pacific, March (upper panel) and September (lower panel). (Reynolds and Smith, 1994)

2.2.1 The Warm Pool

The warmest sea surface temperatures (SST) in the global ocean are found in the tropical western Pacific Ocean and the equatorial Indian Ocean; with mean SSTs in excess of 28C, the western Pacific is also characterized by weak trade winds, and deep atmospheric convection (Bjerknes, 1969). The other important feature of the region, termed the 'Warm Pool', is that small variations in the SSTs (O(1C)) can result in dramatic shifts in global weather patterns (Palmer and Mansfield, 1984).

These facts have led to intense research in trying to explain the physical processes involved between the atmosphere and ocean, particularly in this region. A case in point of this effort is the TOGA-COARE experiment, whose goals were to describe and understand, in the warm pool region (Webster and Lukas, 1992):

- The principal processes responsible for the coupling of the ocean and the atmosphere;
- The principal atmospheric processes that organize convection;
- The oceanic response to combined buoyancy and wind-stress forcing; and
- The multiple-scale interactions that extend the oceanic and atmospheric influence of this region to other regions and vice versa.

Embedded in a longer period of enhanced meteorological and oceanographic monitoring, an intensive observation period (IOP) took place during November 1992 through February 1993. In this period, westerly wind bursts (WWBs) were observed, which are potentially important in triggering and sustaining EL Niño-Southern Oscillation (ENSO) events, and also provide the most energetic mechanism for maintaining the mixed layer in the western Pacific warm pool (Lukas and Lindstrom, 1991).

2.2.2 Westerly Wind Bursts in the Upper Ocean Heat Content.

Several authors (Lau and Chan, 1988; Nakazawa, 1988; Slingo et al., 1999) have associated the high frequency westerly winds with the active phase of the MJO in the western Pacific due to the occurrence of enhanced low-level convergence. They can also result from individual and paired tropical cyclones (Keen, 1982) and mid-latitude cold surges from the Asian continent (Harrison, 1984). Westerly Wind Bursts (WWBs) cause a deceleration of the easterly Trades and can lead to a complete reversal of westerly surface flow. WWBs mainly occur during the boreal winter and spring and last from 2

days to a couple of weeks (Harrison and Giese, 1991), reaching speeds from $2ms^{-1}$ to $10ms^{-1}$ (Delcroix et al., 1993).

The processes controlling the upper ocean heat content are essential for understanding the atmosphere-ocean interaction. The response of the ocean to the WWBs which occurred between September 1992 and February 1993 is an example of these processes, which typically last for less than one week (Webster and Lukas, 1992).

The WWBs have a meridional scale of a few hundred kilometres and a zonal scale of more than 1000 km. They can generate strong equatorial waves and can strongly affect the air-sea interaction processes in the tropics. Smyth et al. (1996b) found that the WWBs occurring during December cooled the ocean's surface layer by about 0.8C; and following the wind burst, a sustained eastward surface current contributed to high current shear and turbulent dissipation rates at the top of the thermocline. Therefore, most of the heat transfer into the thermocline occurred after the wind burst had ended.

These wind anomalies generate an adjustment through equatorial waves that have the capability of rapidly transmitting the local response across the whole Pacific basin within timescales of a few months. Locally, WWBs lead to changes in the current structure above the thermocline including current reversals and associated horizontal pressure gradient reversals (Cronin et al., 2000).

Smyth et al. (1996a) pointed out that despite the low latitude of the COARE region, the Coriolis force plays a crucial role in the dynamics. The response of the surface currents to wind forcing is controlled by interference between the instantaneous wind stress and the oscillatory wake left by previous wind stress events. In addition, the wind stress variations on near-inertial timescales interfer both constructively and destructively with the wave response, exerting considerable influence on the observed currents. The dynamic response to the wind burst is dominated by wavelike motions in the near-inertial band. Usually rain forms a shallow, buoyant layer, that does not mix with the water below, except during infrequent strong wind events (Anderson and Weller, 1996). During the observed period, due to heavy precipitation, salt stratification tends to be strong in the upper waters of the warm pool (Smyth et al., 1996b). Strong salt stratification should tend to insulate the sea surface against mixing with the cooler water found in the thermocline (Lukas and Lindstrom, 1991). Advection appears to have been the dominant factor governing local salinity changes (Smyth et al., 1996b; Feng et al., 1998) and heat balances (Feng et al., 1998). Advection occurs both on short timescales associated with the passage of freshwater pools and on the longer timescales of the wind burst itself. Evaporation was the dominant surface cooling mechanism, even in rainy conditions. The meridional advection dominates over zonal and vertical

advection, acting to decrease temperature and increase salinity in the surface layer. The redistribution of heat caused by the ocean flow produces changes in the meridional gradient of sea surface temperature. These changes in temperature gradient have the potential of feeding back to the atmosphere (Richards and Inall, 2000).

2.3 Modes of Variability

2.3.1 El Nino - Southern Oscillation

The atmospheric pressure fluctuation over the western tropical Pacific and eastern Indian Ocean is coherent and out of phase with that over the southeastern tropical Pacific. This fluctuation is known as Southern Oscillation. This oscillation is associated also with major changes in rainfall patterns and the wind field of the tropical Indian and Pacific Oceans and is correlated with meteorological fluctuations in other parts of the globe (Walker, 1923, 1924, 1928; Walker and Bliss, 1937, 1931, 1930). The correlation between the various parameters establish that high surface pressure over the western and low surface pressure over the southeastern tropical Pacific coincide with heavy rainfall, unusually warm surface waters, and relaxed trade winds in the central and eastern tropical Pacific. This phase of the Southern Oscillation in known as El Nino. The Pacific Ocean alternates between this phase or its complementary one, refered to as La Nina. During the latter phase, the surface pressure is high over the eastern but low over the western tropical Pacific, while trades are intense and the sea surface temperatures and rainfall are low in the central and eastern tropical Pacific.

2.3.2 Madden - Julian Oscillation

The tropical atmosphere-ocean system exhibits variability on short time scales. At intraseasonal timescales, the Madden-Julian oscillation (MJO) is the primary mode of variability. It is an eastward propagating atmospheric signal characterized by multiple covariances between zonal wind, surface air pressure and temperature throughout the troposphere. It has a period of 40-60 days and consists of a low frequency atmospheric Kelvin/Rossby wave structure, which is best described as a large circulatory cell that is vertically coherent throughout the troposphere due to its deep convective activity (Madden and Julian, 1971, 1972). It is thought to be driven by ocean-atmosphere interactions over the Indian and western Pacific Oceans (Slingo et al., 1999). The intensity of MJO activity is correlated to the seasonal cycle, and its convective signal

is most active during the boreal winter and spring and it depends on the latitudinal distribution of warm SSTs. It turns out to be the main intra-annual fluctuation that explains weather variations in the tropics. It affects the entire tropical troposphere but is most evident in the Indian and western Pacific Oceans. The MJO involves variations in wind, SST, cloudiness and rainfall. It propagates eastward around $5ms^{-1}$ to the dateline.

2.4 The Equatorial Pacific Current System

The circulation of the tropical Pacific and Atlantic Oceans are characterized by alternating zonal currents: the westward flowing South Equatorial Current (SEC) straddling the equator, the eastward Equatorial Undercurrent (EUC) embedded within the SEC along the equator and the eastward North Equatorial Countercurrent (NECC) to the north.

The North Equatorial Countercurrent lies approximately between 3N and 10N. It flows counter to the prevailing trade winds with a typical surface speed of $50cms^{-1}$. This narrow current is sandwiched between the North and South Equatorial Currents, which are found north of 10N and to the south of 3N, respectively. The northern current is relatively weak, with speeds less than $20cms^{-1}$. Meanwhile the southern current has an intense core between the equator and 3N in which speeds can exceed $100cms^{-1}$. An eastward flowing South Equatorial Countercurrent in the neighborhood of 9S is usually present west of the date line in the Pacific but it becomes increasingly sporadic east of 180E (Merle et al., 1969).

In the east currents transport cold water that upwells along the American coast. Eastward flow coincides with the band of warm surface waters to the north of the equator. Sea surface temperatures are much lower in the eastern than western tropical Pacific Ocean except for a band of warm surface waters that extends across the width of the ocean basin just north of the equator. This sea surface temperatures pattern is strongly influenced by advection. The sea surface temperature patterns also reflect subsurface thermal gradients. Along the equator, for example, the decrease in sea surface temperature from west to east is associated with a shoaling of the isotherms.

The thermocline, the region of high thermal gradient, separates the warm surface waters from the colder water at depth. It has a depth of about 150m in the western Pacific and surfaces in the east. This slope implies an eastward pressure force in the upper ocean, if hydrostatic balance is assumed and pressure gradients in the deep ocean

are assumed to be negligible.

Away from the equator and below the directly wind-driven surface layer this pressure force induces equatorward geostrophic motion in both hemispheres according to the equation:

$$\rho f v = \frac{\partial p}{\partial x} \tag{2.1}$$

Here f is the Coriolis parameter, which changes sign when the equator is crossed and ρ is the density of the ocean. At the equator the Coriolis force vanishes ($f = 0$) and cannot balance the pressure force. The fluid that converges onto the equator can, in part, rise to the surface to sustain the divergent Ekman drift and can also accelerate eastwards, down the pressure gradient, thus contributing to the EUC in the equatorial thermocline. The EUC is observed below the wind driven westward surface layers and can attain speeds in excess of $150 cms^{-1}$. Its core is in the thermocline and extends vertically over a depth of approximately 150m. Although its width is only of the order of 300km, the current is continuous over a longitudinal distance of more than 10,000km in the Pacific.

The meridional motion in the tropical Pacific Ocean is poleward Ekman drift in the surface layers driven by the easterly winds and equatorward geostrophic motion at the depth of the thermocline. This circulation implies equatorial upwelling, which can be estimated from the divergence of the horizontal currents. In addition to intense equatorial upwelling there is strong downwelling in the adjacent region on the NECC (Hansen and Paul, 1987). Studies of chemical tracer distributions near the equator (Fine, 1983) indicate that the vertical velocity component has a large amplitude only in the upper 150m of the tropical oceans. This explains why the sea surface temperature is unaffected by equatorial upwelling in regions where the thermocline is deep, as in the western Pacific and Atlantic. The transport of the eastward NECC decreases in a downstream direction because the loss of fluid to downwelling and the Ekman drift across 3N. The downwelling is into the thermocline, where the motion is equatorwards, toward the EUC. There is a similar equatorward flow in the thermocline in the Southern Hemisphere.

Equatorial upwelling transfers the convergent fluid to the surface layers. This diminishes the transport of the EUC in a downstream direction- in the Pacific the transport decreases in the eastern half of the basin - and augments that of the westward SEC, which has poleward Ekman drift in its surface layers. The upwelling is most intense in the central Pacific but is strongly confined to the upper ocean and attenuates rapidly with increasing depth below 60m. The downstream decrease in the transport of the two

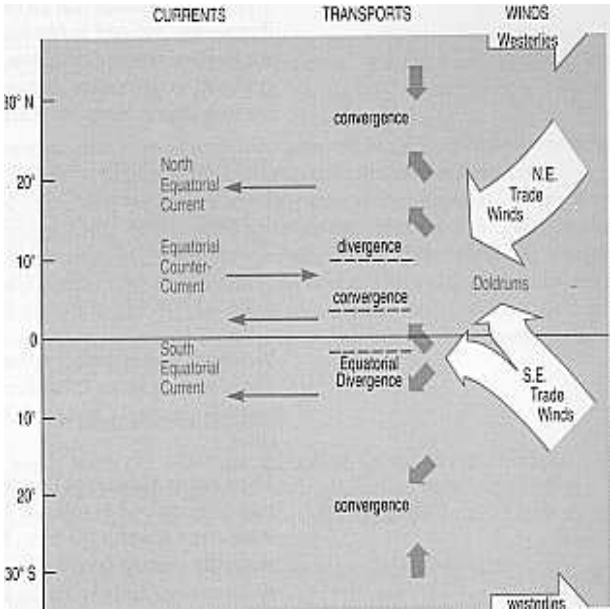

Figure 2.5: Schematic diagram of the equatorial current system.

eastward currents causes both to die out before they reach the eastern boundaries of the Pacific Ocean. The transport of the westward currents on the other hand, increases in the downstream direction. They must ultimately decrease before hitting land (Asia).

2.5 The Cold Tongue region

The eastern tropical Pacific is normally characterized by a tongue of cold water whose temperature can vary over 10C during its annual cycle (see figure 2.4). This pattern is maintained by the Walker circulation, where its descending part in the east coincides with the cold tongue location, figure 2.3. The appearance of cold water extends from the west coast of South America westward along the equator. During March the water is warm in the eastern Pacific and the SST is nearly symmetric about the equator, with cooler water at the equator as a result of equatorial upwelling. After April the upwelling becomes stronger and subsequently this cool water spreads over the southern hemisphere as a result of mixing processes.

The mechanisms governing the temperature and salinity field evolution in the cold tongue need better understanding. These include mixing processes as well as oceanic interactions with the atmospheric boundary layer structure. This region has an influence over the climate in the surrounding continents as well as remote impacts on the tropical Atlantic, South America (Moura and Shukla, 1981; Pezzi and Cavalcanti, 2001) and northwest Africa (Folland et al., 1986).

The importance of the eastern Pacific has increasingly being recognized. For instance the project Eastern Pacific Investigation of Climate Processes (EPIC) was carried out during the years 1998-2004 to investigate the climate and the coupled ocean-atmosphere system with a combination of modelling and observational studies.

It is believed that the extensive marine stratus deck off the west coast of South America acts to reflect a large fraction of the incident solar radiation, which would otherwise be absorbed by the ocean, consequently the ocean is not heated strongly here. This reinforces the cross-equatorial contrast in SST and intensifies the cross-equatorial Hadley cell circulation (Philander et al., 1996; Ma et al., 1996).

2.5.1 Tropical Instability Waves

The westward component of the south east trades induces upwelling where they cross the equator, forming the North Equatorial Front (NEF) between the cold equatorial tongue and warmer waters to the north. Each year in the late summer to fall, when the intertropical convergence zone migrates northward, the southeast trades accelerate the SEC and meridional oscillations perturbing the zonal currents are observed at periods of 15 - 35 days and wavelengths of 500 - 1500 km. These long wavelength oscillations of the NEF are the Tropical Instability Waves (TIW). They appear in the tropical Pacific as meanders of the EUC and SEC, meridional deformations of the NEF, and anticyclonic vortices and sea level highs in the SEC-NECC shear (Kennan and Flament, 2000) due to various instability mechanisms (Philander, 1976). A TIW signature is always observed when the meridional SST gradient at 140W is greater than 0.25C per 100km (Contreras, 2002). These waves grow north of the equator exhibiting their maximum variability around 2N where the meridional SST gradient is highest and propagate westward from the vicinity of the Galapagos Islands reaching a maximum around 120W and then decay to the west.

Between 2N and 5N, the surface layer gains heat from the zonal flow and loses heat from the meridional flow. High TIW energy values typically occur around October when the SEC and the NECC both become stronger and the eddy kinetic and potential energy production at 140W is noticeably larger (Baturin and Niiler, 1997). The effect of instability is to reduce the shear of the mean current and to warm the equatorial cold tongue. These calculations suggest that there exists a balance between energy production and dissipation in the TIWs.

The TIWs in the Pacific Ocean extend from 95W to 150-160W. The waves are anisotropic in the east-west direction with the most energetic region confined primarily

to the upper 100m of the ocean (Philander, 1985). Associated with the TIWs in the SST images are vigorous mesoscale eddies lying primarily between the equator and 7N (Flament et al., 1996).

The eddies rotate anticyclonically and propagate to the west. Propagation speeds range from 10 to 60cm/s, but the spatial structures of the eddies are rather similar. Eddies appear in July and persist through December of each year, except for El Nino years when almost no eddies are observed (Baturin and Niiler, 1997).

Luther and Johnson (1990) reported three distinct types of instabilities, each occurring at different times of the year. The first occurs during the boreal summer and fall and is due to the strong horizontal shear between the EUC and the northern branch of the SEC. The second occurs during the boreal winter and its energy source is primarily the mean potential energy associated with the equatorial SST front located between 3 and 6N. The third occurs during boreal spring and utilizes the mean potential energy associated with the thermocline tilt beneath the NECC. The TIW-induced heat flux north of the equator is comparable to long-term mean surface heat flux. (Hansen and Paul, 1984; Bryden and Brady, 1989).

In recent years a number of research programs have highlighted the importance of studying TIWs by numerical models and observations. The Tropical Instability Wave Experiment (TIWE) was initiated in the boreal spring 1990 aiming to understand the effects of these waves in the near-surface mass, momentum, heat and energy instabilities. The TIWE revealed the presence of a coherent vortex moving westward in the SEC-NECC shear zone between 2N and 7N (Kennan and Flament, 2000). In models and in observations, the TIWs induce large equatorward transport of heat, equivalent to or stronger than the effect of surface forcing (Vialard et al., 2001).

Chapter 3

The Analysis of Heat in the OCCAM Model

3.1 Introduction.

The oceans cover around 70% of the earth's surface; they provide a large reservoir for heat to the earth's climate system. The physical processes driving the currents and determining physical properties of sea water are numerous, complex and occur over a large range of space and time scales.

Ocean climate models are tools used to numerically simulate the large space-time variability which characterizes the ocean climate system. Realizing simulations of the physical system integrity requires the ability to accurately represent the various phenomena which are resolved and to parametrize those scale of variability which are not resolved.

Many techniques used in the meteorological field have been applied to solve oceanographic problems due to the similarities in understanding and simulating them. Particularly, for over twenty years, the use of computers to solve Navier-Stokes equations has been successfully applied to the ocean, and Ocean General Circulation Models (OGCMs) have become important tools in the study of the dynamics and physics of the ocean. The basic idea of numerical methods consists in discretizing differential equations on a three dimensional grid and computing the time evolution of each variable for each grid point. Ocean models are usually written in this finite difference form but spectral method are sometimes used.

Despite the similarities of the equations governing the ocean and the atmosphere, there is a large difference in their physical properties, so that the characteristic scales

in time and space of these two fluids are different. Oceanic structures are characterized by high and low pressure regions propagating across a turbulent fluid with time scales of about a month as compared with the two or three days in the atmosphere. The horizontal resolution needed to resolve the dynamics correctly must be of the order of the internal radius of deformation, which is around 30 km in the ocean and around 1000 km in the atmosphere. As a result the number of grid points in the horizontal plane is considerably larger in an ocean model. In order to ensure numerical stability, the time step is around 10 minutes in the atmosphere and around 1 hour in the ocean for the same time differencing scheme.

3.2 Ocean Circulation and Climate Advanced Model (OCCAM).

The OCCAM model is related to the Bryan-Cox-Semtner (Cox, 1984; Bryan, 1969; Semtner, 1974) ocean general circulation model. The model is based in the ocean 'primitive equations' (Bryan, 1969); its main difference from other ocean model types being the use of an Arakawa-B grid in the horizontal (Arakawa, 1966) and level surfaces in the vertical.

3.2.1 Primitive equations

The ocean is described with a good approximation by the Navier-Stokes equations, or primitive equations, along with a non-linear equation of state which couples the two active tracers (temperature and salinity) to the fluid velocity. The following scale assumptions need to be considered as well:

1. Spherical earth approximation: the geopotential surfaces are assumed to be spheres with gravity (local vertical) parallel to the earth's radius;
2. Thin-shell approximation: the ocean depth is negligible compared to the earth's radius;
3. Turbulent closure hypothesis: the turbulent fluxes (which represent the effect of small scale processes on the large-scale) can be represented in terms of large-scale features, such as large scale temperature or velocity gradients;
4. Boussinesq hypothesis: density variations can be neglected except in their contribution to the pressure field;

5. Hydrostatic hypothesis: the vertical momentum equation can be reduced to a balance between the vertical pressure gradient and gravity (this removes convective processes from the initial Navier-Stokes equations: they must be parametrized);

6. Incompressibility hypothesis: the three dimensional divergence of the velocity vector can be assumed to be zero.

For studies of ocean physics, the state of the ocean can usually be specified by the temperature, salinity and three components of velocity. In ocean models, temperature is commonly stored as potential temperature (relative to a pressure of one atmosphere) because this remains constant under adiabatic changes in pressure. Salinity - a large number of different salts dissolved in the ocean whose ratio is approximately constant - can be aggreagated in terms of a single value, called total salinity.

Because the gravitational force is so dominant in the equations of large-scale motions, it is quite useful to choose an orthogonal set of unit vectors (i, j, k) linked to the earth such that k is the local upward vector and (i, j) are two vectors orthogonal to the k system. Using this system, the 'primitive equations' are:

- The velocity (or momentum balance) equation in the horizontal:

$$\frac{\partial u_h}{\partial t} + (u_h \cdot \nabla)u_h + w\frac{\partial u_h}{\partial z} + f \times u = -\frac{1}{\rho_o}\nabla p + D_u + F_u \tag{3.1}$$

- The hydrostatic equilibrium equation or momentum balance equation in the vertical:

$$\frac{\partial p}{\partial z} = -\rho g \tag{3.2}$$

- The heat and salt conservation:

$$\frac{\partial T}{\partial t} + (u_h \cdot \nabla)T + w\frac{\partial T}{\partial z} = A_h\nabla^2 T + A_z\frac{\partial^2 T}{\partial z^2} + F_{t'} \tag{3.3}$$

$$\frac{\partial S}{\partial t} + (u_h \cdot \nabla)S + w\frac{\partial S}{\partial z} = A_h\nabla^2 S + A_z\frac{\partial^2 S}{\partial z^2} + F_{s'} \tag{3.4}$$

- The equation of state

$$\rho = \rho(T, S, p) \tag{3.5}$$

Strictly speaking the ocean in compressible but the error assuming incompressiblity is small, therefore is possible to consider:

- The incompressibility equation:

$$\nabla \cdot u + \frac{\partial w}{\partial z} = 0 \tag{3.6}$$

The prognostic variables are the horizontal velocity (u_h), the potential temperature (T) and the salinity (S). The other variables, the pressure (p), the vertical velocity (w) and the density (ρ), can be calculated from the prognostic variables from equations 3.2, 3.6 and 3.5. In these equations t is time and f is the Coriolis term (equal to $2\omega sin(\theta)$, where ω is the Earth's rotation rate and θ is the latitude. D represents diffusion and F is the forcing.

3.2.2 Coordinate system

A characteristic of rotating stratified fluids, such as the ocean, is the dominance of lateral over vertical transport. As a result, it is traditional in ocean modelling to orient the two horizontal coordinates orthogonal to the local vertical direction as determined by gravity. The choice of vertical and horizontal coordinates characterizes each particular model.

Horizontal coordinates (The model grid)

If a global model uses a latitude-longitude grid everywhere, then the convergence of the meridians means that the spacing between grid points near the north pole becomes very small. A small grid spacing requires smaller time-steps and has a large computational cost. To overcome this problem, the OCCAM model is split in two regions called 'Model 1' and 'Model 2'. Model 1 uses a standard latitude-longitude grid and covers the Pacific, Indian and South Atlantic Ocean. Model 2 covers the North Atlantic and Arctic Oceans and uses a rotated grid which has its poles on the Equator in the Indian and Pacific Oceans. The model uses an Arakawa-B grid in the horizontal, which consists basically in defining the tracers in the centre of a grid cell and the velocity at the corners (fig 3.1).

There are many issues which prompt one to choose one sort of grid over another. The preference of B grid at coarse resolution is based on its superior representation of geostrophic balance and a good representation of short wavelength inertia- gravity waves. Geostrophy is well simulated due to the location of velocity points. The main advantage of doing this is that the resulting model equations are more accurate than other schemes in representing the propagation of oceanic Rossby waves when the grid

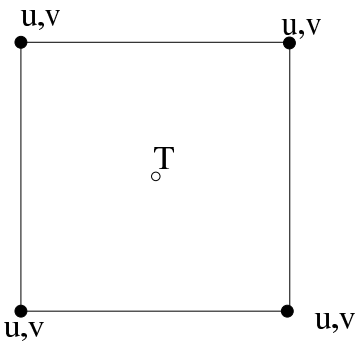

Figure 3.1: Arakawa B grid

spacing is greater than the Rossby radius of the ocean. The Rossby radius is typically 50 km for the first internal mode of the ocean and becomes much smaller for the higher modes. As a result the Arakawa-B grid is better at representing oceanic fronts and currents with small vertical extent (Griffies et al., 2000). The other widely used grid is an Arakawa -C, which is superior for well resolved waves.

The secondary advantage of the scheme is that near coastlines the velocity points lie on the boundary. This simplifies the implementation of velocity boundary conditions.

Vertical coordinate

Various ocean modelling studies (e.g. DYNAMO Group, 1997) show that the choice of vertical coordinate system is also an important aspect in an ocean model's design. The practical issues of representation and parametrization are often directly linked to the vertical coordinate choice.

There are three important regimes of the ocean to take into account for an appropriate choice of the vertical coordinate. First is the consideration of the surface mixed layer, a turbulent region dominated by transfers of momentum, heat, freshwater and tracers with the overlying atmosphere, sea ice, rivers, etc., which makes it of prime importance for climate system modelling. It is typically very well-mixed in the vertical through three-dimensional convective/turbulent processes. Such processes involve non-hydrostatic physics which requires very high horizontal and vertical resolution to explicitly represent. A parameterization of these processes is therefore necessary in primitive equation ocean models. On the other hand, tracer transport processes in the ocean interior predominantly occur along constant density directions. Therefore, water mass properties in the interior tend to be preserved over large space and time scales (e.g., basin and decade scales). Finally, the bottom ocean topography acts as a strong forcing on the overlying currents and so directly influences dynamical balances.

The OCCAM model uses the first regime discussed, called z-model regime. Which is the simplest choice of vertical coordinate and most established framework for ocean modelling. This represents the vertical distance from a resting ocean surface at $z = 0$, positive upwards and $z = -H(x, y)$ the topography. Some of the advantages of z-models are that the horizontal pressure gradient can be easily represented, as well as the equation of state for ocean water, which is highly non-linear and important for determining water mass properties. The surface mixed layer is naturally parametrized. In general, a z-coordinate provides a useful framework for representing adiabatic processes.

A disadvantage is that the representation of tracer advection and diffusion along inclined density surfaces in the ocean interior is inconvenient. The representation and parametrization of the bottom boundary layer is unnatural and the bottom topography is difficult. The OCCAM model has 36 levels in the vertical, which ranges from 20m near the surface to 255m at the depth of 5500m, where the tracers are defined in the middle of the layer.

The numerical model equations are obtained by integrating the primitive equations over the 'grid box' surroundings to give an equation in which the advective and diffusive terms are replaced by the fluxes through the boundaries of the box and the other terms written in terms of averages over the box. As discussed later, this helps to ensure that heat, salt and energy are conserved within the model.

3.2.3 Time stepping scheme

The Bryan-Cox-Semtner (Cox, 1984; Bryan, 1969; Semtner, 1974) model makes use of a mixed leapfrog - Euler forward time-stepping scheme. For solving an equation of the form:

$$\frac{\partial}{\partial t} T_i(t) = F_i(t), \tag{3.7}$$

the leapfrog time-stepping scheme is:

$$T_i(t + \delta t) = T_i(t - \delta t) + 2\delta t F_i(t), \tag{3.8}$$

where δt is the time step and T_i is the variable value of the grid box $'i'$; F_i is the value of $\frac{\partial T}{\partial t}$ at that point. The advantage of this scheme is that if the term $F_i(t)$ represents wave propagation or advection, then the amplitude of any wave remains constant. However, the scheme cannot be used when $F_i(t)$ is dissipative because the solution then becomes unstable (Arakawa, 1966). Instead, the model uses the Euler forward time-stepping

scheme for the dissipative terms. In its normal form, the Euler forward is:

$$T_i(t+\delta t) = T_i(t) + \delta t F_i(t). \tag{3.9}$$

The scheme is complementary to leapfrog in that it is stable when $F_i(t)$ represents dissipation and is unstable when used for wave propagation or advection. In the model these terms are combined as:

$$T_i(t+\delta t) = T_i(t-\delta t) + 2\delta t[F_{a,i}(t) + F_{d,i}(t-\delta t)]. \tag{3.10}$$

The model is stepped forward in time in a series of discrete time-steps. It is computationally most efficient when the time-step is as large as possible. In order to be numerically stable, the time-step must be less than the time it takes a wave, or other disturbance, to move from one grid box to the next.

The fastest wave in the ocean, the external gravity wave, has the speed of about 250 m/s. This is about one hundred times faster than the speed of the next fastest wave, the first internal mode. As the external gravity wave has little effect on the large scale circulation, it may be removed by filtering, enabling the time-step to be increased by a factor of 100 and greatly speeding up the model.

The filtering is done by separating off the barotropic and baroclinic parts of the ocean circulation and solving them using separate equations. The two parts are then recombined at the end of each baroclinic time-step.

3.2.4 Boundary conditions

The model assumes that the velocity is zero on all solid boundaries and that the gradients of potential temperature and salinity normal to solid boundaries (including the bottom) are also zero. The stress acting on the ocean due to wind and the flux of heat and fresh water through the air-sea interface drive the ocean in the upper surface boundary. Atmospheric pressure is also specified. On the bottom boundary of the ocean there is an additional friction force which depends of the current adjacent to the boundary.

3.2.5 Advection - Diffusion scheme

Any property transferred wholly by a flow is said to be 'advected' by the flow. The currents in the ocean transport energy in this way. This energy transfer is called heat

flux due to advection or advective heat flux, which can be modified on its way due to shear, upwelling, mixing, etc.

The OCCAM model is concerned with the advection of small-scale features in the tracer field by the large-scale velocity field. In the first part of the run, it uses the standard Bryan-Cox-Semtner scheme for advecting tracers and a modified scheme for the vertical advection of velocity (Webb, 1995).

The advective terms are treated in terms of the fluxes through the faces of the basic grid boxes. The volume flux through each interface is defined to be the area times the mean velocity through the interface.

The standard advection scheme is not perfect, its main problem being that it generates short wavelength noise. These consist in solving the advective part of equation 3.3 given by:

$$\frac{\partial T(x,t)}{\partial t} = -U\frac{\partial T(x,t)}{\partial x}. \tag{3.11}$$

Consider a 1-D problem where u is constant. Let x_i be the position of the ith cell, T_i the value of the tracer and δx the length, then equation 3.11 is expressed as:

$$\frac{\partial T_i}{\partial t} = -U\frac{(T_{i+\frac{1}{2}} - T_{i-\frac{1}{2}})}{\delta x} \tag{3.12}$$

Where $T_{i+\frac{1}{2}}$ is a value on the interface.

$$T_{i+\frac{1}{2}} = \frac{(T_i + T_{i+1})}{2} \, and \, T_{i-\frac{1}{2}} = \frac{(T_{i-1} + T_i)}{2} \tag{3.13}$$

the central difference form of the advection equation is given by:

$$\frac{\partial T_i}{\partial t} = -U\frac{(T_{i+1} - T_{i-1})}{2\delta x}. \tag{3.14}$$

This is the one used by Bryan-Cox-Semtner ocean model. Substituting the Taylor expansion:

$$T(x+a) = exp(a\frac{\partial}{\partial x})T(x) \tag{3.15}$$

into equation 3.14:

$$\frac{\partial T}{\partial t} = -U(\frac{\partial T}{\partial x} + \frac{\delta x^2}{3!}\frac{\partial^3 T}{\partial x^3} + \frac{\delta x^4}{5!}\frac{\partial^5 T}{\partial x^5} + ...) \tag{3.16}$$

This form of the advection equation shows a leading error proportional to δx^2. This scheme is seriously affected by dispersion, narrow maxima being reduced in amplitude

and breaking up into short wavelength noise. The problem of representing fluid advection in numerical models has proved to be difficult to solve satisfactorily, so many alternative schemes had been proposed.

QUICK scheme.

Leonards's (1979) quadratic upstream interpolation for convective kinematics (QUICK) scheme is notable in being a reasonable compromise between improved performance and computational cost. It also has the advantage that, like the ocean model, it uses a control volume to ensure that tracer is conserved.

QUICK uses quadratic upstream interpolation, instead of linear interpolation, to determine the interface temperature, which is given by:

$$T_{i+\frac{1}{2}} = \frac{1}{2}(T_{i+1} + T_i) - \frac{1}{8}(T_{i+1} - 2T_i + T_{i-1}), \tag{3.17}$$

introducing this term in the advection equation 3.14 and using Taylor series expansion to solve gives the result:

$$\frac{\partial T}{\partial t} = -U(\frac{\partial T}{\partial x} + \frac{1}{4}\frac{\delta x^2}{3!}\frac{\partial^3 T}{\partial x^3} + \frac{3}{2}\frac{\delta x^3}{4!}\frac{\partial^4 T}{\partial x^4} + ...). \tag{3.18}$$

This solution reduces the magnitude of the leading error by a factor of 4 but introduces the biharmonic diffusion term $\frac{\partial^4}{\partial x^4}$, which is a disadvantage as it means QUICK cannot be used with the leapfrog time-stepping scheme used for advection in the ocean model.

Modified Split-QUICK scheme (MSQ)

To overcome this problem, OCCAM uses the scheme in which the QUICK operator is split into two parts and the error $O(\delta x^2)$ is reduced to $O(\delta x^4)$. Webb et al. (1998) called this the modified Split-QUICK scheme (MSQ).

In this scheme $T_{i+\frac{1}{2}}$ is:

$$T_{i+\frac{1}{2}} = (\frac{T_{i+1} + T_i}{2} - \frac{T_{i+2} - T_{i+1} - T_i + T_{i-1}}{12}) + \gamma\frac{|U|}{U}(\frac{T_{i+2} - 3T_{i+1} + 3T_i - T_{i-1}}{16}), \tag{3.19}$$

and the Taylor expansion for the advection equation, 3.14, is:

$$\frac{\partial T}{\partial t} = -U[\frac{\partial T}{\partial x} - 4\frac{\delta x^4}{5!}\frac{\partial^5 T}{\partial x^5} + ...] - \gamma|U|[\frac{3}{2}\frac{\delta x^3}{4!}\frac{\partial^4 T}{\partial x^4} + \frac{15}{2}\frac{\delta x^5}{6!}\frac{\partial^6 T}{\partial x^6} + ...] \tag{3.20}$$

The first part is the standard fourth-order advection operator, which can be time-stepped using the leapfrog scheme. The second one is a velocity-dependent biharmonic diffusion operator, which can be time-stepped using the Euler forward scheme. In this way, the scheme is converted to have a purely advective and a purely diffusive part. When split in this way, the scheme can be used with the standard model time-stepping scheme. This scheme is used for tracer fields in the horizontal and vertical directions and for velocity momentum in the horizontal direction.

3.2.6 Diffusion

If a layer of warm water overlies a layer of cold water after certain amount of time both layers should reach the same temperature. This thermal equilibrium is due to the transfer of energy by the constant movement of particles in the interface. This process, given at the molecular level, is called molecular diffusion and the flux of heat is proportional to the gradient of temperature between both masses of water. The proportionality constant is the coefficient of molecular diffusivity, which is expressed as:

$$D_Q = -\rho c_p \kappa_Q \frac{\partial T}{\partial x} \tag{3.21}$$

where $\kappa_Q \sim 1.5 \times 10^{-7} \frac{m^2}{s}$ is the coefficient of molecular thermal diffusivity, ρ is the sea water density and c_p is the specific heat at constant pressure. The negative sign means that the diffusion occurs down the gradient. In the ocean, molecular diffusivity is very small.

Several processes contribute to stir the ocean, e.g. blowing of wind at the surface, perturbations due to breaking of surface waves and internal waves, or ocean currents flowing over irregular bottom in an stratified ocean. This stirring energy is called turbulence, it is described as irregular fluid flow in which some quantities of the flow show random variability in space and time. If we consider the eddies generated by the turbulence analogous to molecules, and its movement analogous to the mean free path of the molecules, we can describe the energy transported by eddies as eddy diffusion.

Eddies in the ocean transport heat due to their constant movement within the ocean. Such heat transport is proportional to the gradient of heat, the stronger the gradient, the more rapid the transfer of heat. The proportionality constant is named the eddy viscosity coefficient. Turbulent eddies in the ocean can have scales that vary from tens of centimetres to kilometres, as a consequence there is a wide range of eddy viscosity coefficients. The ocean is stably stratified, this makes easy to move water parcels

along isopycnals than across them, as a consequence the vertical turbulence is highly depressed compared with the horizontal turbulence.

Eddy viscosity coefficient values vary in the order of:

$$A_z = 10^{-4} - 10^{-3} m^2 s^{-1} \tag{3.22}$$

$$A_h = 10^{-1} - 10^{3} m^2 s^{-1} \tag{3.23}$$

where A_z denotes vertical eddy viscosity coefficient and A_h the horizontal.

The horizontal flux of heat due to turbulent diffusion can be expressed as:

$$D_h = -A_h \nabla T \tag{3.24}$$

The primitive equations describe the behavior of a geophysical fluid at space and time scales larger than a few kilometers in the horizontal, a few meters in the vertical and a few minutes. They are usually solved at larger scales, the specified grid spacing and time step of the numerical model. The effect of smaller scale motions (the turbulence coming from the advective terms of Navier-Stokes equations) must be represented entirely in terms of large scale patterns to close the equations. These effects appear in the equations as the divergence of turbulent fluxes.

The model resolution is always larger than the scale at which the major sources of vertical turbulence occurs, such as shear instability or internal wave breaking. Turbulent motions are thus never explicitly solved, even partially, but always parametrized. The vertical turbulent fluxes are assumed to depend linearly on the gradients of large-scale quantities (for example, the turbulent heat flux is given by $\overline{T'w'} = -A^{\nu T} \partial_z \bar{T}$, where $A^{\nu T}$ is an eddy coefficient). This formulation is analogous to that of molecular diffusion and dissipation. This is necessary, because considering only the molecular viscosity acting on large scale severely underestimates the role of turbulent diffusion and dissipation, while an accurate consideration of the details of turbulent motions is impractical.

Lateral turbulence can be roughly divided into a mesoscale turbulence associated with eddies, which can be solved explicitly if the resolution is sufficient, as their underlying physics is included in the primitive equations, and a sub mesoscale turbulence, which is parametrized but never partially explicitly solved. The formulation of lateral eddy fluxes depends on whether the mesoscale is below or above the gridspacing (i.e. the model is eddy-resolving or not).

The OCCAM model uses normal Laplacian diffusion and viscosity terms to represent horizontal mixing. For diffusion of tracers the value of the horizontal diffusion coefficient used in the $\frac{1}{4}^o$ version of OCCAM model is $1 \times 10^6 cm^2 s^{-1}$. For the velocity field the horizontal viscosity is $2 \times 10^6 cm^2 s^{-1}$. These values are similar to those observed in the ocean at scales of 20-30km.

As with the advection term, the diffusion term is calculated for each of the interfaces $i_{\frac{1}{2}}$ of an OCCAM cell or model grid box, estimating the gradient of temperature at the interface of two horizontal boxes (figure 3.2) according to the finite differential equation:

$$D_{i_{\frac{1}{2}},n} = -A_h \frac{T_{i+1,n} - T_{i,n}}{\Delta x} \Delta y \Delta z \tag{3.25}$$

where $A_h = 10^6 cm^2 s$ is the horizontal diffusive or mixing coefficient used in the model and $\Delta x, \Delta y \, and \, \Delta z$ are the zonal, meridional and vertical lengths of the $i_{\frac{1}{2}} - th$ cell, respectively.

As the ocean is vertically stratified, instabilities between two layers generates turbulence. This makes the vertical coefficient, A_z, change in time and space. In the vertical, OCCAM uses the Pacanowski and Philander (1981) vertical mixing for the tracer fields. The velocity fields use normal Laplacian mixing with a coefficient of $1 cm^2 s^{-1}$. The Philander and Pacanowski (PP) scheme is based in non-constant parameterization of the vertical eddy viscosity, ν, and eddy diffusivity, κ. Measurements had shown that these parameters change considerably in the oceans. They usually have large values in the mixed surface layer, but have very small values below the thermocline. Mixing processes are very important near the ocean surface. In the upper layers of the tropical oceans, the fluxes across the surface and the dynamical response to variable winds are important even on time-scales as short as a month.

The measurements of Crawford and Osborn (1979) and Osborn and Bolodean (1980) suggest that the mixing processes are strongly influenced by the shear of the ocean currents. Empirical studies (Robinson, 1966) indicate that the shear dependence of ν and κ should be of the following form:

$$\nu = \frac{\nu_o}{(1 + \alpha R_i)^n} + \nu_b, \tag{3.26}$$

$$\kappa = \frac{\nu_b}{(1 + \alpha R_i)} + \kappa_b, \tag{3.27}$$

where R_i is the Richardson number given by:

$$R_i = \frac{\beta g T_z}{U_z^2 + V_z^2} \tag{3.28}$$

$\beta \sim 8.75 \times 10^{-6}(T + 9)$ is the coefficient of thermal expansion of water, T is the potential temperature in ^oC, U and V are the horizontal velocity components, g is the gravitational acceleration, ν_b and κ_b are background dissipation parameters and ν_o, α and n are adjustable parameters. This dimensionless ratio is a measure of the potential for instability or vertical mixing in a sheared stratified fluid. A fluid with sufficiently large vertical shear will become unstable with respect to small wavelike perturbation that grow exponentially, at least for a limited time. The ocean tends to mix better along isopycnals than between isopycnals, which makes the vertical mixing coefficients smaller.

OCCAM uses the PP scheme given by:

$$A_z = \frac{\nu_0}{(1 + \alpha Ri)^n} + \nu_b, \tag{3.29}$$

where $\alpha = 5$, $n = 3$, $\nu_0 = 50$ and $\nu_b = 0.5 cm^2 s^{-1}$. The Richardson number in the model considers density effects, therefore is given by:

$$Ri = \frac{\frac{-g\partial\rho}{\rho\partial z}}{(\frac{\partial u}{\partial z})^2} \tag{3.30}$$

A necessary, but not sufficient, condition for shear flow instabilities to occur is to have a value of $Ri < \frac{1}{4}$ somewhere in the flow, if $Ri > \frac{1}{4}$ everywhere in the flow the system is stable.

The finite difference equation that represents the Richardson number in OCCAM is given by:

$$Ri_k = g\frac{(z_{k+1} - z_k)}{\rho}\frac{(\rho_k - \rho_{k+1})}{((u_k - u_{k+1})^2 + (v_k - v_{k+1})^2)} \tag{3.31}$$

3.2.7 Box Conservation of Fluxes

The model ensures flux conservation by first partitioning the ocean into cells whose interfaces lie along lines of constant latitude, longitude and depth. Representing one

cell (or model grid box) with i, then, integrating over the cell,

$$V_i \frac{\partial T_i}{\partial t} - \sum_j A_{ij} u_{ij} T_{ij} = \sum_j A_{ij} D_{ij} \tag{3.32}$$

where, V_i is the volume of the cell and T_i the mean value of the tracer T. $A_{ij}u_{ij}T_{ij}$ represents the advective flux of the tracer from cell j to cell i, the sum being over the six cells adjacent to i, A_{ij} is the area across the interface, u_{ij} is the mean velocity of water into cell i through the interface and T_{ij} the mean value of the tracer at the interface. D_{ij} is the diffusive flux per unit area across the interface.

The total amount of tracer in the model will remain constant if the fluxes balance, that is:

$$\sum_i \sum_j A_{ij} u_{ij} T_{ij} + \sum_i \sum_j A_{ij} D_{ij} = 0. \tag{3.33}$$

This is satisfied as long as the flux across each interface is the same for the cells on each side. Thus, advective flux is conserved if:

$$u_{ij} = -u_{ji} \quad and \quad T_{ij} = T_{ji}. \tag{3.34}$$

An important step in the development of any finite difference model is the choise of u_{ij} and T_{ij}, so that 3.33 represents the equations of heat and salt conservation (equations 3.3 and 3.4) as accurately as possible. In the standard model this is done by interpolating the boundary values from the nearest grid points. Thus, for the tracer field, the model uses the high order Split-QUICK scheme.

3.2.8 The free surface

The model replaces the rigid lid of the standard Bryan-Cox-Semtner scheme with a free surface. The resulting barotropic equations are solved using a simple tidal model with a time-step of 18s.

Aliasing problems can arise with fast baroclinic waves which have a period of approximately one barotropic time-step because they can interact strongly (and unphysically) with slow baroclinic waves of the same wavelength. This instability is prevented by stepping the tidal model on for two baroclinic time-steps and by taking the average values over this period to give the free surface height and barotropic velocities at the new central baroclinic time-step.

The inclusion of a free surface means that the thickness of the surface layer of the

model is no longer fixed. Rainfall and evaporation now produce changes in sea level. They also produce changes in the thickness of the surface layer of grid boxes and, because salt is conserved, result in changes in surface salinity.

3.2.9 Model initialization and forcing fields.

For the first main run of the OCCAM model, the initial potential temperature and salinity fields were initialized from the Levitus (1982) global annual average database. The temperature was first converted to potential temperature. The potential temperature and salinity were then interpolated from the one degree Levitus grid and Levitus levels to the model grid and levels using linear interpolation. The velocity fields were initialized to zero. At coastlines the boundary condition is that both horizontal components of the velocity are zero.

The initial spin-up phase of the model run lasted for 1440 days (4 years). During this time a robust diagnostic scheme relaxed the model potential temperature and salinity fields everywhere toward the Levitus values. This ensured that the model did not drift far from Levitus during the period. Following the initial spin-up phase the model was allowed to run for another four years before analysis began. This allowed some of the initial transients to die away and allowed the eddy field to develop. Unfortunately the phase velocity for the higher Rossby waves modes is so slow that a steady state eddy field is unlikely to have been achieved.

The wind stress used to force the first main run of the OCCAM model was the monthly averaged ECMWF wind stress climatology, calculated by Siefridt and Barnier (1993) from the years 1986 to 1988 inclusive. The data was corrected so that when linearly interpolated in time the correct average stress was applied each model month (Killworth et al., 1991).

The surface fluxes of heat and fresh water were calculated so as to relax the surface layer of the model to the Levitus monthly average values (Levitus and Boyer, 1994; Levitus, 1982; Levitus et al., 1994).

3.2.10 Grid box

Figure 3.2 shows a model grid box at the point ijk, where i represents longitude, j latitude and k depth. The length of each side of the box are given by dx, dy and dz. The interfaces of the box are represented by $i + \frac{1}{2}$, $i - \frac{1}{2}$, etc (see figure).

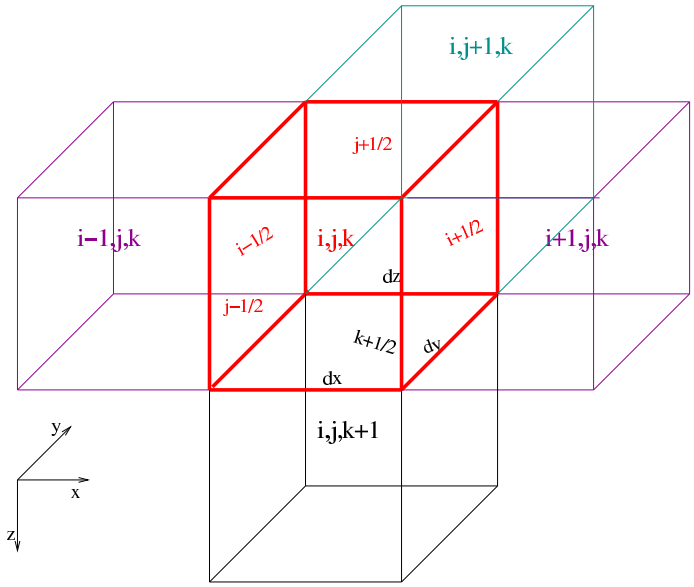

Figure 3.2: Model box ijk. i represents the longitude, j the latitude and k the model depths. Values with $\frac{1}{2}$ represents the interfaces of the box.

3.2.11 Analysis time-step

The model calculates the state of the ocean every model time-step, $n = 15\,minutes$, but data is only archived every five days. The black curve in figure 3.3 represents a tracer at each model time-step. A copy of this is archived at midnight at the end of every five days. This is called the instantaneous output of the model.

The instantaneous output can contain the effects of large amplitude inertial oscillations. To remove this, an average over each five days is also calculated and archived at the same time. Then, for a tracer T, the five day mean dataset is given by equation:

$$T_{t_{i+\frac{1}{2}}} = \frac{1}{\Delta t_i} \int_{t_i}^{t_{i+1}} T_n dn \tag{3.35}$$

where t_i and t_{i+1} are two adjacent archive timesteps. This represents a value at the middle of the time interval, i.e. at time-step $t_{i+\frac{1}{2}}$ and is the 5 day-mean dataset (blue curve in figure 3.3).

In this study the best estimate of heat flux due to advection and diffusion is done using the 5 day-mean data. As the 5 day-mean velocity field has less fluctuations than the instantaneous output. This means that the heat fluxes are estimated at time $t_{i+1/2}$. For simplicity I will refer to $t_{i+\frac{1}{2}}$ as $t_{i\frac{1}{2}}$.

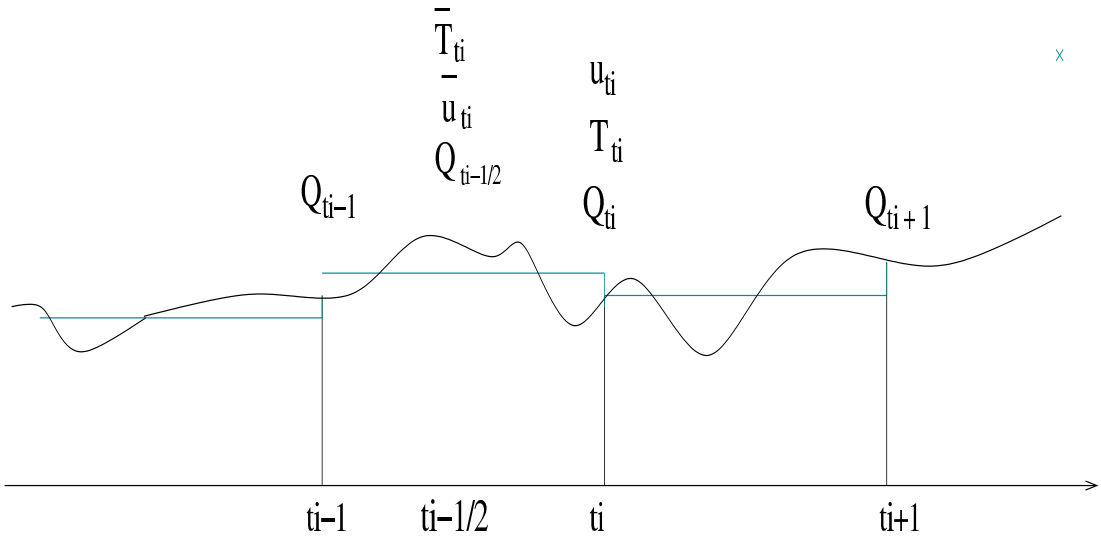

Figure 3.3: Analysis time-step $t_i = 5\,days$. Quantities with bar represent values of the 5-day mean dataset, and without bar are instantaneous output.

3.3 Method

3.3.1 Heat flux

From the atomic point of view a macroscopic sample of matter is an agglomerate of an enormous number of electrons and nuclei. These particles tend to move or vibrate in organized patterns called normal modes. The amplitude of these normal modes are called normal coordinates. When these coordinates are averaged statistically some of them are lost and a few, with unique symmetric properties, survive the statistical average associated with a transition to a macroscopic description. Some of the surviving coordinates are mechanical in nature, as volume, parameters descriptive of shape, components of elastic strain, etc. Other are electrical e.g., electric and magnetic dipole moments. The atomic coordinates, which, by virtue of the statistical average, do not appear explicitly in a macroscopic description of a system are the matter of study of thermodynamics. It is possible to transfer energy to the non-macroscopical atomic modes of motion, such transfer of energy is called heat.

In defining heat as a transfer of energy that takes place at the molecular level, but macroscopically observable, it is important to point out that only the differences of energy rather than absolute values of the energy have physical significance. So, it is conventional to adopt some particular state of a system as a fiducial state where the energy is arbitrarily taken as zero. The energy of any other state relative to this state is called the thermodynamic internal energy of the system in that state, denoted by U.

The heat or heat flux given to a system in any process is the difference of internal

energy between the final and initial state minus the work done in the process, expressed as:

$$dQ = dU - dW \tag{3.36}$$

where dQ is the transfer of heat in the process, dW is the quasi-static work associated with the change in volume of a thermodynamic simple system, given by:

$$dW = -PdV \tag{3.37}$$

When there is no work done in the system $dW = 0$, and the change of internal energy equals the change of heat flux, I.e..

$$dQ = dU \tag{3.38}$$

Temperature is a measure of the kinetic energy of the particles in a sample, if the kinetic energy is increased, the temperature would rise. The ratio of the heat flux per mole required to increase the temperature one unit is the specific heat. This process can be achieved either at constant volume or constant pressure. The specific heat per unit volume at constant pressure is expressed as:

$$c_p = (\frac{dQ}{dT})_p \tag{3.39}$$

3.3.2 Heat in the ocean

In the earth system the main source of heat is the radiative energy received by the sun. This solar energy is also the main source of heat for the ocean. An internal source of heat is the decay of radioactive matter within the earth's interior, which maintains the material below the surface crust in either a plastic or a fluid condition (except for the inner, solid core). This source of heat just influences the temperature at the bottom of the deep sea and does not play a major role in the dynamical effects.

In a time scale of a year, the ocean is not heating up or cooling down much so there is an annual balance of heat. There is a significant amount of heat exchanged across the ocean surface due to: short-wave radiation received from the sun; radiative heat in the infrared spectrum exchanged between the atmosphere and the ocean; loss of heat due to evaporation; and heat exchange due to conduction in the atmosphere-ocean interface when a difference of temperature exists.

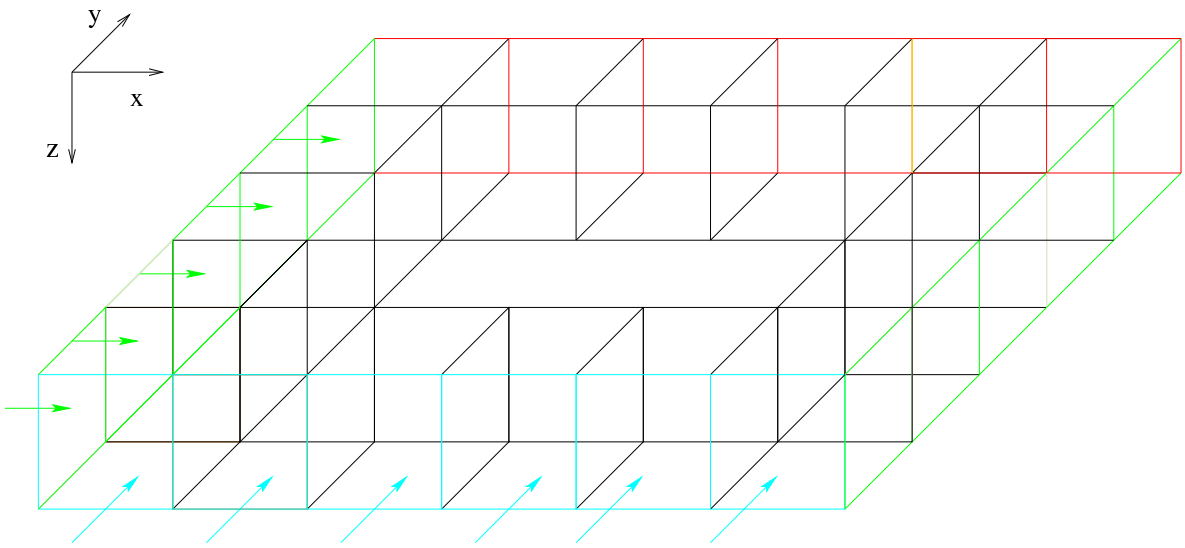

Figure 3.4: Subvolume composed of several model grid boxes.

In the interior of the ocean the heat is transported by the currents systems, horizontal diffusion and vertical mixing processes. This thesis tries to understand the physical processes that determine the heat balance in the equatorial Pacific Ocean.

3.3.3 Equations

The main objective of this thesis is the study of the physical processes affecting the heat balance in OCCAM, within the Tropical Pacific ocean. To achieve this, I subdivided the Tropical Pacific into key regions or boxes (explained in chapter 4). I made use of the $\frac{1}{4}$ of degree OCCAM run for the year 1993, which was forced with 6-hourly winds from the ECMWF.

The approach I adopted is to implement equation 3.32 for each region under consideration. This equation calculates, for each model grid box each model timestep, the heat flux due to advection and diffusion across each interface. In this analysis, the regions under study are composed by several model grid boxes (figure 3.4). Then, the heat flux due to advection, F, across the interface $i_{\frac{1}{2}}$ of each model box is calculated using the 5-day mean fields of velocity and temperature, each analysis time step (t_i = 5 days) given by:

$$F_{i_{\frac{1}{2}},t_i} = \rho A_{i_{\frac{1}{2}}} C_p u_{i_{\frac{1}{2}},t_i} \left[\frac{(T_{i+1,t_i} + T_{i,t_i})}{2} - \frac{(T_{i+2,t_i} - T_{i+1,t_i} - T_{i,t_i} + T_{i-1,t_i})}{12} \right] \tag{3.40}$$

where the first term is the central difference (C-D) term and the second term in brackets is the extra advective component of the Split-QUICK scheme discussed in section 3.2.5.

The temperature is given at the interface $i_{\frac{1}{2}}$, i.e. $T_{i_{\frac{1}{2}}}$.

The heat flux due to advection, for a complete interface, l, during the year under study, is obtained integrating the above equation in time and summing the fluxes of each individual interface components as:

$$F_{l,\tau} = \sum_i \frac{1}{\tau} \int_0^\tau F_{i_{\frac{1}{2}},t_i} dt_i \tag{3.41}$$

where $\tau = 1\, year$. The heat gain by advection in the full box, is obtained by adding the six interfaces:

$$\bar{F}_{tot,\tau} = \sum_l F_{l,\tau} \tag{3.42}$$

The heat gain by diffusion is obtained in a similar way. For each interface $i_{\frac{1}{2}}$ it is given by:

$$D_{i_{\frac{1}{2}},t_i} = A_{h(z)} \Delta y \Delta z \left[\left(\frac{T_{i+1,t_i} - T_{i,t_i}}{\Delta x} \right) + \gamma \left(\frac{|u|}{u} \left(\frac{T_{i+2,t_i} - 3T_{i+1,t_i} + 3T_{i,t_i} - T_{i-1,t_i}}{16} \right) \right) \right] \tag{3.43}$$

where the subindice h in A_h represents the horizontal diffusion coefficient and z the vertical one. The last term is the diffusive component of the Split-QUICK scheme. Then, the diffusive heat flux, at each interface of the regions under study, is given by:

$$\bar{D}_{l,\tau} = \sum_i \frac{1}{\tau} \int_0^\tau D_{i_{\frac{1}{2}},t_i} dt_i \tag{3.44}$$

and the heat gain by diffusion is:

$$\bar{D}_{tot,\tau} = \sum_l D_{l,\tau} \tag{3.45}$$

3.3.4 Rate of change of heat content

The density of a parcel of seawater is determined by the pressure to which it is subjected, its temperature and salinity. If compression effects are ignored, seventy five percent of the ocean density ranges between $1026.4\, and\, 1028.1 kgm^{-3}$. For some purposes one can ignore this small variation in density and assume an homogeneous ocean. For the heat content in the runs studied, the model uses the constant values of $\rho = 1 g/cm^3$ and $C_p = 1 cal/gC$.

The heat content of a parcel of water, of mass m, in the ocean is a function of its temperature, density and specific heat. This is shown expressing the change of heat

content, dQ, (equation 3.39) as:

$$dQ = mC_p dT \tag{3.46}$$

The first term of the left hand side of equation 3.32 represents the rate of change of heat content. Using the time stepping scheme:

$$\frac{\partial Q_n}{\partial t} = \frac{Q_{n+1} - Q_{n-1}}{2\delta t} \tag{3.47}$$

the model tries to satisfy the finite differential equation for the rate of change of heat content, for each model grid box ijk at each model time-step, $n = 15\,minutes$, according with equation 3.10 as:

$$\frac{\partial Q_{ijk,n}}{\partial t} = F_{ijk,n} + D_{ijk,n-1} \tag{3.48}$$

In this analysis, I looked at each of the terms separately. The rate of change of heat content is calculated using the temperature output of the instantaneous values, as:

$$\frac{\Delta Q_{t_i}}{\Delta t_i} = C_p \rho dx dy dz (\frac{T_{t_{i+1}} - T_{t_i}}{\Delta t_i}) \tag{3.49}$$

The integral in time and space of the above equation gives the rate of heat content for the year.

$$\int_0^\tau \frac{\partial Q}{\partial t} dt = C_p \rho \int dV \int \frac{\partial T}{\partial t} dt \tag{3.50}$$

This analysis tries to satisfy equation:

$$\frac{\Delta Q_\tau}{\Delta \tau} = \bar{F}_{tot,\tau} + \bar{D}_{tot,\tau} \tag{3.51}$$

3.4 Mean field and fluctuations in time

I further split the heat flux due to advection in its mean and fluctuating components. It is possible to separate the velocity and temperature fields, for every analysis time-step, into their mean and fluctuating parts for each interface of the box as:

$$u_{i_{\frac{1}{2}}} = \bar{u}^t_{i_{\frac{1}{2}}} + u'_{i_{\frac{1}{2}}} \tag{3.52}$$

$$T_{i_{\frac{1}{2}}} = \bar{T}^t_{i_{\frac{1}{2}}} + T'_{i_{\frac{1}{2}}} \tag{3.53}$$

where $\bar{u}^t = \frac{1}{\tau}\int_0^\tau u dt$ is the mean velocity for the analysis period τ and $u'_{i_{\frac{1}{2}}}$ represents fluctuations from the mean due to processes with time scales less than τ. $T_{i_{\frac{1}{2}}}$ is the temperature as represented in equation 3.40, $\bar{T}^t = \frac{1}{\tau}\int_0^\tau T dt$ is the mean temperature for the period τ and $T'_{i_{\frac{1}{2}}}$ are the fluctuations around the mean. Substituting equations 3.52 and 3.53 into equation 3.40, for the velocity and temperature fields respectively; ignoring ρ, C_p and $A_{i_{\frac{1}{2}}}$, the total advection heat flux through the interface can be written as:

$$u_{i_{\frac{1}{2}}} T_{i_{\frac{1}{2}}} = (\bar{u}^t_{i_{\frac{1}{2}}} + u'_{i_{\frac{1}{2}}})(\bar{T}^t_{i_{\frac{1}{2}}} + T'_{i_{\frac{1}{2}}}). \tag{3.54}$$

It is important to notice that $T_{i_{\frac{1}{2}}}$ does represent the temperature using the split-QUICK scheme. But for simplicity, in the rest of this chapter, I will refer to it just as $T_{i_{\frac{1}{2}}}$.

Integrating the above equation for the period of time τ we get:

$$\int_0^\tau u_{i_{\frac{1}{2}}} T_{i_{\frac{1}{2}}} dt = \int_0^\tau \bar{u}^t_{i_{\frac{1}{2}}} \bar{T}^t_{i_{\frac{1}{2}}} dt + \int_0^\tau \bar{u}^t_{i_{\frac{1}{2}}} T'_{i_{\frac{1}{2}}} dt + \int_0^\tau u'_{i_{\frac{1}{2}}} \bar{T}^t_{i_{\frac{1}{2}}} dt + \int_0^\tau u'_{i_{\frac{1}{2}}} T'_{i_{\frac{1}{2}}} dt \tag{3.55}$$

where $\bar{T}^t_{i_{\frac{1}{2}}} \int_0^\tau u'_{i_{\frac{1}{2}}} dt = 0$ and $\bar{u}^t_{i_{\frac{1}{2}}} \int_0^\tau T'_{i_{\frac{1}{2}}} dt = 0$, then the equation for the full heat flux, for one interface of a grid box of area $A_{i_{\frac{1}{2}}}$ is:

$$\int_0^\tau u_{i_{\frac{1}{2}}} T_{i_{\frac{1}{2}}} A_{i_{\frac{1}{2}}} dt = \int_0^\tau \bar{u}^t_{i_{\frac{1}{2}}} \bar{T}^t_{i_{\frac{1}{2}}} A_{i_{\frac{1}{2}}} dt + \int_0^\tau u'_{i_{\frac{1}{2}}} T'_{i_{\frac{1}{2}}} A_{i_{\frac{1}{2}}} dt \tag{3.56}$$

The integral of the above equation is:

$$\overline{u_{i_{\frac{1}{2}}} T_{i_{\frac{1}{2}}}}^t A_{i_{\frac{1}{2}}} = (\bar{u}^t_{i_{\frac{1}{2}}} \bar{T}^t_{i_{\frac{1}{2}}})^t A_{i_{\frac{1}{2}}} + \overline{(u'_{i_{\frac{1}{2}}} T'_{i_{\frac{1}{2}}})}^t A_{i_{\frac{1}{2}}} \tag{3.57}$$

This equation states that the total heat flux due to advection is the sum of the heat flux carried by the mean flow and the heat flux carried by fluctuations during the period of time τ, i.e.:

$$\bar{F}^\tau_{i_{\frac{1}{2}}} = \overline{\bar{F}_{i_{\frac{1}{2}}}}^\tau + \bar{F}^{\tau'}_{i_{\frac{1}{2}}} \tag{3.58}$$

when τ equals five days (analysis period) the first term of right hand side is the archived 5 day-mean output and the second term, the fluctuation term, needs to be estimated.

I used the 5-day mean horizontal velocity fields, meanwhile the vertical velocity

depends on the vertical advective flux of volume (or mass). In the OCCAM model this is a derived quantity calculated by first setting the vertical volume flux to zero at the bottom of the ocean. Using the conservation of volume equation, together with the horizontal volume fluxes at each level, it integrates the vertical volume flux to higher levels of the ocean.

The above equations are implemented in a FORTRAN code for the different regions in the Pacific Ocean under study.

Chapter 4

Mean Volume Transport in the 1/4 of degree OCCAM Run

4.1 Introduction

At the equator strong easterly trade winds drive a westward surface flow producing a pressure gradient as water piles up at the western boundary. A few degrees north and south, the surface Ekman flow is poleward while the eastward pressure gradient induces equatorward geostrophic flow below this and within the thermocline. Equatorial upwelling occurs near the equator and downwelling is located in convergence zones about 3 to 4 degrees from the equator.

A system of surface and subsurface zonal equatorial currents, linked by a meridional circulation driven by Ekman, geostrophic and nonlinear dynamics, has been recognized since the earlier modern observations (e.g., Knauss, 1960, 1966) and has been recently named Tropical Cells (TCs) (Lu et al., 1998; Johnson and McPhaden, 2001).

Fofonoff and Montgomery (1955) explain that, as a parcel moves equatorward associated with the lower branch of the TCs within the thermocline, its loss of planetary vorticity is compensated by a gain of relative vorticity resulting in the eastward Equatorial Undercurrent (EUC). This current is not dynamically isolated, but rather an essential part of the Pacific general ocean circulation. Indeed, it is the equatorial branch of several meridional circulation cells that extend to mid and higher latitudes. Observations are not sufficient to allow a complete description of the Tropical Cells, primarily because it is extremely difficult to measure vertical velocity. Modelling studies have therefore been valuable in providing a comprehensive picture of the flow (Lu et al., 1998). The weaker meridional circulation and upwelling within a few degrees of

the equator are not only important elements of the general circulation, but they also have a strong control on global climate and bio-geochemical cycles (Philander, 1990).

Using CTD and ADCP datasets Lu et al. (1998) and Johnson and McPhaden (2001) made meridionally localized estimates of the zonal flow and large-scale estimates of the meridional flow and horizontal divergence in the upper tropical Pacific Ocean. Sloyan et al. (2003) estimated a tropical Pacific circulation using inverse methods to combine a new mean temperature, salinity and direct velocity climatology with air-sea flux climatologies and historical CTD and XBT data in the eastern Pacific. The equatorial upwelling has been estimated in a number of ways over a number of spatial and temporal scales. In addition, several studies have observed the subsurface countercurrents (SSCCs) in both the Atlantic and Pacific Oceans. The persistent eastward subsurface currents are found on either side of the equator and are associated with sub-thermocline isotherms plunging toward the equator at the poleward flank of the 13C thermostad, a thick layer of nearly homogeneous water near the equatorial region (Wang, 2005).

In this chapter I explore the spatial patterns and dynamics of these processes within the Tropical Pacific in OCCAM, addressing the questions of how does the water recirculate within the Tropical Pacific in the 1/4 of degree run, and how much of it leaves the Tropics toward the poles.

4.2 Regions under study

As discussed in chapter 2, the western equatorial Pacific Ocean is characterized by high sea surface temperatures, a deep thermocline and low velocities. Above, strong convection drives different atmospheric cycles. The ocean's low velocities and high temperatures make it a heat reservoir. Perturbations in this region, like westerly wind bursts, can have a great impact on global weather. The region is strongly linked to the beginning of an El Nino event. An understanding of the physical processes affecting the heat balance in it is key in improving our knowledge about ENSO and climate variability.

The eastern equatorial Pacific is mainly characterized by the cold tongue, where the temperature can fall to 24C, and there is strong upwelling. The current system described in section 2.4 is well developed in this region of the Pacific, which during autumn can host strong eddy motion, such as the TIWs.

The different characteristics of the east and west mean that it is necessary to study the processes within these regions separately. For this reason I found it convenient to

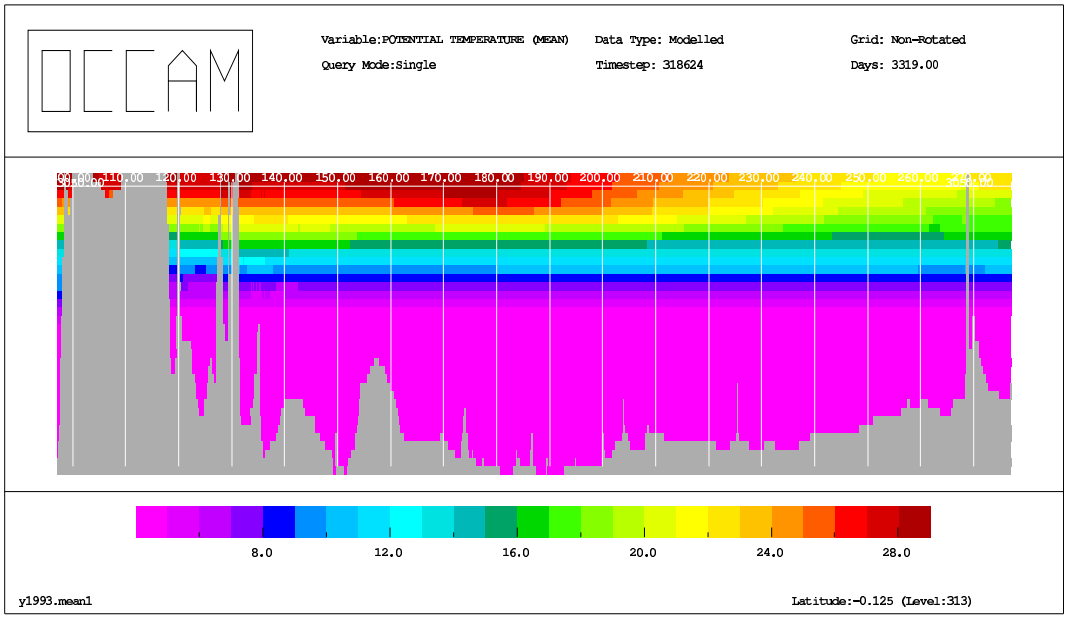

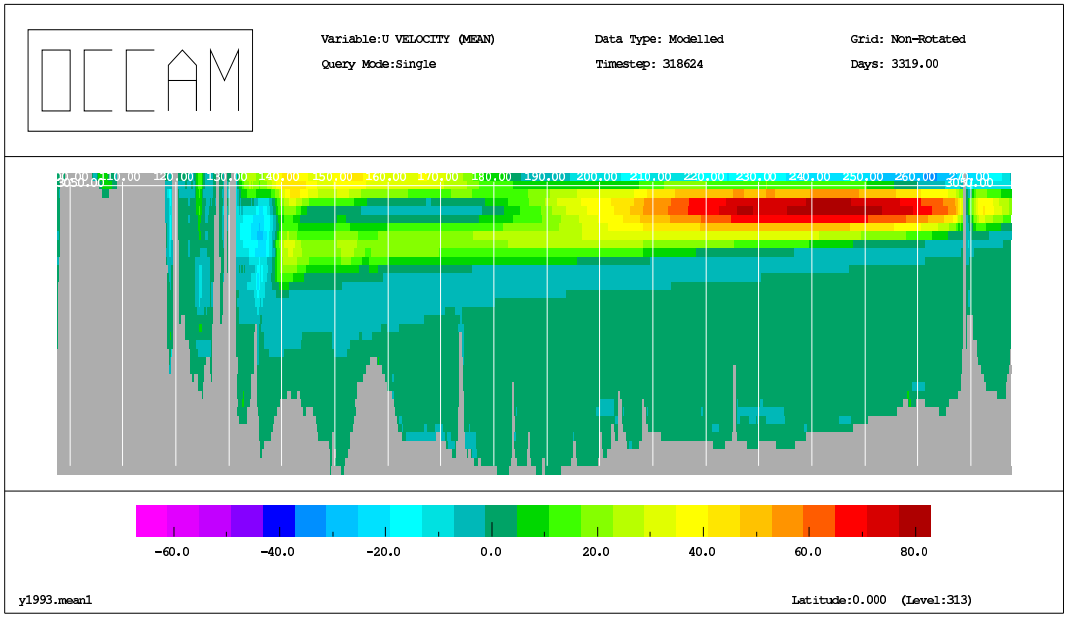

Figure 4.1: Cross section across the equator of the mean temperature (in C, top) and the mean zonal velocity (in cms^{-1}, bottom) for the year under study according with OCCAM.

define the Tropical Pacific region longitudinally from 150E to 120W and latitudinally from 12S to 10N, and split it into three zonal regions. The first region is in the west, which extends from 150E to 180E, where the Warm Pool is fully embedded in OCCAM. A second region, off the American continent, which includes a large part of the cold tongue and the TIWs (lower panel of figure 4.2), extends from 150W to 120W. Between these regions, I define the Central Pacific region, a transition zone, extending from 180E to 150W. This part of the ocean is characterized by the end of the MJO. Zonally the regions have the same extent in order to make the meridional transport comparable.

As seen in section 2.4, the currents are not symmetrical about the equator; instead, their latitudinal and vertical extent varies considerably. While the NECC extends from 3N to 10N, the SEC extends from 3N to around 8S. In the vertical, the EUC extends down to around 250m and the NEC just extends down to approximately 150m.

Another remarkable feature of this current system is its intensity, which varies in longitude, latitude and also in depth. For example, the EUC can reach speeds of about 90cm/s in its core in the East Region (figure 2.5), meanwhile in the West Region, where it is deeper, it never exceeds $30 cms^{-1}$ (figure 4.1).

Meridionally, I found it convenient to further subdivide the above regions according to the latitudinal extent of the main current system in the equatorial Pacific in OCCAM. Figure 4.3 shows the integral of the zonal velocity for the East, Central and West regions, as a function of latitude, for four levels of the model. It shows the mean current system in OCCAM for the year under study for the three zonal regions.

The eastward current that extends from 5N to 10N in the figure corresponds to the mean location of the North Equatorial Countercurrent (NECC). It persists throughout the three zonal regions and decreases its intensity below model level seven (163.67m). This region will be referred to as the NECC Region.

The South Equatorial Current (SEC) extends from 3N to 7S in the first few metres of the ocean (around 30m). At the equator, below the direct influence of the wind, the Equatorial Undercurrent (EUC) is confined to just two degrees north and south of the equator. The SEC is found north and south of the EUC. As shown in figure 4.3 the EUC in the model extends from 1S to 2N approximately from level three to ten (52.35m to 295.34m). In the uppermost level the SEC extends from 5N to 7S, and below it, its northern branch extends from 2N to 5N and the southern one from 1S to 7S. This gives three further subdivisions in the meridional direction. These subdivisions are the NSEC Region, which stands for the northern branch of the SEC, from 2N to 5N, the Equatorial or EUC Region from 1S to 2N and the SEC region from 1S to 7S. To the

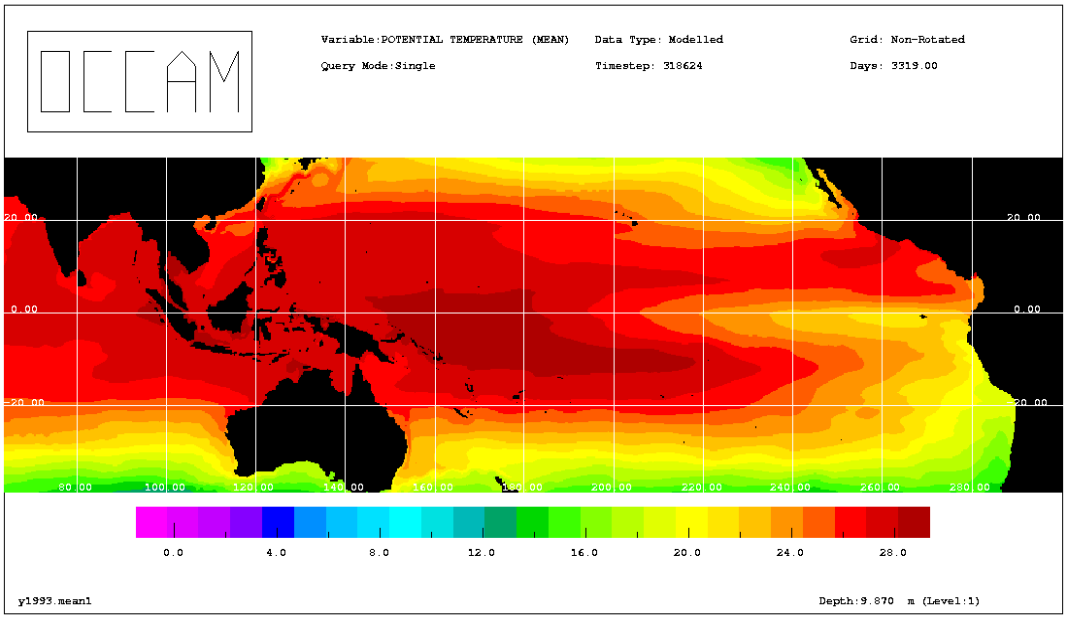

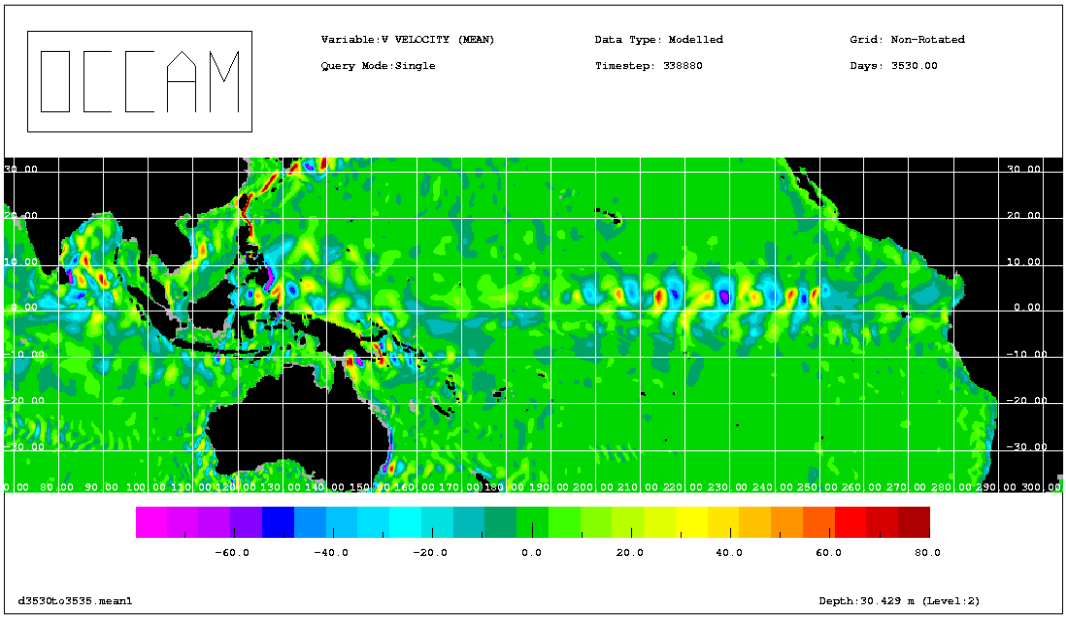

Figure 4.2: Mean sea surface temperature for the year under study (in C, upper panel) and meridional velocity at level two (30.43m) for the first week of September 1993 (in cms^{-1}, bottom panel), according with OCCAM output.

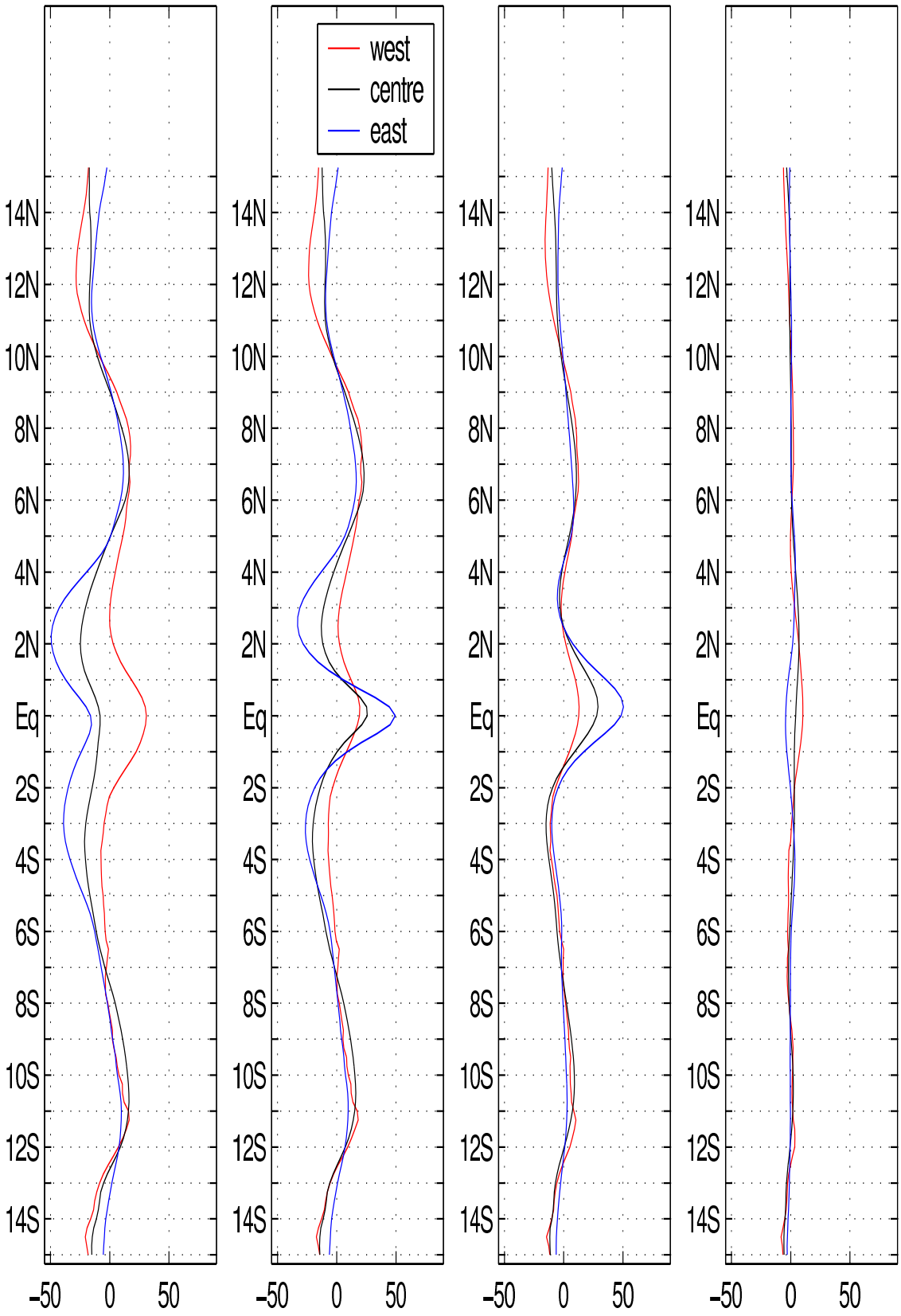

Figure 4.3: Average of zonal velocity for East Region (blue), Central Region (black) and West Region (red) as a function of latitude from 15S to 15N, using the output of the 1/4 of degree OCCAM run. Levels 1, 4, 5 and 11 (9.87m, 76.05m 102.04m and 355.07m) from left to right. Units cms^{-1}.

south the eastward South Equatorial Countercurrent, SECC, is found, which extends from 7S to 12S and is the fifth meridional region called the SECC Region.

In the vertical, the equatorial Pacific Ocean is characterized by a strong thermocline, which separates the warm surface waters from the colder waters at depths. The thermocline shallows from west to east. In the west it is located at the bottom of the warm pool, meanwhile it surfaces to the east. On the other hand, the direct response of the ocean to the wind stress, the Ekman transport (see section 4.4), is principally confined to the upper mixed layer, between 10 and 100m deep.

The regions are subdivided vertically into an upper mixed layer, or mixed layer box, which extends from the surface down to 41.20m, (the bottom of model level 2). Below it, I define a subsurface box, down to the bottom of the Warm Pool, which in OCCAM corresponds to 146.79m (bottom of level 6). Finally, a Bottom box is defined from 146.79m down to 388.83m (level 11), which corresponds to the level where the EUC in the west decreases. With these choices, the EUC is confined in the Bottom box in the West and into the Subsurface box in the Centre and East. The horizontal surface currents are located in the mixed layer box, including the influence of the Ekman transport.

As stated in section 3.2.7, the model ensures flux conservation. Following the integral in space and time discussed in section 3.4, the volume transport, T_l, through each side of each of the boxes described above is calculated as:

$$T_l = \frac{1}{\tau} \int_1^{\tau} \sum_{i=1}^{n} A_i u_i dt \tag{4.1}$$

where A_i is the area of each individual model cell, u_i is the velocity perpendicular to the cell, n is the number of cells in each side of the box and τ is the time period under study.

In the mixed layer the meridional transport is composed of the Ekman transport contribution (discussed in section 4.4) and a remaining, predominantly geostrophic contribution, which is calculated as a residual.

4.3 Volume flux in the Tropical Pacific

4.3.1 Tropical Pacific region

Figure 4.4 shows the total transport in the Tropical Pacific Region averaged over the year under study. The top panel of the figure represents the mixed layer box, the middle panel the subsurface box and the last panel the Bottom Box. The arrows indicate inflow or outflow through the corresponding side of the box (north, south, east or west). The vertical flow corresponds to the flow through the bottom of each box. This means that the vertical flow shown in the mixed layer box is also the vertical flow at the top of the subsurface box. The vertical flow is represented by a cross when it is downward and a dot when the flow is upward.

From the figure it can be seen that, within OCCAM, the surface layer transports more volume northward, 21.68Sv, than southward, 8.39Sv. The main balance to this divergence is zonal convergence, with a stronger contribution from the westward flow across 120W. The rest of the volume flow is balanced by upwelling and an eastward component flow across 150E. A small fraction of the volume is balanced by evaporation and precipitation processes.

The Subsurface box and the Bottom box show strong eastward transport, which weakens mainly due to upwelling. Meridionally both boxes exhibit northward transport, with a stronger component in the north.

4.3.2 East, Central and West Tropical Pacific

Figure 4.5 shows the volume flow in the Eastern, Central and Western Tropical Pacific regions. The West Region, where the Warm Pool is embedded, shows inflow at 150E in the three vertical boxes. This eastward flow weakens in the mixed layer due to meridional divergence and in the subsurface box due to vertical divergence. The eastward flow remains almost constant throughout the whole basin in the Subsurface and Bottom boxes. In the Mixed layer there is a westward flow from the East region, which weakens due to meridional divergence as well.

Thus, at large scales, the volume flow in OCCAM is found to be strongest toward the north out of the tropics, where the transport decreases from west to east. Southward, the West and East regions transport more volume out of the tropics than the Centre. In the mixed layer a strong westward component is observed, which weakens considerably

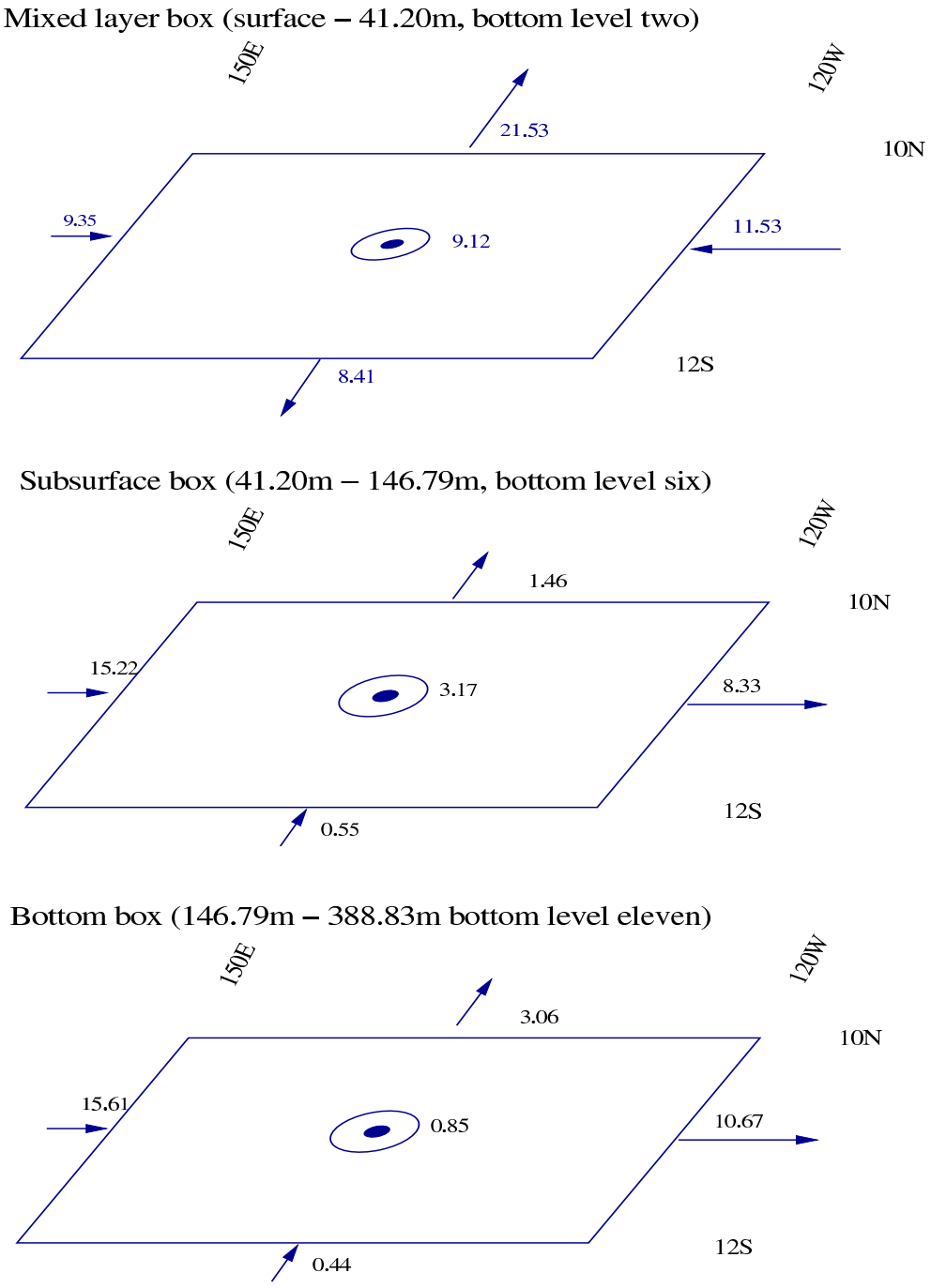

Figure 4.4: Volume transport (in Sv) for the Tropical Pacific Region defined between the longitudes 150E to 120W and the latitudes 10N to 12S, at the mixed layer, subsurface and bottom layers. The arrows represent volume flow out or in of the corresponding wall of the box. The dot or cross in the middle of each box represents upwelling or downwelling, respectively, at the bottom of the box.

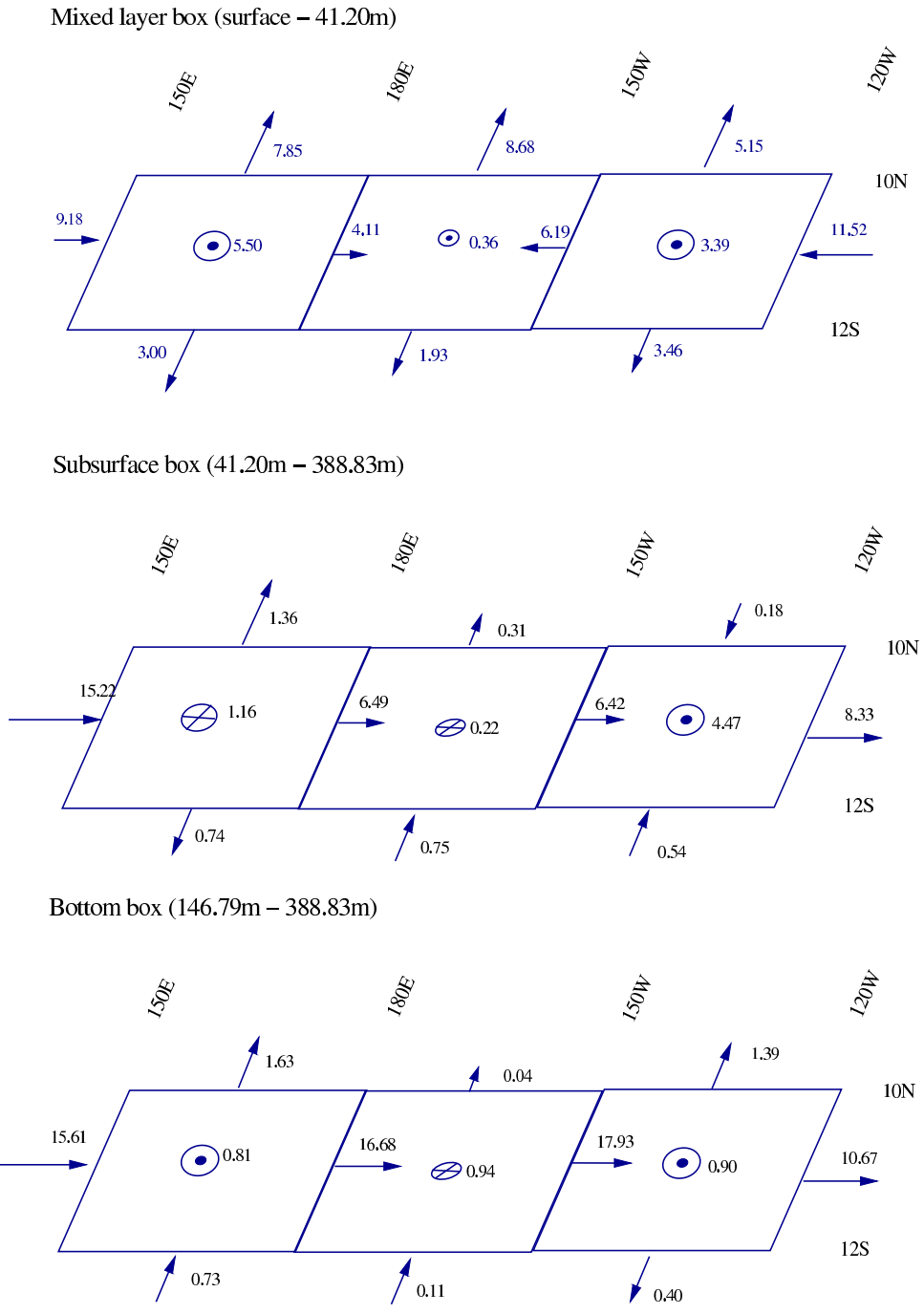

Figure 4.5: Volume transport (in Sv) for the East, Central and West Tropical Pacific Region, for the mixed layer, subsurface and bottom layers. The arrows represent volume flow out or in of the corresponding wall of the box. The dot or cross in the middle of each box represents upwelling or downwelling, respectively, at the bottom of the box.

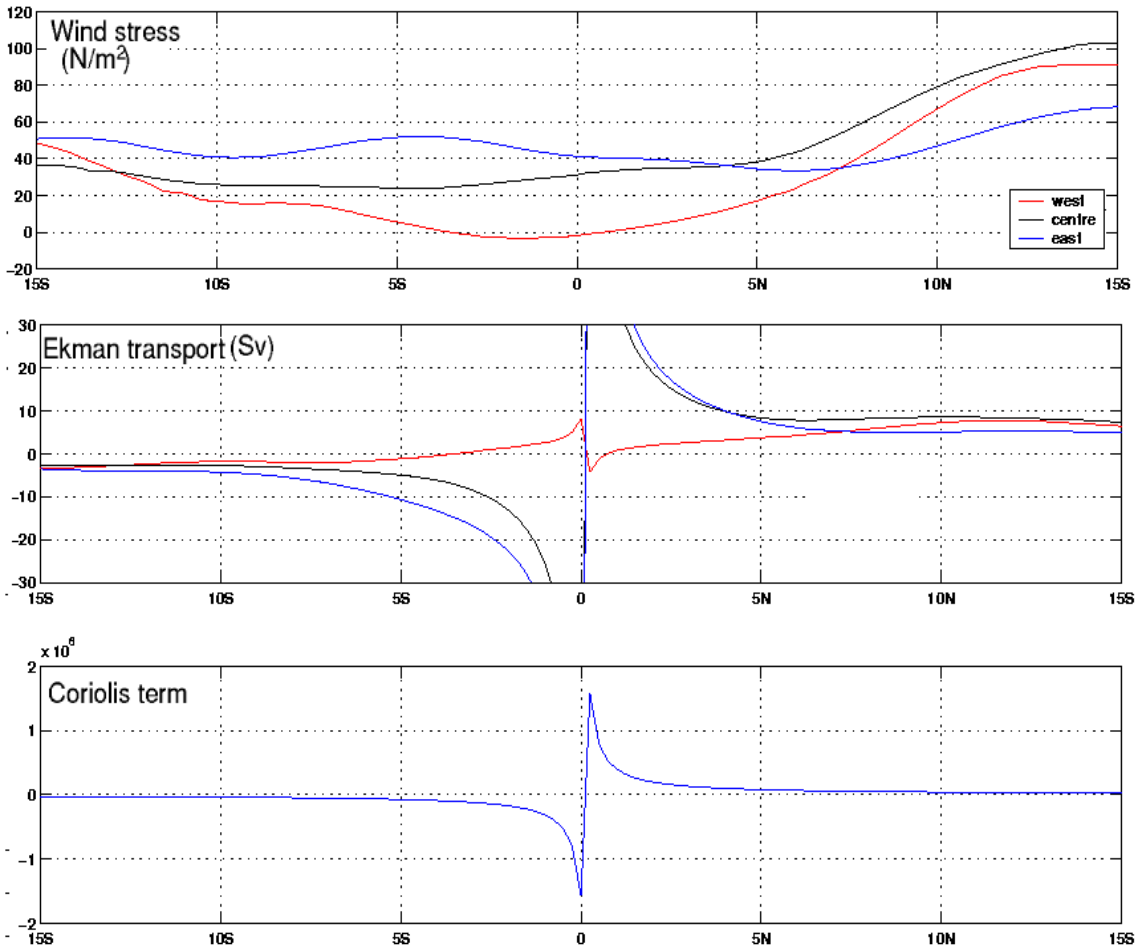

Figure 4.6: Wind stress (top) and zonal integral of the Ekman transport (middle) as a function of latitude for the East (blue), Central (black) and West (red) Tropical Pacific regions. Bottom figure is the inverse of the Coriolis parameter as a function of latitude.

in the Central Pacific. This weakening is associated with downwelling into that area and its contribution to the poleward transport.

To further understand some of the mechanisms that drive the volume flow in these regions and the subsequent regions I first analyze the Ekman transport in the regions under study.

4.4 Ekman Transport

The wind stress over the ocean induces mass transport, which is confined to the first few meters of the ocean, usually in the mixed layer. This transport is called Ekman transport. If one assumes a wind blowing on a flat ocean surface with no horizontal pressure gradients, no acceleration and no internal friction, the only forces to be balanced in

the equation of motion are the Coriolis force and the frictional term represented by the wind stress, i.e.:

$$\frac{1}{\rho}\frac{\partial \tau_x}{\partial z} = -fv \tag{4.2}$$

where τ_x is the wind stress over the ocean and f is the Coriolis parameter. A similar expression can be derived for the meridional component. Integrating from the surface to some depth z, below which the effect of the wind is no longer felt, one gets the steady-state relationship:

$$\tau_x = -T_y f \tag{4.3}$$

where $T_y = \int_0^z \rho v dz$ is the meridional mass transport, known as the Ekman transport. From this, T_y can be expressed as:

$$T_y = -\frac{1}{f}\tau_x \tag{4.4}$$

The model calculates the Ekman transport using the monthly average ECMWF wind stress climatology calculated by (Siefridt and Barnier, 1993).

Figure 4.6 shows the zonal integral of the Ekman transport (top) and the wind stress, τ_x (middle) for the East, Centre and West regions as a function of latitude. The bottom panel represents the inverse of the Coriolis parameter, $\frac{1}{f}$. In all these regions the wind stress is seen to be asymmetric about the equator. In the East Region the wind stress is almost constant from 15S to 5N, $5Nm^{-2}$, and increases to $7Nm^{-2}$ at 15N. The Central region has almost a constant wind stress of $3Nm^{-2}$ from 15S to around 4N, then it increases to $10Nm^{-2}$ at 15N. In the West region the wind stress decreases from $5Nm^{-2}$ at 15S to $0Nm^{-2}$ at 4S, then it reverses sign up to around 1N, and increases to $9Nm^{-2}$ at 15N.

The top panel of the figure shows that the Ekman transport in the east and central regions decreases poleward from the equator. The rate of decrease is given by the variation in latitude of the inverse of the Coriolis parameter (bottom part of the figure).

The Ekman transport in the west shows convergence close to the equator. This is due to the mean westerly winds found in this region. Very close to the equator (1N to 4S) the negative wind stress induces equatorward Ekman transport. Away from the equator, the mean wind changes direction and the increase in the Ekman transport is dominated by the increase in the wind stress.

In the east region the wind stress is weakest around 6N. In all the regions it is stronger farther north. In the central region the stress is almost always larger than in the west region, except for the latitudes between 15S and 12S, where it is slightly stronger in

the west. The latitudinal variation of the wind stress shows a minimum around 6N in the east, 5S in the centre and around 3S in the west region.

The horizontal distribution of the wind stress is the result of the asymmetry of the Intertropical Convergence Zone (ITCZ), which is found at about 10N in the East Pacific in the time mean. This is a region of marked Ekman convergence in the atmospheric boundary layer, and hence one of Ekman divergence in the ocean.

Figure 4.7 shows the integrated vertical velocity for the East, Centre and West Regions as a function of latitude. The East Region shows a maximum of downwelling centred at 5N, with a latitudinal extent of two degrees. This is a region where the poleward decrease in Ekman Transport reaches an almost constant value (figure 4.6), which results in downwelling due to variations in the coriolis parametre. The reason for this sharp downwelling is associated with the boundary between the NECC and NSEC (figure 4.3). South of the equator the decrease in Ekman transport is less sharp, due to the nearly constant wind stress, generating uniform downwelling from 3S to 7S. The figure shows that equatorial upwelling extends from around 1S to around 4N. It has a maximum nearly centred at the equator and a second maximum around 3N; this becomes clearer at level five.

In the Central region, the upwelling is also centred at the equator but is less intense than in the East Region, it extends from 1S to 2N approximately. The downwelling is confined close to the equator with its northern branch less intense than in the East, extending from 3N to 7N with a minimum at around 4N. The southern branch of the downwelling starts at 1S, and has an absolute maximum at around 2S, which is more intense than the downwelling in the East. Then it decreases until around 8S.

The West region presents weak upwelling and downwelling north and south of the equator, respectively. This is generated by the reversal of the wind stress near to the equator, which generates divergence north of the equator and convergence south of the equator. This vertical motion is confined to the first three levels of the model.

Overall, the latitudinal decrease of the inverse of the Coriolis parameter is the dominant term in the decrease of Ekman transport in the Centre and East Regions. Meanwhile the poleward increase of the wind stress increases the Ekman transport in the West Region.

The zonal variation of the poleward Ekman transport is a consequence of the variation of the wind field, which intensifies from west to east and from 12S to 4N (figure 4.6). Further north the wind stress is more intense in the Central Region. This poleward variation generates Ekman convergence and induces downwelling.

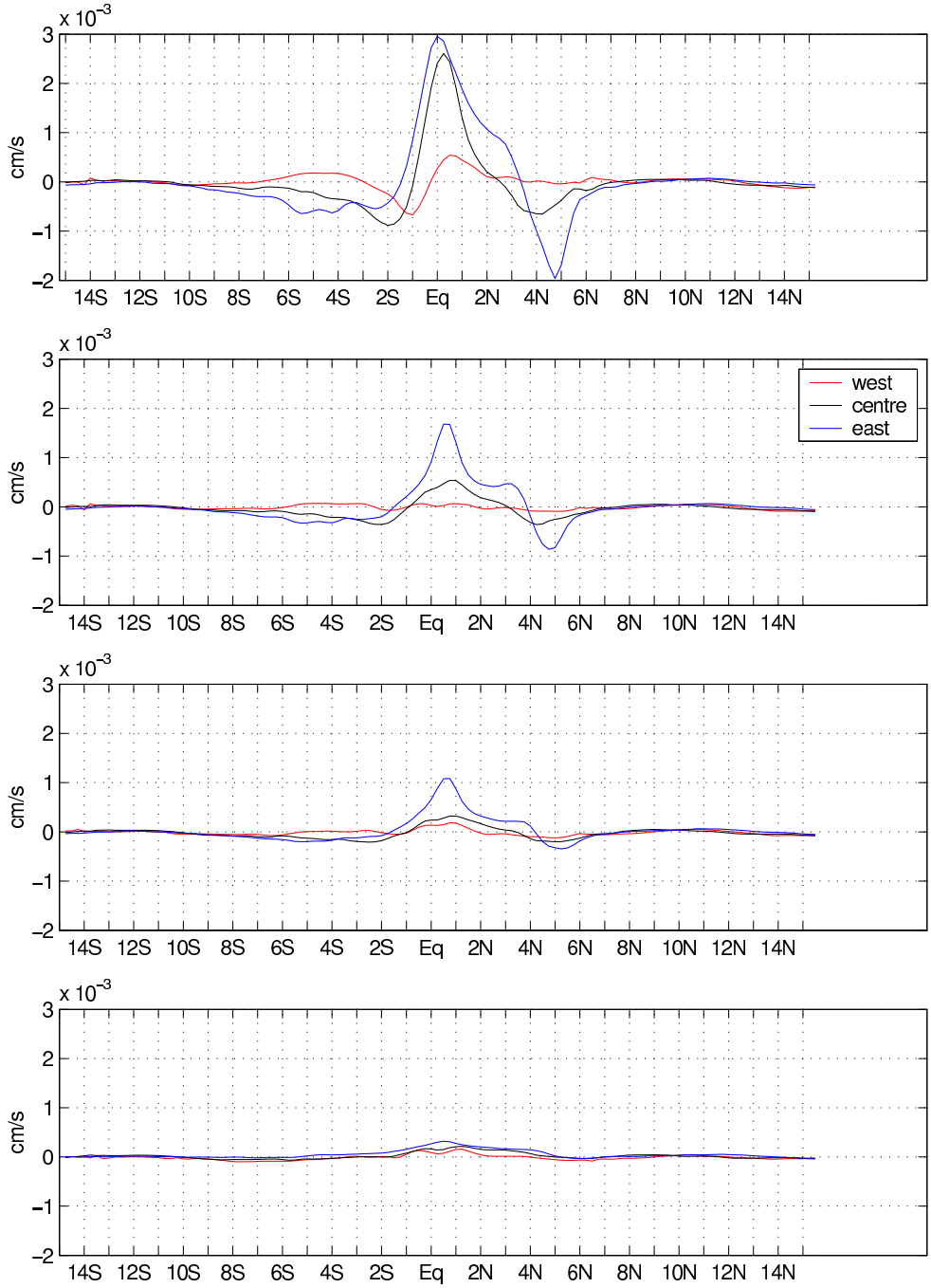

Figure 4.7: Zonal integral of the vertical velocity for the East (blue), Centre (black) and West (red) regions as a function of latitude. The velocities are defined at the bottom of levels three, five, six and nine (52.35m, 102.04m, 130.97m and 244.55m).

4.5 Volume Transport within the Tropical Pacific

Figure 4.8 shows the volume transport in the East, Centre and West Regions for each of the meridional regions described in section 4.2. Each panel consists, from south to north, of the: SECC Region (7S - 12S); SEC Region (1S - 7S); EUC or Equatorial Region (1S - 2N); NSEC Region (2N - 5N); and NECC Region (5N - 10N). The top panel represents the Mixed Layer Box, the middle panel the Subsurface Box and the last panel the Bottom Box.

4.5.1 Upwelling and Downwelling

As discussed earlier, the Ekman transport generates upwelling at the equator, which decreases from east to west due to the weakening of the winds. Figure 4.8 shows strong upwelling into the mixed layer in the Equatorial Region.

In the East Region, where the wind stress is stronger, the upwelling into the mixed layer is stronger as well, with an inflow from the subsurface box of 23.16Sv, which is confined from 1.625S to 3.625N (figures 4.8 and 4.7). This upwelling starts at level nine and has a considerable increase at level five and six, where the core of the EUC is found in OCCAM. This upwelling has a maximum at 0.625N, and at level five shows a second maximum at around 3N. From figure 4.7 it can be observed that at 3.625N the vertical velocity changes sign. This is a boundary between upwelling and downwelling into the mixed layer box, which lies in the NSEC Region. The same figure shows a strong and narrow downwelling centred at 4.875N, which is the limit between the NECC and NSEC Region. Figure 4.8 shows that the NSEC region downwells 4.13Sv into the Subsurface Box and the NECC downwells 4.39Sv. South of the Equatorial Region, there is not a narrow downwelling zone, instead it is spread through the SEC and SECC Regions, contributing with 8.88Sv and 2.37Sv respectively. The downwelling from the NECC Region persists until the bottom of the Subsurface Box. In the NSEC Region the downwelling is less deep and at the bottom of the Subsurface Box there is upwelling.

The Central Region shows a weaker upwelling into the mixed layer, 15.27Sv, which has a narrower extension than in the East Region. It narrows, from 1S to 5N at level eight to 1S to 2N at level three, figure 4.7. At level four the downwelling strengthens considerably, nearly reaching the same intensity as the east region at level three. In the north it is mainly concentrated in the NSEC Region, with a contribution of 4.05Sv compared with 0.82Sv from the NECC Region. The downwelling in the south has

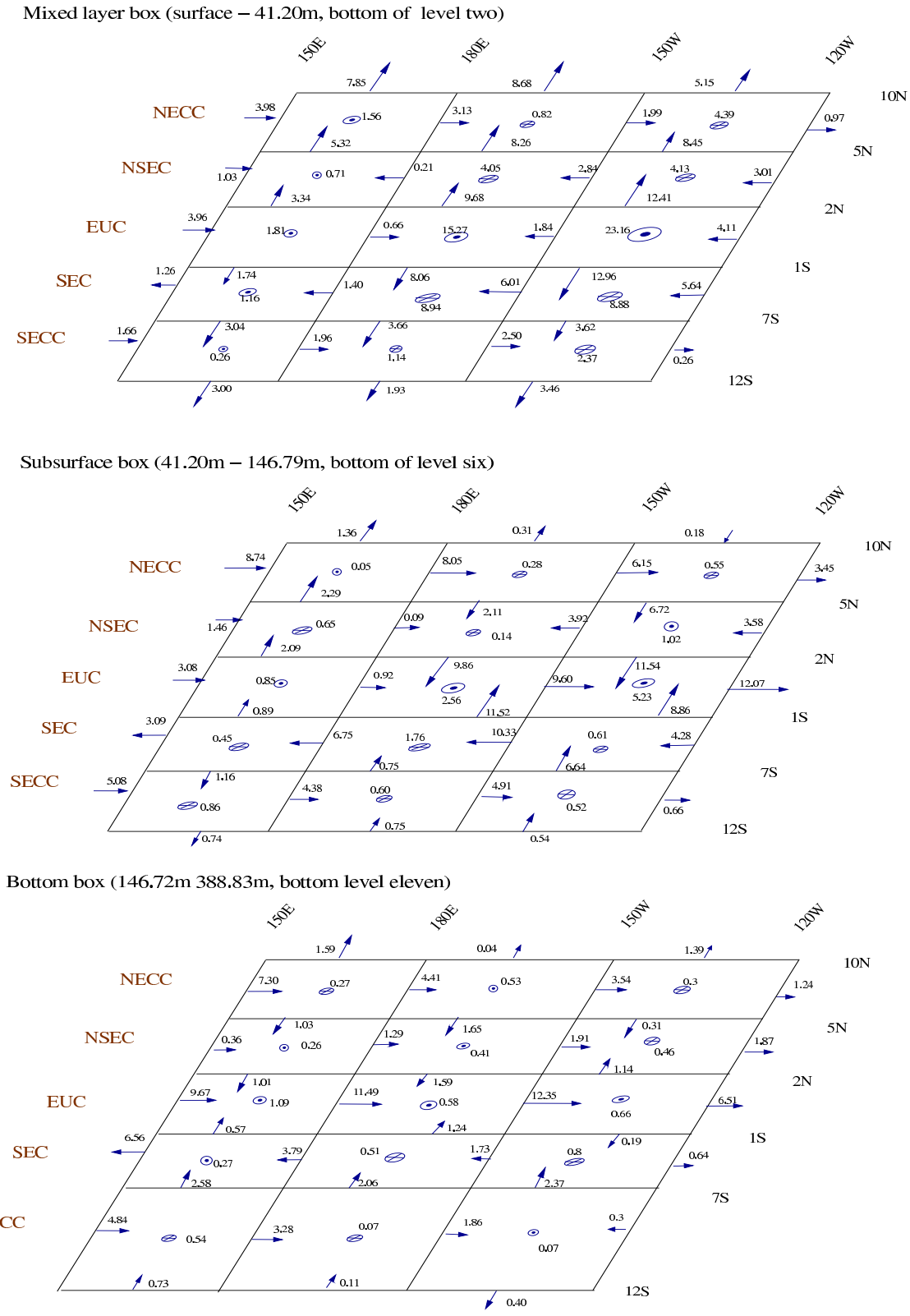

Figure 4.8: Volume transport (in Sv) in the East, Centre and West for the meridional regions under study (see text), for the mixed, subsurface and bottom layers. The arrows represent volume flow out or in of the corresponding wall of the box. The dot or cross in the middle of each box represents upwelling or downwelling, respectively, at the bottom of the box.

a similar contribution than the one in the East Region, 8.94Sv come from the SEC Region and 1.14Sv come from the SECC Region.

The West Region is characterized by weak downwelling south of the equator in the limit between the Equatorial and SEC Regions amounting to 1.83Sv. Between 0.125S and 1.875N there is weak upwelling of 2.41Sv into the mixed layer box (figure 4.7).

4.5.2 Meridional Transport

The vertical flow into the mixed layer is mainly balanced by poleward transport in the East and Central Regions. The meridional surface flow (equation 4.1) is the sum of the Ekman transport (equation 4.4) and the geostrophic flow component, which is calculated as a residual. These three components are shown in figure 4.9 for each meridional wall of the mixed layer boxes.

Figure 4.9 shows that in the East Region the Ekman transport across 1S is twice the one across 2N (46.89Sv and 21.73Sv respectively). On the other hand, the meridional transport at both latitudes is almost the same, around 12.50Sv. This is associated with the stronger geostrophic flow from the SEC Region. It is observed from the figure that the poleward transport decreases faster with latitude in the south than in the north. This is associated with downwelling from the SEC and SECC Regions and with the equatorward geostrophic flow, which persists until 12S. In the south the meridional transport is always weaker than the Ekman transport, whereas in the north both transports are almost the same in the NECC Region.

In the Central Region, close to the equator, the poleward transport at the surface is one quarter of the Ekman transport at 1S and half of it at 2N. The outward flow from the NSEC, SEC and NECC Regions are almost equal to the Ekman transport. South of the SECC the meridional transport weakens due to a geostrophic flow component.

In the West region, the poleward transport increases due to the prevailing winds in the area. This transport is always stronger than the Ekman transport, except in the vicinity of 1S, where the winds reverse sign. The poleward geostrophic component balances the Ekman transport.

Below the direct influence of the wind, in the subsurface box, there is equatorward geostrophic flow in the East and Central Regions (figure 4.8). This flow has a weak component at 10N and 12S and increases considerably equatorward due to the downwelling from the NECC, NSEC, SEC and SECC Regions. In the East Region, the increase is stronger in the NSEC Region, from 6.72Sv to 11.54Sv. Meanwhile in the

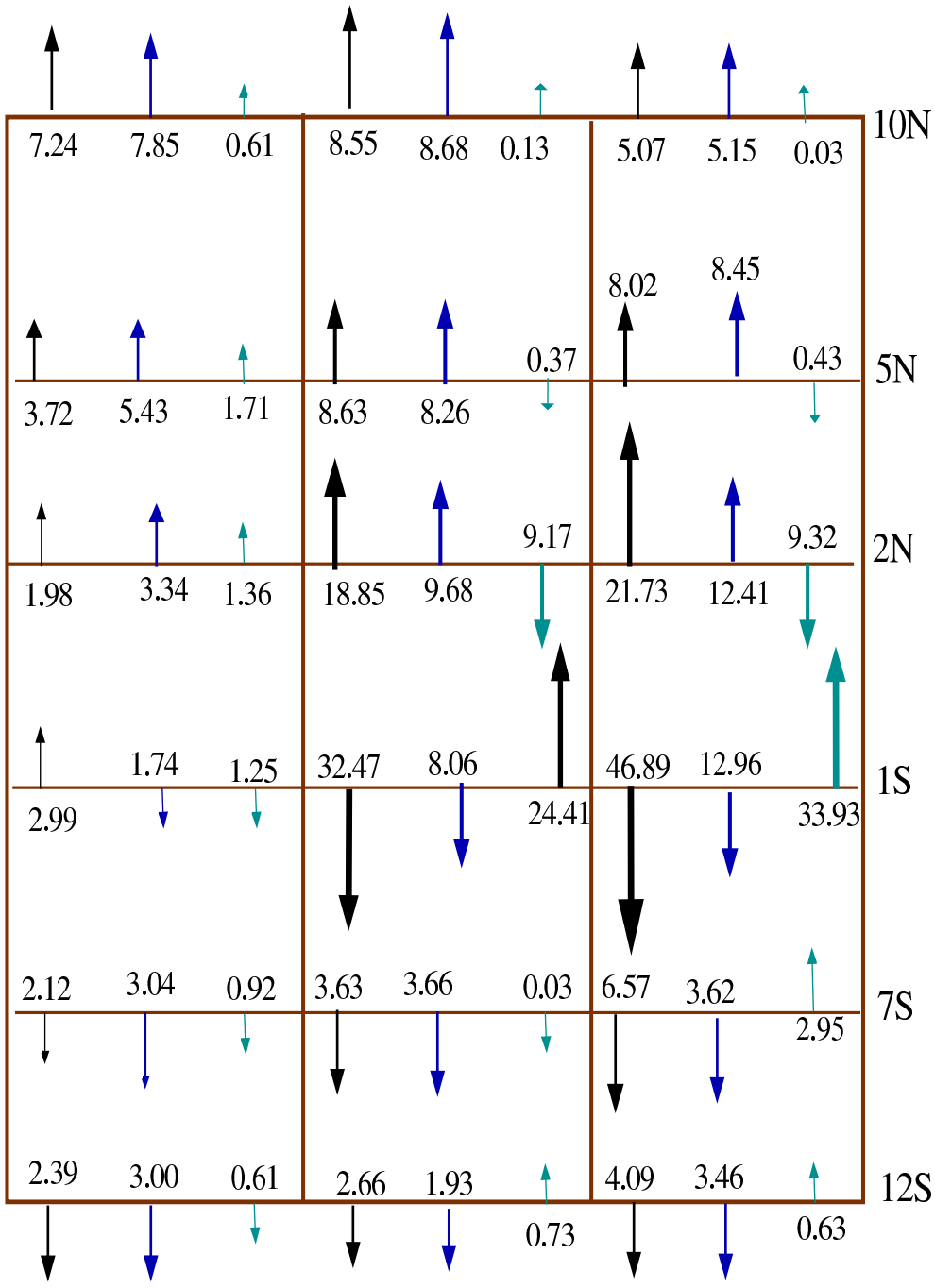

Figure 4.9: Meridional transport at the surface (Sv). Ekman transport (black arrows), total meridional flow (blue arrows) and geostrophic flow (magenta arrows) for each of the latitudes under study.

SEC Region it just increases from 6.64Sv to 8.86Sv. In the Central Region the equatorward flow is stronger in the south than in the north of the Equatorial Region, 11.52Sv and 9.86Sv respectively. This inflow intensifies due to downwelling and zonal transport from the SEC and NSEC Regions. The West Region exhibits divergence centred in the SEC Region, which increases northward up to 5N and then decreases. Southward it decreases as well.

4.5.3 Zonal Transport

At the equator, where the Coriolis force vanishes, the primary forces that need to be in balance are the pressure gradient and the wind stress. Any imbalance will result in a current which will accelerate until restrained by viscous forces. Figure 4.8 shows that in the west of the Equatorial Region there is an eastward current, which flows down the pressure gradient, as a consequence of the weakening of the the wind stress in the area. This current decreases from 3.96Sv across 150E to 0.66Sv across 180E. On the other hand, there is a westward current in the East Region, which is part of the SEC. This westward current is associated with a wind stress stronger than the pressure gradient and decreases in transport from 4.11Sv across 120W to 1.84Sv across 150W.

The SEC extends from 5N to 7S in the first few metres of the ocean (figure 4.3). Its total westward transport, which in the mixed layer is split in the NSEC, Equatorial and SEC Regions, weakens from 12.61Sv across 120W to 10.69Sv across 150W. This westward current just persists in the SEC Region through all the regions. It weakens westward mainly due to downwelling and poleward motion in the Central Region. The SEC extends down to the bottom of the subsurface box in the East and Centre; in the West it extends down to the Bottom Box. Through the whole water column it transport 9.92Sv across 120W, increases to 18.06Sv at 150W, then decreases to around 11Sv through the West Region. The northern branch of the SEC, the NSEC, just persists into the subsurface box, with an average transport of 6.59Sv at 120W, then it decreases to 3.76Sv across 150W and to 0.30Sv across 180E.

Below the mixed layer, between the two branches of the SEC, the EUC dominates the eastward transport in the Centre and East Regions. This transport increases on its way due to meridional convergence into the subsurface box. It increases from 9.60Sv across 150W to 12.07Sv across 120W. In the West Region the eastward transport at this level is not part of the EUC, but part of eastward transport in the mixed layer box.

The SECC and NECC Regions have eastward transport in the three vertical boxes.

The SECC intensifies in the mixed layer box from 1.66Sv across 150E to 2.50Sv across 150W due to meridional inflow, then it weakens due to downwelling in the east. In the rest of the column it weakens from west to east due to equatorward transport. It has an average transport of 11.58 Sv in the West region and of 9.44Sv in the Central Region. The NECC decreases eastward, from 18.47Sv across 150E to 4.97Sv across 120W. It mainly weakens due to meridional processes. In the Bottom Box there is a weak eastward transport in the NSEC and SEC Regions, which corresponds to the weak subsurface countercurrents SSCC.

4.5.4 The Equatorial Undercurrent Transport

To understand how much of the upwelling in OCCAM is due to the tilt of the EUC and how much due to other processes, I split the EUC Region into the model levels. Figure 4.10 shows the volume transport from levels one to eleven in the East, Centre and West region of the EUC region. It shows that in the West Region, below the warm pool (201.13m-355.07m, levels eight to eleven) the flow at each level across 150E has an upward and eastward component.

This upward component is part of the EUC tilt, which flows across 180E at the above level. For example at level nine (244.55m), from the 2.27Sv of inflow across 150E, 0.78Sv flow upward and 1.49Sv flow eastward. This eastward flow joins the meridional convergence (0.55Sv) and the upwelling across the bottom (1.03Sv), to sum 3.09Sv across 180E. The upwelling into this level (L9) comes entirely from the eastward flow across 150E at level ten (295.43m). In analogy, the 0.78Sv of upwelling into level eight leaves as eastward flow. At level seven all the flow from 150E flows upward. This level seems to define the beginning of the EUC at this longitude.

In the Central Region from level nine to eleven (244.55m-355.07m) the inflow across 180E has an eastward and upward component, similar to that described for the West Region. The eastward component weakens at level eight (201.13m) and just 0.49Sv from the 2.58Sv flows eastward; at level seven (163.67m) all the eastward flow at 180E flows upward. In the East Region, below the core of the EUC (130.97, level six), all the upwelling is due to the tilt of the EUC and all the eastward flow at 120W is due to the upwelling into the level.

In the Central and East regions the meridional convergence joins the flow from the east and leaves as upwelling from 130.97m to 163.67m (levels six and seven), which continues eastward at the level above. In the Centre, at level five (102.04m) the upwelling across the bottom is almost entirely due to the meridional convergence at level

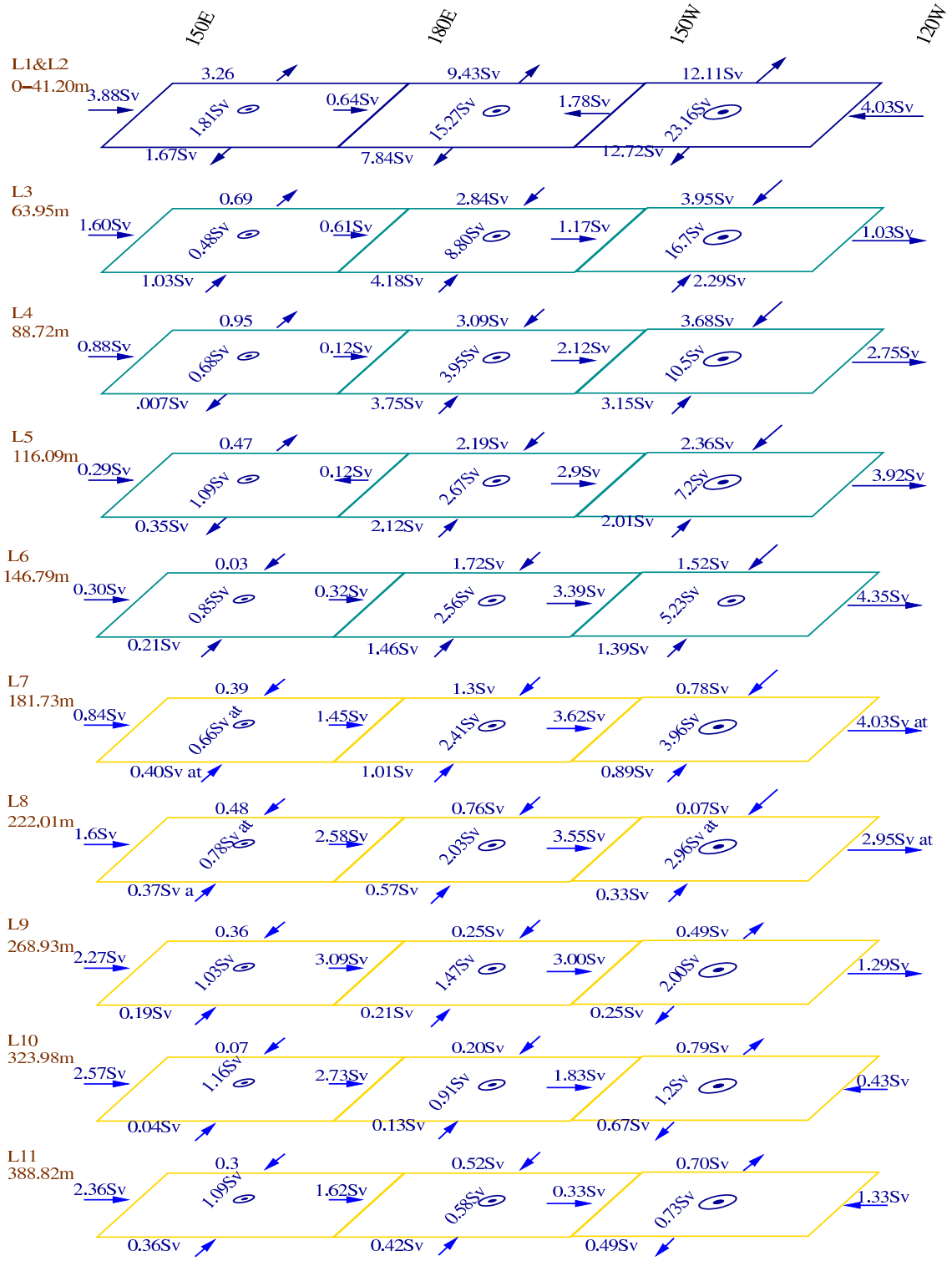

Figure 4.10: Figure showing each of the components of the volume transport from level one to level eleven (9.87m - 355.07m) of OCCAM, at the EUC region (2N to 1S).

six (130.97m). The eastward flow across 150W at L5 upwell into L4 together with the meridional convergence.

From level two to five (30.43m to 102.04m) in the Central region and from level two to four (30.43m to 76.05m) in the East region the upwelling across the bottom at each level is entirely due to meridional convergence, which sustains the EUC from levels three to five (52.35 to 102.04m).

Above the core of the EUC (levels three to six, 52.35m to 130.97m) the meridional convergence is similar in the Central and East regions, meanwhile the upwelling is always considerably stronger in the East region. In the Centre the meridional convergence is the only contribution to upwelling, meanwhile in the east the upwelling is due to the meridional convergence plus the eastward flow from the Centre, which is part of the EUC.

To sum up, below level six (130.97m) all the upwelling into each level is due to the tilt of the EUC in the East, Centre and West Regions. This upwelling, which leaves as eastward flow, contributes to the upwelling in the level above, as it flows eastwards. The latter holds for the West and Central Regions at level six (130.97m); in the East, around 70% of the upwelling is due to the EUC tilt and the rest is due to the meridional convergence at level seven (163.67m). In the Centre, from level two to five (30.43m-102.04m) 90% of the upwelling is due to the meridional convergence from the level below. The part of the upwelling that leaves eastwards sustain the EUC further east. In the East Region, at levels three and four (52.35m-76.05m), all the EUC is entirely due to the meridional convergence at the Central Region. The upwelling due to the tilt of the EUC at these levels contributes 10 and 20% of the flow. The rest of the upwelling comes from the meridional convergence, which strengthens as it flow upward, reaching a maxima at the East at the bottom of level two (30.43m).

4.6 Tropical Cells in OCCAM

As discussed earlier, the meridional transport at the surface is dominated by poleward Ekman transport. Zonally, the easterly trade winds drive a westward surface flow that produces an eastward pressure gradient force. This eastward pressure force produce equatorward geostrophic flow within the thermocline. The equatorial upwelling near the equator and downwelling north and south of the equator, at the convergence zones, produce meridional circulation cells known as Tropical Cells. Using figures 4.8 and 4.7 an idealized sketch of the meridional circulation cells was constructed within OCCAM

for the East, Centre and West regions (figure 4.11).

4.6.1 East Tropical Cells

The top part of figure 4.11 shows the meridional circulation in the East Region according with the model for the year under study. It shows two well defined Tropical Cells in OCCAM where the upwelling of 24.51Sv extends from 1.375S to 3.675N. As already shown, this upwelling leaves the surface as poleward transport, 25.37Sv. The difference between both transports is provided by the zonal SEC. The northern branch of the TC has a meridional transport of 12.41Sv; from which 9.90Sv sink at 5N in a well defined downwelling zone, which extends over just two degree in latitude. Equatorward there are 11.54Sv, partially due to downwelling and partially due to the equatorward transport coming from the NECC Region, generated by the decrease of the zonal flow.

In the south, the poleward transport decreases from 12.96Sv close to the equator to 3.62Sv at 7S. Part of this flow contributes to the downwelling of 11.25Sv, which takes place from 1.5S to 8S and is the main source of the 8.86Sv flow toward the equator. Then, the total convergence toward the EUC Region is of 20.40Sv. This transport is weaker than the upwelling into the mixed layer, which is balanced by zonal flow.

The northern branch is stronger. It has a second maxima of upwelling around 3N and it recirculates 100% of the downwelling back to the equator. The southern branch just recirculates 80% of the downwelling flow.

4.6.2 Central Tropical Cells

The TCs in the Central Region are weaker than in the East Region. The upwelling has a narrower extension with a transport of 15.27Sv and the meridional divergence is 17.74Sv. The balance between both transports is given by zonal convergence into the mixed layer. The southern cell shows downwelling of 10.08Sv, with the main contribution coming from the Ekman convergence through the SEC and SECC regions; part of it is due to the downwelling from the zonal flow. Around 80% of this downwelling flows toward the equator, which together with flow from the zonal current contributes 11.52Sv of the equatorial convergence. The rest of the convergence, from the northern branch, is 9.86Sv, half of which is due to downwelling and half due to zonal flow. Then, the total convergence is 21.48Sv. The difference between the upwelling and convergence (6.21Sv) strengthens the EUC. The northern branch recirculates around 80% of the downwelling, meanwhile the southern branch recirculates nearly 100% of it.

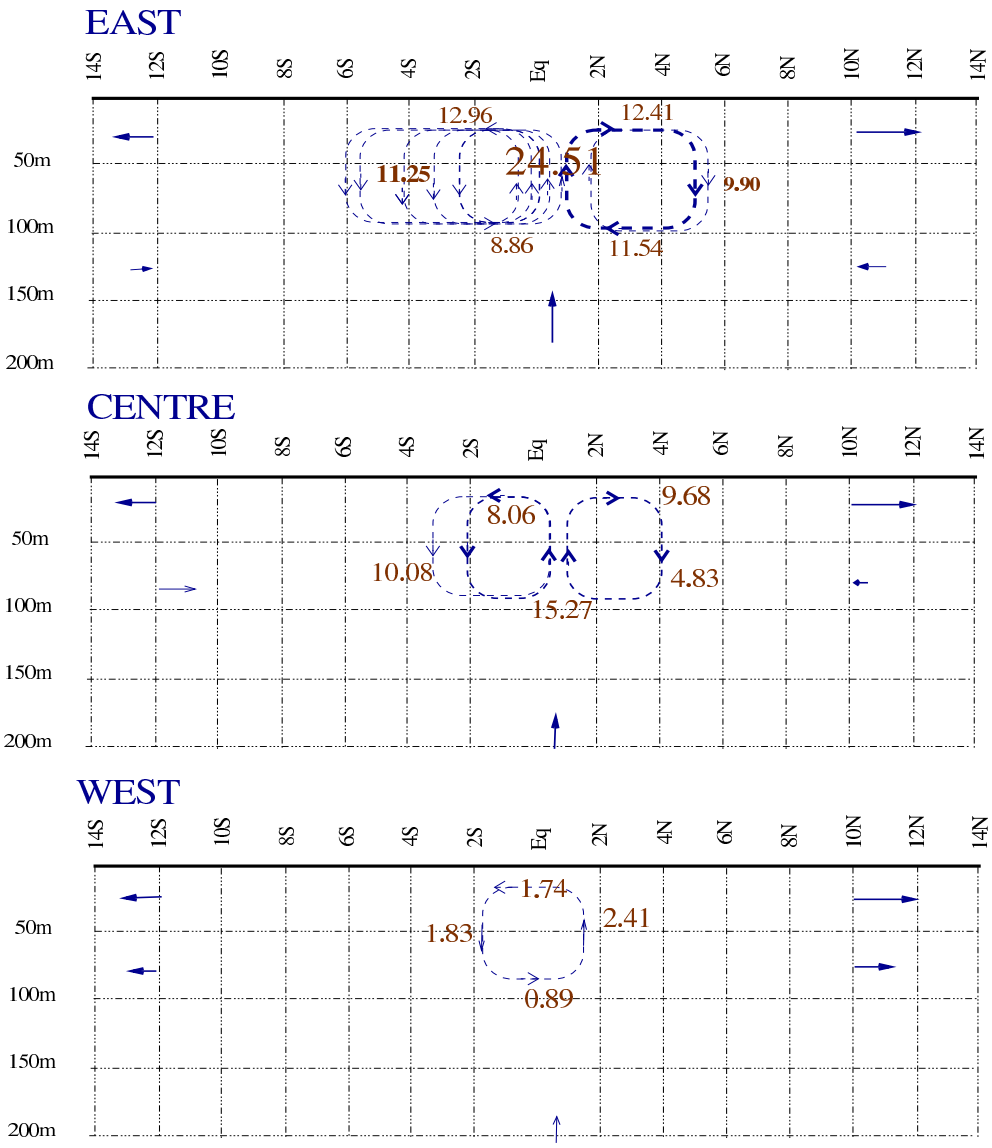

Figure 4.11: Idealized Tropical Cells in OCCAM for the East (top), Centre (middle) and West (bottom) regions.

4.6.3 West Tropical Cells

In the west, there is not a well defined pattern of two cells at each side of the equator recirculating water back to the equator. Figure 4.7 shows that there are two upwelling regions, centred at 4.375S and 0.625N, with 2.67Sv and 2.41Sv of transport respectively. At around 1S there is downwelling of 1.83Sv, with a latitudinal extent of two degrees. The divergence induced by the Ekman transport around 0.625N and the convergence close to the equator generates a weak cell that crosses the equator (bottom panel of figure 4.11). This weak cell flows toward the equator at the surface and northward in the subsurface box.

4.7 Summary and Conclusions

This study shows weaker zonal currents than those reported by Johnson and McPhaden (2001), hereafter JM. The mean zonal currents in their analysis are based in CTD/ADCP data sets at 136W for the upper 400m. JM estimated a transport of 28Sv in the EUC; in OCCAM the EUC increases from 12.41Sv across 180E to 21.95Sv across 150W, then it decreases to 18.58Sv at 120W.

The other two eastward currents, the NECC and SECC weaken along their way. The NECC weakens from 15.59Sv to 11.68Sv to 5.66Sv at 180E, 150W and 120W, respectively; in the JM analysis it transports 14Sv. The SECC is not reported by JM, here it is weaker than the NECC and transports 9.52Sv at 180E and decreases from 5.27Sv to 0.92Sv at 150W and 120W, respectively.

The total SEC, i.e., its components north and south of the EUC and in the mixed layer at the equator, transports 20.62Sv at 120W increasing to 26.67Sv at 150W; JM reported 33Sv. The eastward flow at 120W in the Bottom Box in the NSEC and SEC Regions represents the subsurface countercurrents, SSCC. They transport 1.87Sv and 0.64Sv, respectively, at 120W. Just the northern one exists at 150W, with a transport of 1.91Sv. JM estimated 4Sv and 1Sv for the north and south SSCC, respectively. The surface eastward current in the West Region decreases from 9.53Sv at 150E to 1.88Sv at 180E, due to meridional transports.

Wyrtki and Kilonsky (1984) suggested that the downwelling generated by Ekman convergence might drive the TCs. This study shows strong and sharp downwelling at 5N, which is not fully explained by Ekman convergence. If it were the case, the vertical velocity in the downwelling region should be approximately equal to the rate of change of Ekman transport with latitude, i.e.:

$$w \simeq \frac{\partial E}{\partial y} = \frac{\partial}{\partial y}(\frac{\tau}{f}). \tag{4.5}$$

Figure 4.6 does not show a strong Ekman transport gradient around 5N, which would be necessary for the vertical velocity to be stronger than somewhere else in latitude. Thus, terms such as friction, viscosity and gradient of pressure in the equation of motion must be important in controlling the northern branch of the TC in the East region.

The analysis of the EUC shows that below its core all the upwelling in the model is due to its tilt. At the core, mainly in the East Region, the meridional convergence and the upward tilt the the EUC have a similar contribution to the upwelling. While at the

top levels of the current the upwelling is sustained entirely by meridional convergence.

Using a $3\frac{1}{2}$ layer model Lu et al. (1998) studied the meridional circulation cells that provide the source waters of the EUC. In their study, the Subtropical Cells (STCs) are the primary source of water for the model EUC (around 21Sv) and the TCs contribute 6.8Sv to the EUC. In this analysis the TCs in the Central Region provide 6.21Sv to the EUC. In the East, the equatorward convergence makes a stronger contribution to the upwelling than to the EUC, which contributes with only 2.5Sv.

Here, the TCs in the East Region, recirculate around 80% of the downwelled water in both branches; in the Centre, the southern branch shows an strong recirculation of 100%, meanwhile the northern branch of the cell recirculates just 50%. The rest of the flow mainly joins the zonal currents. Using drifter data Johnson (2001) reported that off-equatorial downwelling around $\pm 4^o$ recirculates about 50% of the upwelled water into TCs. In this analysis the TCs are stronger, although we need to bear in mind that the zonal region here is smaller than in previous studies.

According to Lu et al. (1998), the STCs (mentioned above) are the part of the ocean circulation that brings subtropically subducted water in the thermocline to the equator, where it upwells and moves back poleward in the surface layers. In models, the TCs are shallow, near-equatorial phenomena superimposed on the STC (Johnson, 2001). Here, the equatorward transport at 10N and 12S in the subsurface box is too weak to reach the equator and contribute to the EUC as part of a lower branch of a STC. A reason for this could be that the timescale of a STC to circulate is larger than the period under study here.

This analysis shows that within OCCAM in the region 150E - 120W and 12S to 10N there is more volume being transported northward than southward. Furthermore, the circulation seems to be confined within $\pm 8^o$ latitude, where the zonal currents contribute to the TCs transport. There does not seem to be extratropic volume transport below the mixed layer. This suggests that the exchange of transport between the tropics and extratropics occurs in the boundary currents (not considered here) and/or with longer timescales than the one used here. It could be as well that the zonal currents play a role in this exchange at the boundaries.

Chapter 5

Verification of the heat balance analysis

5.1 Introduction

A good estimate of the fluctuation terms in a heat budget analysis is crucial to understand the physical processes that occur in the equatorial Pacific circulation. In order to verify if the heat flux analysis computer programs were working correctly I calculated the sum of the heat fluxes due to advection and diffusion into a column of the ocean located at (110W, 4.625N) and checked if the heat flux into it is consistent with the rate of change of heat content in the box. This was done for every analysis timestep during one year.

5.2 The fluctuation term

The best estimate of the rate of change of heat content was obtained using instantaneous output for the temperature field (left hand side of equation 5.1). The heat flux due to advection and diffusion are computed using 5-day mean datasets (right hand side of equation 5.1):

$$\frac{\partial Q_{tot,t_i}}{\partial t_i} = \bar{F}_{tot,t_i} + \bar{D}_{tot,t_i} \tag{5.1}$$

Figure 5.1 shows both sides of the above equation for the year under study. For most of the time the two curves follow each other, however there are differences and sometimes they are large. If the calculation has been done correctly, the difference should be given by:

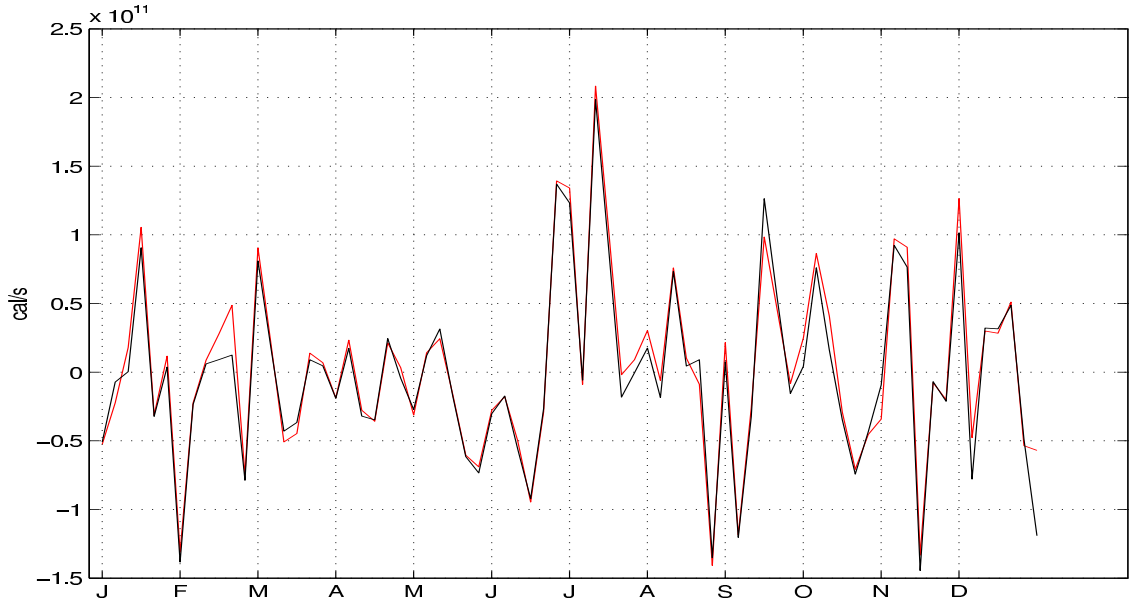

Figure 5.1: Results for a column at (132.625W, 4.125N), from level three to six. Black curve: rate of change of heat content. Red curve: sum of heat flux due to advection and diffusion (red).

$$\frac{\partial Q_{tot,t_i}}{\partial t} - [\bar{F}_{tot,t_i} + \bar{D}_{tot,t_i}] = F'_{t_i} \tag{5.2}$$

where F'_{t_i} represents the contribution due to fluctuations in temperature and velocity within the analysis timestep. Unfortunately, F'_{t_i} cannot be calculated exactly, but it is possible to estimate its size.

5.3 The high frequency term

As the model saved both means and instantaneous values of the tracers at five days intervals, I made use of them to estimate the fluctuation term as a function of time for the year under consideration. As discussed for equations 3.52 and 3.53 the tracer flux can be split into its mean and fluctuating components. I choose to represent the instantaneous values of the temperature and velocity at each analysis time step as a sum of its mean component, given by the 5-day mean field, and a fluctuating component:

$$T(t_n) = \overline{T}(t_n) + T'(t_n) \tag{5.3}$$

$$u(t_n) = \overline{u}(t_n) + u'(t_n) \tag{5.4}$$

where the over bar represents the 5-day mean output and $T(t_n)$ and $u(t_n)$ are the corresponding instantaneous values at t_n. Using the above equations for the fluctuation terms ($T'(t_n)$ and $u'(t_n)$), I estimated the high frequency fluctuating part of the advection, each analysis time step, at each grid point as:

$$u'_{i_{\frac{1}{2}}}(t_n)T'_{i_{\frac{1}{2}}}(t_n) = (u_{i_{\frac{1}{2}}}(t_n) - \bar{u}_{i_{\frac{1}{2}}}(t_n))(T_{i_{\frac{1}{2}}}(t_n) - \bar{T}_{\frac{1}{2}}(t_n)) \tag{5.5}$$

The above expression represents an estimate of the fluctuation due to advection within each analysis timestep, $t_n = 5\,days$, at the interface $i_{\frac{1}{2}}$. The fluctuation term at each wall, l, of the box is the sum of each grid interface fluctuation:

$$u'_l(t_n)T'_l(t_n) = \sum_i u'_{i_{\frac{1}{2}}}(t_n)T'_{i_{\frac{1}{2}}}(t_n) \tag{5.6}$$

where $'i'$ is the sum over the interfaces of a wall $'l'$. The estimate of the fluctuation for the full box, each analysis timestep, is given by the sum of its six walls:

$$(u'(t_n)T'(t_n))_{tot} = \sum_l u'_l(t_n)T'_l(t_n) \tag{5.7}$$

Due to the data availability I do not have $u'T'$ every model timestep, but only once every 5 days. Therefore, I used the 5-day mean values to estimate what $u'T'$ would be if the data every model timestep was available.

I will refer to equation 5.7 as the estimate of the high frequency term, which represents processes of timescale less than five days. This term is an estimate of the error due to the use of the 5-day mean output.

If any physical process has been left out in this analysis, this term is expected to be of the same size as or bigger than the difference between the rate of change of heat content and the sum of heat flux due to advection and diffusion. The latter, the fluctuation term (equation 5.2), corresponds to the 'real' error of the analysis. Then, the relation between both terms should be:

$$|F'_{t_i}| \leq |\int u'(t_i)T'(t_i)dt| \tag{5.8}$$

where the left hand side is equation 5.2 and the right hand side is the estimate of the high frequency term (equation 5.7).

Figure 5.2 shows both terms of the above expression (before the modulus) at one location for the year under study. It shows that the estimate of the high frequency

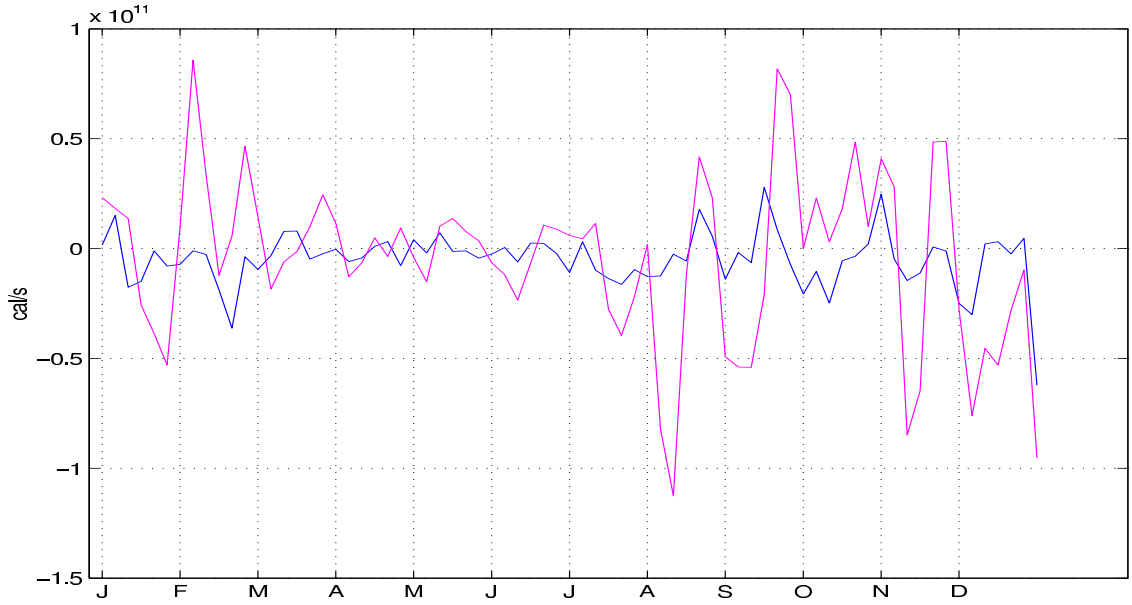

Figure 5.2: Plot showing the difference between the rate of change of heat content and the sum of heat flux due to advection and diffusion (blue) and the estimate of the high frequency term (magenta) based in the five day mean values. For a single column at (110W, 4.625N).

term (magenta line) is bigger, almost all the time, than the fluctuation term (blue line). This result helps to confirm the assumption that the fluctuation term is due only to the flux due to the high frequency variations in the temperature and velocity, and no other major physical term has been left out.

5.4 Variations in space

To confirm that the above analysis holds in a bigger region of the ocean, I repeated the above analysis for two of the large regions under study (described in section 4.2). The results for the first region, located in the east part of the NSEC region (110W - 150W, 2.625N - 4.625N, 41.20m - 146.79m), are shown in figure 5.3. The top part of the figure shows the rate of change of heat content (black) and the sum of the heat flux due to advection and diffusion (red). As with a single column, both terms follow each other most of the year. However, from July onward the sum of the heat fluxes is considerably bigger (warmer) than the rate of change of heat content. The difference between both terms is expected to be of the same size as the estimate of the high frequency term for this region.

Figure 5.4 shows the difference between the rate of change of heat content and the sum of heat flux due to advection and diffusion, i.e. the fluctuation term, and the

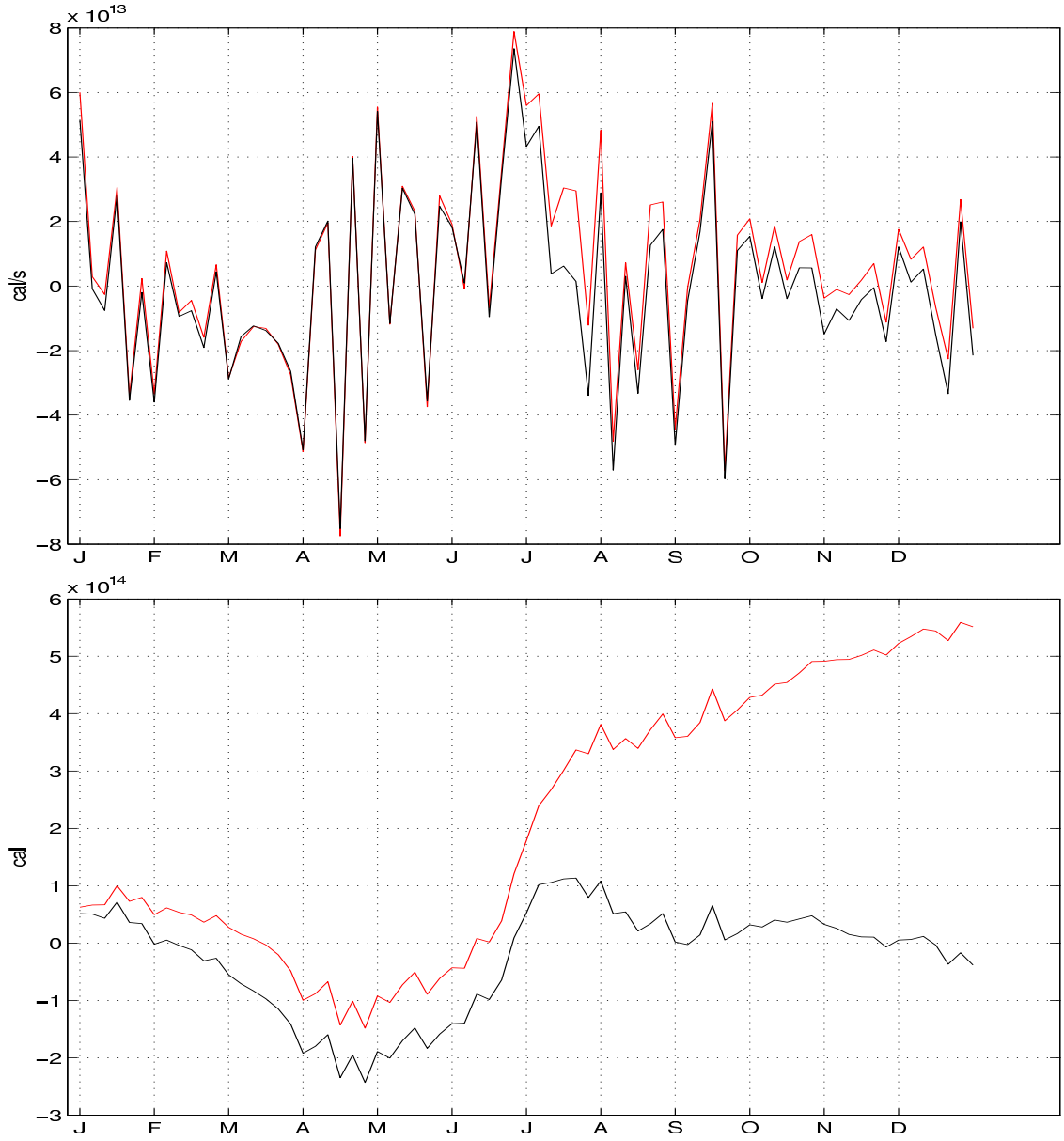

Figure 5.3: Top: Rate of change of heat content (black) and sum of heat flux due to advection and diffusion (red). Bottom: integral of the rate of change of heat content (black) and integral of the heat flux due to advection and diffusion (red). For the east NSEC region.

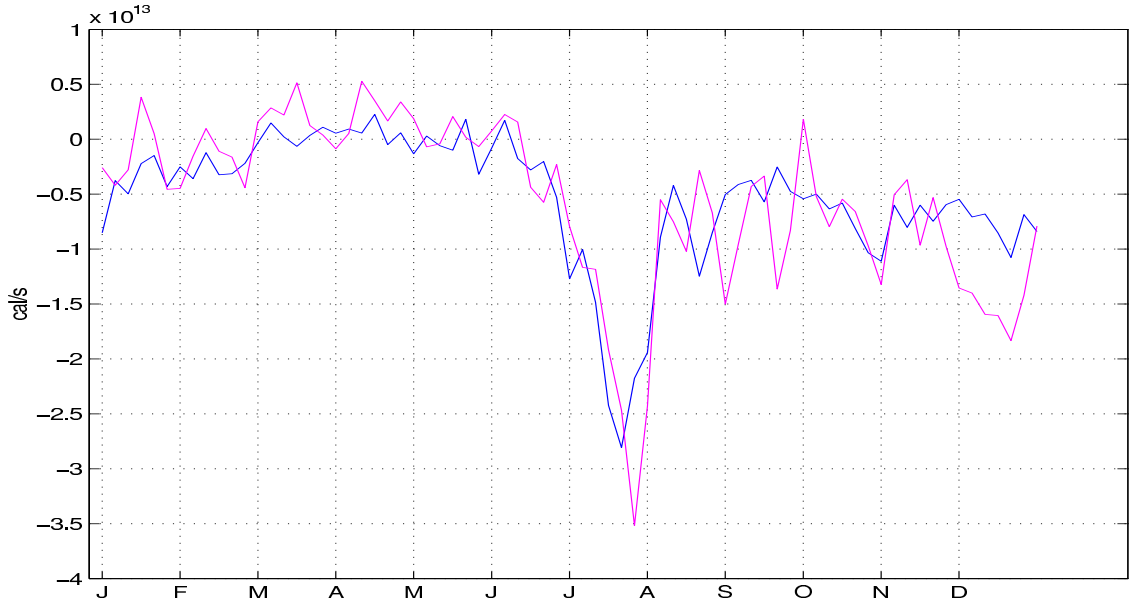

Figure 5.4: Difference between the rate of change of heat content and the sum of heat flux due to advection and diffusion (blue) and high frequency term estimated from the instantaneous values (magenta). For the east NSEC region.

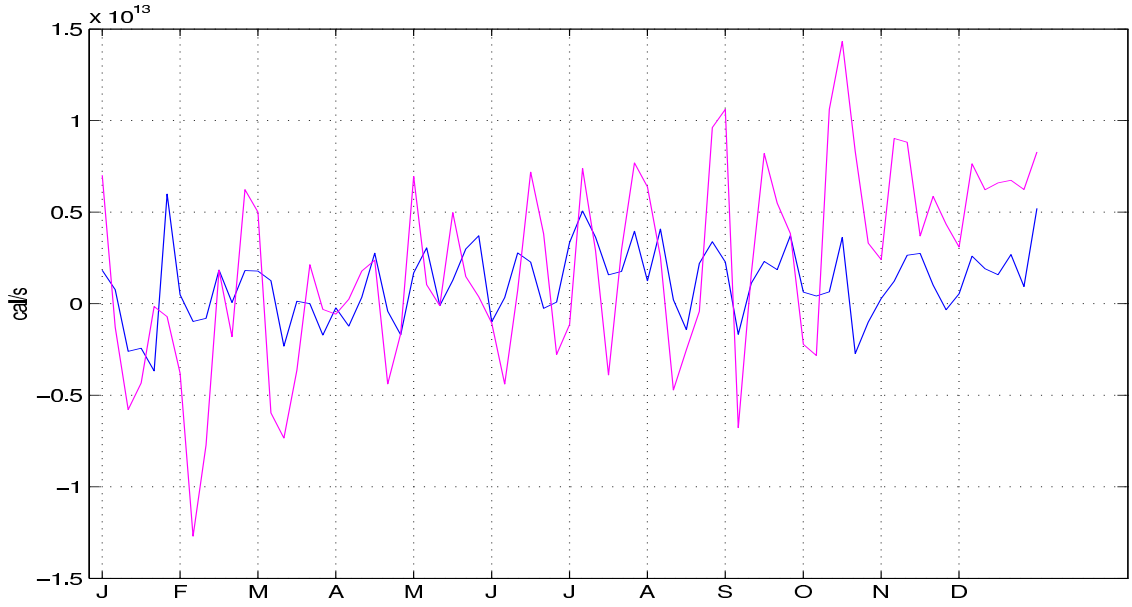

Figure 5.5: Difference between the rate of change of heat content and the sum of heat flux due to advection and diffusion (blue) and high frequency term (magenta). For the east EUC region.

estimate of the high frequency term. It shows that both terms have the same behavior. It is remarkable that at the end of June both terms have a high negative value. The presence of strong downwelling and of the TIWs seems to be the cause of such large fluctuation, which persists during the rest of the year. This shows that the difference between the curves in figure 5.3 is associated with the contribution of the high frequency term. The latter cools the region, in agreement with the apparent excess warming due to the advection and diffusive heat fluxes shown in figure 5.3. This excess warming is best illustrated in the bottom part of the figure, which shows the integral of the rate of change of heat content and the sum of the heat flux due to advection and diffusion.

The second region studied is centred at the equator (110W - 150W, 1S - 2N, 41.20m - 146.79m). Figure 5.6 (top) shows the rate of change of heat content and the sum of the heat flux due to advection and diffusion for this box. In this part of the ocean, cooling due to upwelling competes with warming due to downward diffusion of heat at the top of the box, where stratification is strong, creating a high mixing area. The bottom part of the figure is the integral during the year of both terms. It shows that when using 5-day mean values, the cooling by upwelling appears stronger than the warming by diffusion. This is more evident during the second half of the year. Figure 5.5 shows the estimate of the high frequency term and the fluctuation term for this region. It shows that both terms fluctuate similar to each other most of the time and provide the extra warming required.

5.4.1 Fluctuations in the diffusion term

The OCCAM model uses the Pacanowski and Philander (1981) vertical mixing scheme, and it is known that this can produce highly variable vertical mixing near the equator. As a further check I did an analysis of the vertical mixing parametrization using the 5-day mean and instantaneous datasets. The Pacanowski and Philander (1981) scheme depends on the Richardson number, so I calculated the Richardson number (equation 3.31) used in the vertical mixing coefficient (equation 3.29) using both datasets. This is done for the top and bottom walls of the box located at the equator, each analysis time-step, for every grid point during two periods of time - January to April and September to December.

Table 5.1 shows the number of grid points with Richardson number values in the interval shown in the first column, at 41.20m (top of level three). Columns two and three correspond to values for the first period (January - May) using instantaneous and 5-day mean datasets respectively; column three and four represent the values for the

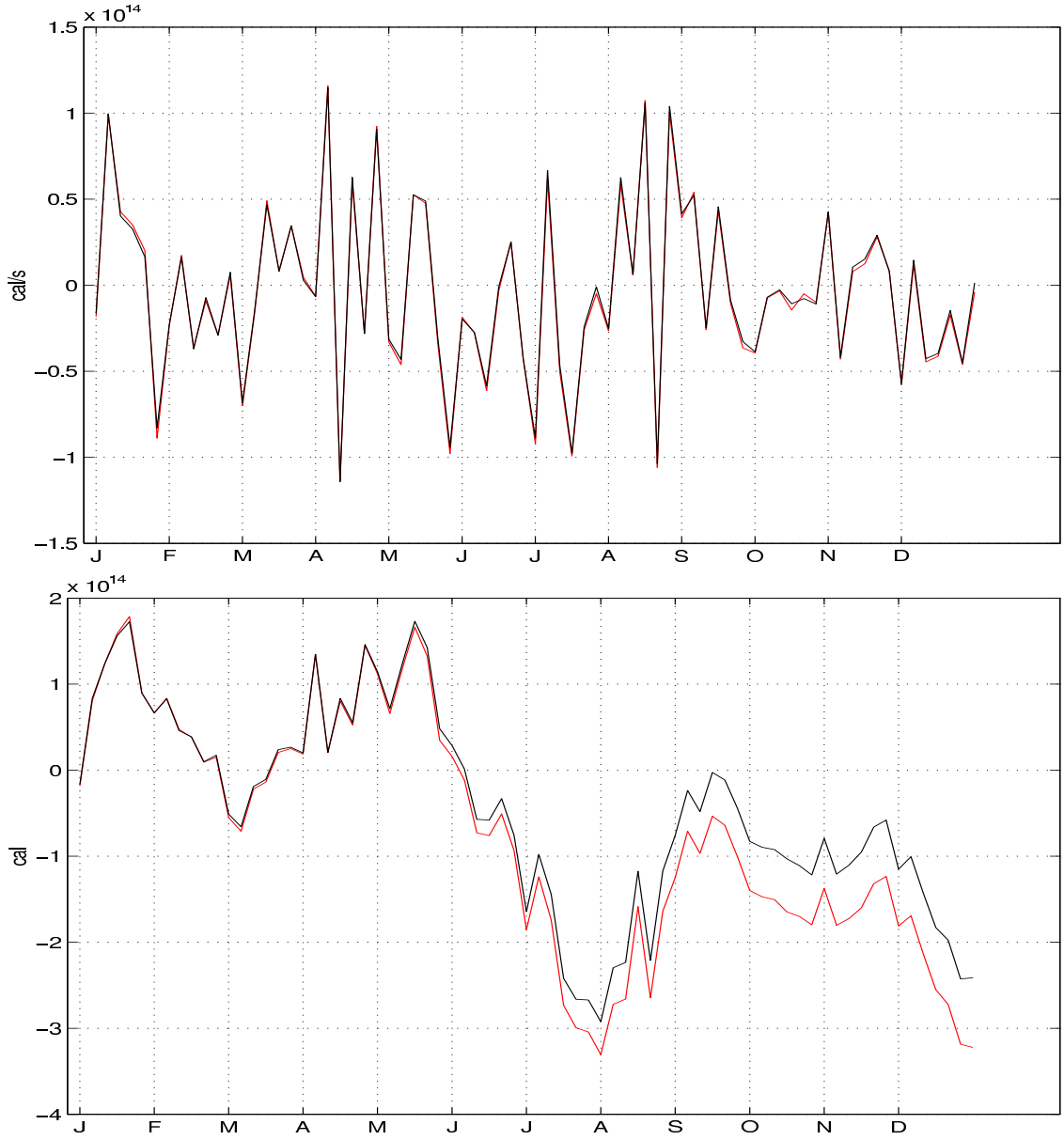

Figure 5.6: Rate of change of heat content (black). Sum of heat flux due to advection and diffusion (red). For the region centred at the equator (110W - 150W, 1S - 2N, 41.20m - 146.79m).

second period (September -December).

In the model, shear flow instabilities, i.e. high vertical mixing, occur at values of $R_i < 0.4$. Values of $R_i > 0.4$ correspond to low mixing. The table shows that the number of grid points with small values of the Richardson number using instantaneous values is one order of magnitude bigger than when using 5-day mean datasets. This is especially true for the range $R_i \leq 0.1$ in the first period and $R_i \leq 0.07$ in the second one. For values corresponding to mixing in the interval: $0.1 < R_i \leq 0.45$ for the first period and $0.07 < R_i \leq 0.3$ for the second one, the number of grid points using

	January- May			September-December	
Ri	instantaneous	5-day mean		instantaneous	5-day-mean
0.001	0	0		0	0
(0.001 0.01]	102	5		214	12
(0.01 0.07]	246	71		421	67
(0.07 0.1]	282	91		469	111
(0.1 0.15]	721	360		2261	1328
(0.15 0.18]	534	527		2181	1918
(0.18 0.19]	206	220		828	758
(0.19 0.25]	1526	1499		5715	5319
(0.25 0.3]	1535	1493		4576	4493
(0.3 0.4]	3153	3007		6796	7423
(0.4 0.45]	1543	1444		2506	2692
(0.45 0.5]	1439	1565		1987	2209
(0.5 0.8]	8589	8856		7271	7683
>0.8	33884	23622		18535	19747

Table 5.1: Number of grid points at level three (41.20m) with values of the Richardson number within the interval shown in the first column, using instantaneous values (column two and four) and 5-day man values (column three and five).

instantaneous fields is still bigger than using 5-day mean, but the difference between both fields is not as contrasting as for high mixing values.

The number of grid points using 5-day mean datasets is bigger than using instantaneous fields for values of the $R_i > 0.45$ in the first period and $R_i > 0.3$ for the second which mainly correspond to low mixing. In this case most of the grid points lie at values of $R_i > 0.8$. Overall, the second period shows more mixing than the first one, which is due to the instability processes at that time.

This analysis shows that the number of grid points with high mixing values is bigger calculating the Richardson number with instantaneous datasets than using 5-day mean fields in the velocity field. As a consequence, the vertical diffusion is underestimated using 5-day mean values, and this is more evident in high mixing regions. Figure 5.7 shows the integral of the sum of the heat flux due to advection and diffusion using 5-day mean and instantaneous values in the Richardson number together with the rate of change of heat content. It is observed that the difference between both terms is considerably reduced with the use of instantaneous values in the Richardson number.

Figure 5.7: Integral of the sum of heat flux due to advection and diffusion using 5day mean values (red) and instantaneous values (green) and the rate of change of heat content (black). For the east EUC region.

5.5 Mean heat fluxes and associated uncertainties

The heat balance analysis discussed in the next chapter is done for a period of one year. Therefore, it is of interest to estimate the mathematical contribution (or analysis error) for such a year. To measure how well the estimate of the high frequency term, represents the actual analysis error (the fluctuation term), I calculated the root mean square (RMS) of the estimate of the high frequency term, for the year under study as:

$$\varepsilon_l = \sqrt{\frac{\sum (u'(t_i)T'(t_i))_l^2}{n-1}} \tag{5.9}$$

where n is the number of datasets during one year.

The estimate of the high frequency term is the error associated to the heat balance analysis. In this case equation 3.51 can be rewritten as:

$$\frac{\partial Q_{tot,\tau}}{\partial t} = \bar{F}_{tot,\tau} + \bar{D}_{tot,\tau} \pm \varepsilon_{tot,\tau} \tag{5.10}$$

where $\varepsilon_{tot,\tau}$ is the RMS of the estimate of the high frequency term of the whole box for the year.

Tables 5.2 and 5.4 show the values of the integral over the year under study of the heat flux due to advection (equation 3.40), the heat flux due to diffusion (equation

box located north of the equator				
interface	advection	diffusion	adv + diff	ε
bottom	82.51	-15.81	66.7	0.43
top	-414.80	-9.93	-424.73	6.30
west	-395.94	0.002	-395.94	-0.032
east	-334.57	-0.0028	-334.57	-0.13
south	-1112.09	-0.93	-1113.02	-11.00
north	-705.38	-0.28	-705.68	-12.13

Table 5.2: Integral over the year at each interface of the box located at (110W - 150W, 2N - 4N, 41.20m - 146.79m) of: the heat flux due to advection, heat flux due to diffusion, sum of the heat flux due to advection and diffusion, and the high frequency term. Units are $10^{12}W$.

advection	diffusion	adv+diff	$\frac{\partial Q}{\partial t}$	$\frac{\partial Q}{\partial t} - \sum F$	rms(hft)
29.21	-6.43	22.78	-2.20	-24.98	39.33

Table 5.3: Mean values for the year under study of: the full heat flux due to advection, full heat flux due to diffusion, total heat flux, rate of change of heat content, fluctuation term and high frequency term for the region at (110W - 150W, 2N - 4N, 41.20m - 146.79m). Units are $10^{12}W$.

3.43) and the estimate of the high frequency term at each wall of the boxes located at (110W - 150W, 2N- 4N, 41.20m - 146.79m) and (110W - 150W, 1S - 2N, 41.20m - 146.79m), respectively. They show that the high frequency term is considerably smaller than the heat flux due to advection. On the other hand, the high frequency term is sometimes smaller and sometimes bigger than the heat flux due to diffusion.

Table 5.3 shows the integral over the year under study of the total heat flux due to advection, the total heat flux due to diffusion, the rate of change of heat content (equation 5.1) and the RMS of the estimate of the high frequency term (equation 5.7) at the NSEC region. In this region, the heat due to advection ($29.21 \times 10^{12}W$) is bigger than the cooling due to diffusion ($-6.43 \times 10^{12}W$), as a consequence the total heat flux into the box is positive ($22.78 \times 10^{12}W$). The actual rate of change of heat content shows slight cooling ($-2.20 \times 10^{12}W$). This discrepancy is compensated by the estimate of the high frequency term ($39.33 \times 10^{12}W$), which is almost of the same size as the absolute value of the difference between the rate of change of heat content and sum of the the heat flux due to advection and diffusion ($-24.98 \times 10^{12}W$).

Table 5.5 shows the integral for the year under study of the rate of change of heat content, the estimate of the high frequency term, the heat flux due to advection and the heat flux due to diffusion for the box centred at the equator. In this case, the diffusion is calculated using 5-day mean and instantaneous datasets in the Richardson number.

interface	advection	diffusion	adv+diff	ε
bottom	410.84	-14.41	396.43	0.17
top	2283.12	-31.05	2252.07	0.72
west	905.13	0.004	905.13	0.026
east	1004.05	0.003	1004.05	-0.108
south	830.96	-0.05	830.91	-0.104
north	-1112.09	-0.93	-1113.02	-2.62

Table 5.4: Integral over the year at each interface of the box located at (110W - 150W, 1S - 2N, 41.20m - 146.79m) of: the heat flux due to advection, heat flux due to diffusion, sum of the heat flux due to advection and diffusion, and the high frequency term. Units are $10^{12}W$.

	advection	diffusion	adv+diff	$\frac{\partial Q}{\partial t}$	$\frac{\partial Q}{\partial t} - \sum F$	high freq term
5-day mean	-28.08	17.63	-10.45	-13.83	-3.38	23.08
instantaneous		18.41	-9.67		4.31	

Table 5.5: Values for the year under study of: the full heat flux due to advection, full heat flux due to diffusion, total heat flux, rate of change of heat content, fluctuation term and high frequency term for the region at (110W - 150W, 1S - 2N, 41.20m - 146.79m). Units are $10^{12}W$.

In this case the results of the analysis using instantaneous fields in the Richardson number shows that the sum of heat flux due to advection and diffusion and the rate of change of heat content is considerably reduced, as shown in last section.

A further analysis of the terms involved in the heat equation is done for the temperature field of the Split-QUICK scheme used in the model. Table 5.6 shows the temperature terms of equations 3.40 and 3.43 for the region centred at the equator. It shows that the Split-QUICK terms for the advection and diffusion heat fluxes are big at the bottom and top walls, compared with the rest of the values.

	adv	adv	diff	diff
	CD	S-Q term	CD	S-Q term
bottom	97.99	0.14	-3.29	-0.30
top	544.45	0.97	-5.83	-0.86
west	216.23	-0.0016	0.004	-0.0001
east	239.86	-0.0012	0.0035	-0.00011
south	198.57	-0.056	0.013	0.0006
north	-265.62	-0.052	-0.21	-0.007

Table 5.6: Table showing the central difference (CD) terms of the advection and diffusion and its corresponding Split-QUICK term (S-Q term) for the region centred at the equator Units $10^{12}W$.

5.6 Discussion and conclusions

The main findings in verifying the code, in order to be sure that the main physical processes had being captured are:

- The differences between long term heat changes in model ocean and fluxes based on five day averages of temperature and velocity can be explained as due to fluctuations at timescales of less than five days.
- The estimates of the advective heat flux through the interfaces of the regions under considerations are good; and the high frequency terms and errors due to the Split-QUICK numerical scheme are small.
- Estimates of the diffusive heat flux through the interfaces are of the same order of magnitude as the high frequency term sometimes and also to the Split-QUICK advection scheme.
- The use of instantaneous values in the Richardson number in high mixing regions gives a better estimate of the heat flux due to diffusion than the 5-day mean field.
- Estimates of the total advective and diffusive heat flux in or out of a box are comparable with the high frequency term.
- Results for ocean are likely to be similar, so fluxes based on average values are unlikely to give good estimates of the total heat change in a region of the ocean.

Chapter 6

Mean Heat Flux in the Tropical Pacific in the 1/4 of degree OCCAM run

6.1 Introduction

In the equatorial Pacific there is a significant transfer of heat into the ocean across the atmosphere - ocean interface. The oceanic processes that redistribute heat in this region are of fundamental importance for climate studies. Regions of strong divergence in ocean heat transport are reflected in high net surface heat flux; among these the equatorial Pacific cold tongue is one of the most persistent and intense regions of ocean heat gain.

The sea surface temperature (SST) is a critical oceanic variable for understanding and predicting climate variability. In the Tropical Pacific, relatively large, climatically significant variations in the SST occur on seasonal and inter-annual timescales associated with the El Nino - Southern Oscillation (ENSO) phenomenon.

The purpose of this study is to examine the physical processes responsible of the distribution of heat in the equatorial Pacific region, the role of the heat flux left by the mean currents in the ocean and the heat flux due to fluctuation terms in the $\frac{1}{4}$ degree OCCAM run. In Chapter 4, I discussed the volume transport in OCCAM for the regions under consideration. This chapter deals with how much heat is being transported by such currents and how heat is distributed within the equatorial region.

6.2 Heat balance equation in the Tropical Pacific

This section studies how well the heat is balanced in OCCAM in the equatorial Pacific ocean. To analyze the contribution of the different components of the heat equation in each region under consideration, I first study the heat gain by advection and diffusion, the rate of change of heat content and the RMS of the estimate of the high frequency term for each region under consideration.

6.2.1 Rate of change of heat content

In the ocean, currents and mixing processes redistribute the heat gain by the atmosphere to attain a heat balance. This implies that if the average temperature of the oceans is to remain constant, the heat gain and loss must balance during each period of time. In this analysis, the rate of change of heat content is compared with the heat gain by advection and diffusion and the estimate of the high frequency term, as discussed in section 5.5:

$$\frac{\partial Q_{tot,\tau}}{\partial t} = \bar{F}_{tot,\tau} + \bar{D}_{tot,\tau} \pm \varepsilon_{tot,\tau} \tag{6.1}$$

Figure 6.1 shows the rate of change of heat content (left hand side of equation 6.1) for each region under study. It shows a considerable decrease of heat, centred at the equator, in the central and east regions, in the surface and subsurface boxes. This loss of heat is higher at the equator in the central part of the subsurface box. On the other hand, there is an increase of heat in most of the regions in the west and in all the bottom boxes.

This shows that there are processes that lead to a gain of heat content during a year. This is more evident in the equatorial region, east of the dateline. The extent to which processes such as advection and diffusion contribute to balance this heat content, within the model, is a key point in this thesis, and is discussed in the following sections.

6.2.2 Heat gain due to advection

Divergence of heat due to the mean flow, for a closed region of the ocean (a box in this analysis), implies that the flow out of the region is warmer than the inflow, and the region has gained extra heat energy from some other source. Heat convergence in a region means that the inflow leaves heat in the region, and exits at a lower temperature, which implies an extra cooling process.

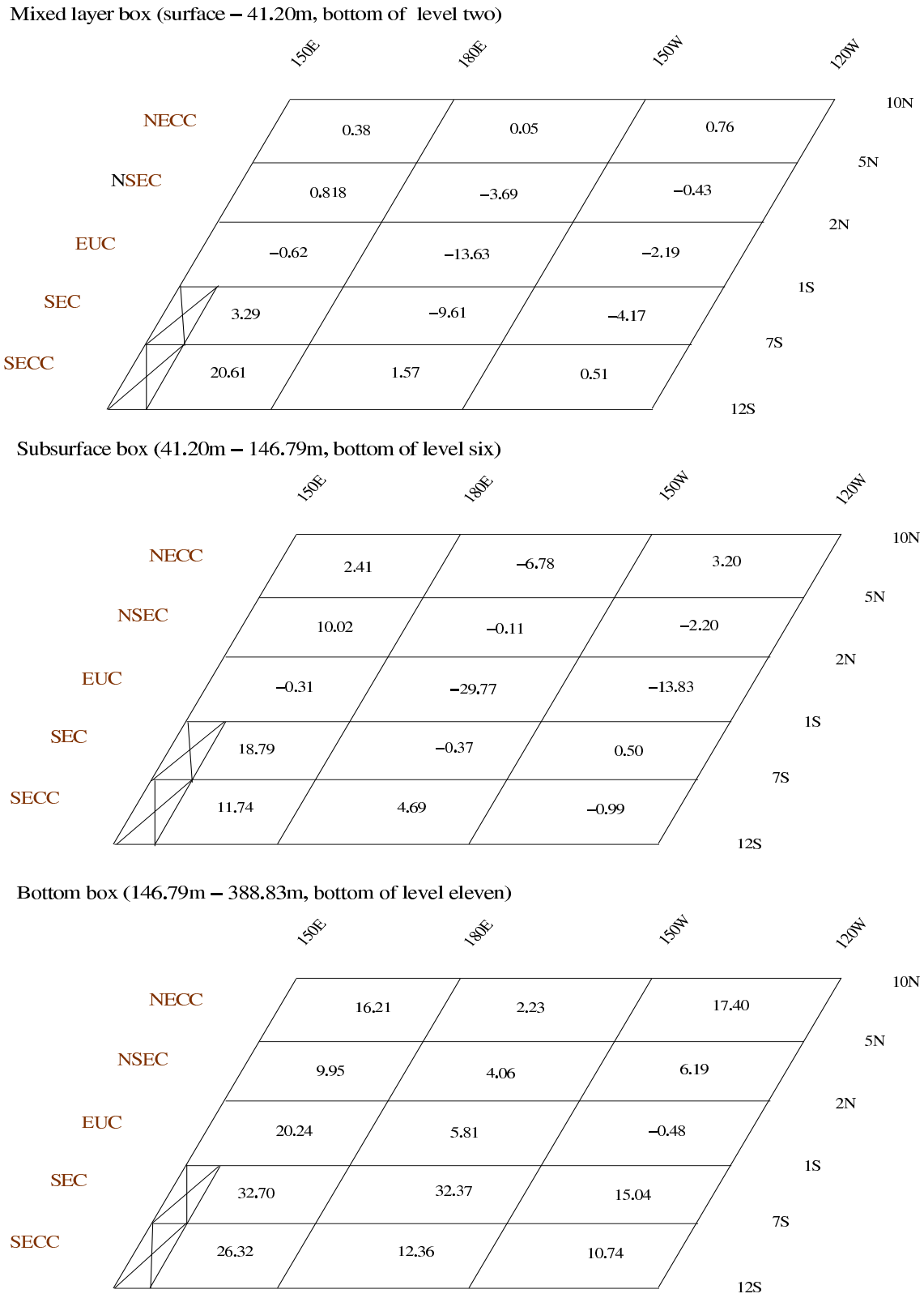

Figure 6.1: Rate of change of heat content for the regions under consideration. Units $10^{12}W$.

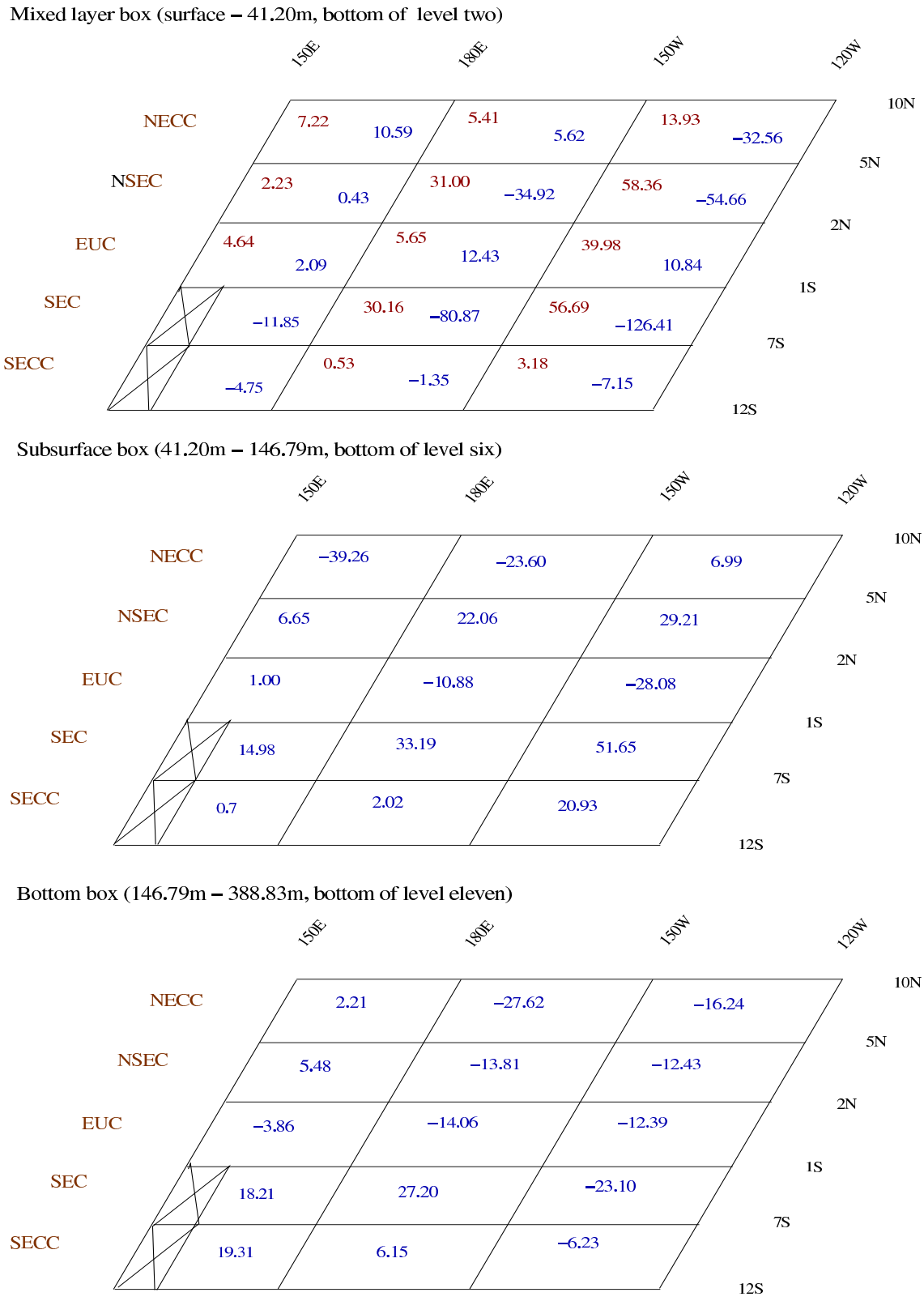

Figure 6.2: Heat gain by the full advective heat transport in 10^{12} watts (blue numbers) in the East, Centre and West for the meridional regions under study (see text). The red numbers in the mixed layer represent the surface gain of heat in Wm^{-2}.

Figure 6.2 shows the heat gain by the full advective heat transport for each region under study (first term of the right hand side of equation 6.1). At the surface, the current system gains heat from the atmosphere, which leads to an apparent divergence of the heat flux. This gain of heat is higher in both branches of the SEC. The convergence of heat at the equator suggests that the heat flux due to fluctuations is an important contribution to the heat flux in this region. This process will be discussed later on in this thesis.

The apparent divergence of heat at the surface is due to the energy input from the atmosphere, which warms the surface water. Dividing the total energy flux by the surface area yields an estimate of the heat input from the atmosphere per unit area. In the eastern regions this is: $56.69 Wm^{-2}$, $39.98 Wm^{-2}$ and $58.36 Wm^{-2}$ for the SEC, EUC and NSEC regions respectively. This is in reasonable agreement with the existing bulk formula estimates of air-sea exchange of $50-80 Wm^{-2}$ (Wyrtki, 1965; Weare et al., 1980).

Below the direct influence with the atmosphere, at the subsurface boxes, the EUC and the NECC are mainly characterized by divergence of heat. The rest of the current system at this level shows a convergence of heat, which decreases westward. Lower down in the deeper boxes, the EUC is also divergent. Elsewhere the deep levels are divergent in the east and convergent in the west.

6.2.3 Heat gain due to diffusion

Figure 6.3 shows the heat gain by diffusion in each region under consideration. It shows that all the regions in the mixed layer appear to be divergent. This arises because the surface heat flux is not considered in this calculation. The bottom boxes are characterized by convergence of heat due to diffusion, with maxima in the NECC regions. This corresponds to a heating of water by the diffusive flux at these levels. At intermediate levels, in the subsurface boxes, the heat flux is predominantly divergent. The heat advected into the region being lost by diffusion to deeper levels.

6.2.4 Heat balance

As stated in subsection 3.2.7 OCCAM conserves heat for every model timestep (every 15 minutes), by satisfying equation 3.32. If this is true in this analysis, the heat gain or loss by diffusive processes (figure 6.3) balances the heat gain or loss by advection (figure 6.2). In fact, this happens in few of the regions under consideration. From

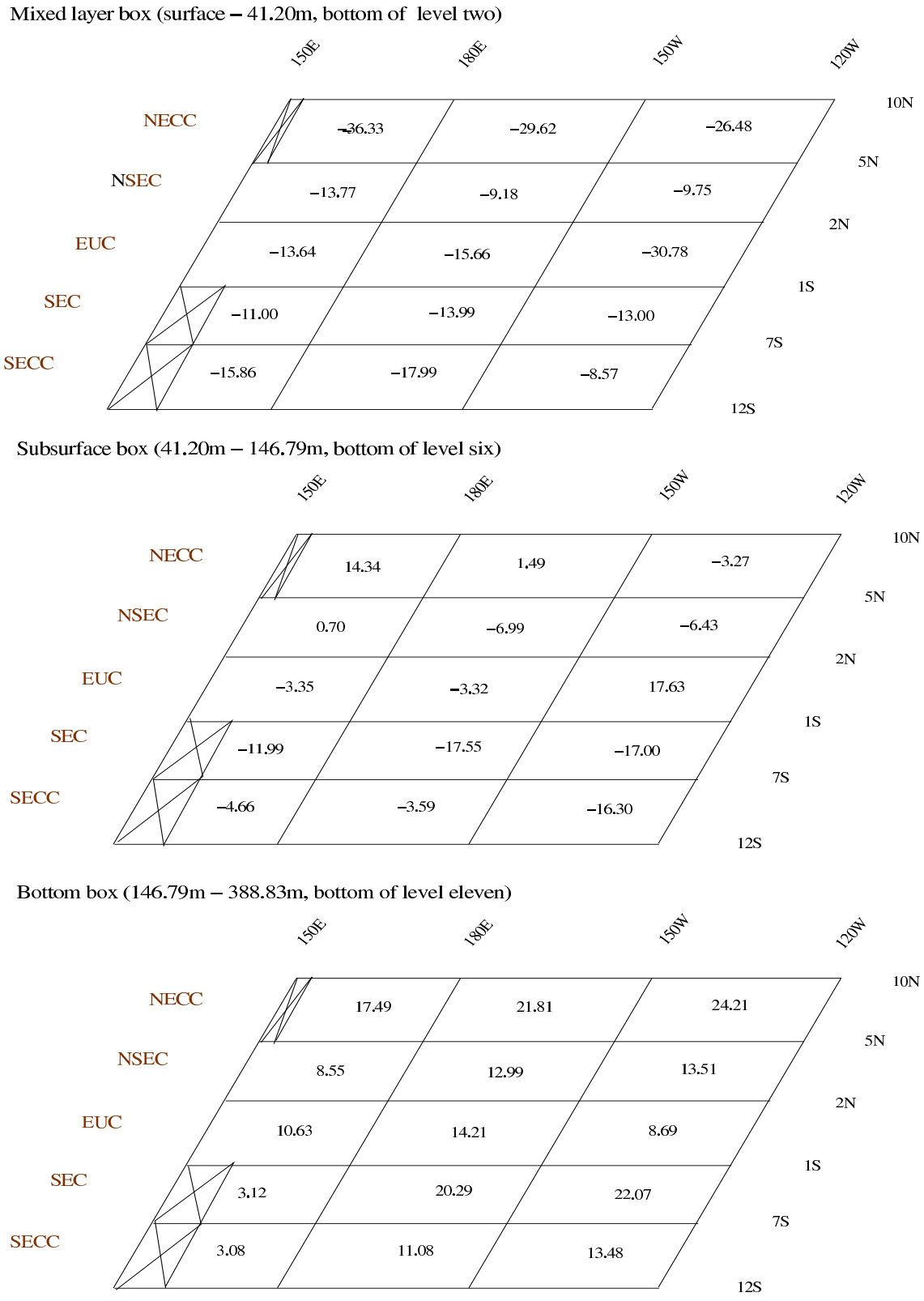

Figure 6.3: Heat gain by diffusion in the East, Centre and West for the meridional regions under study (see text). Units 10^{12} watts.

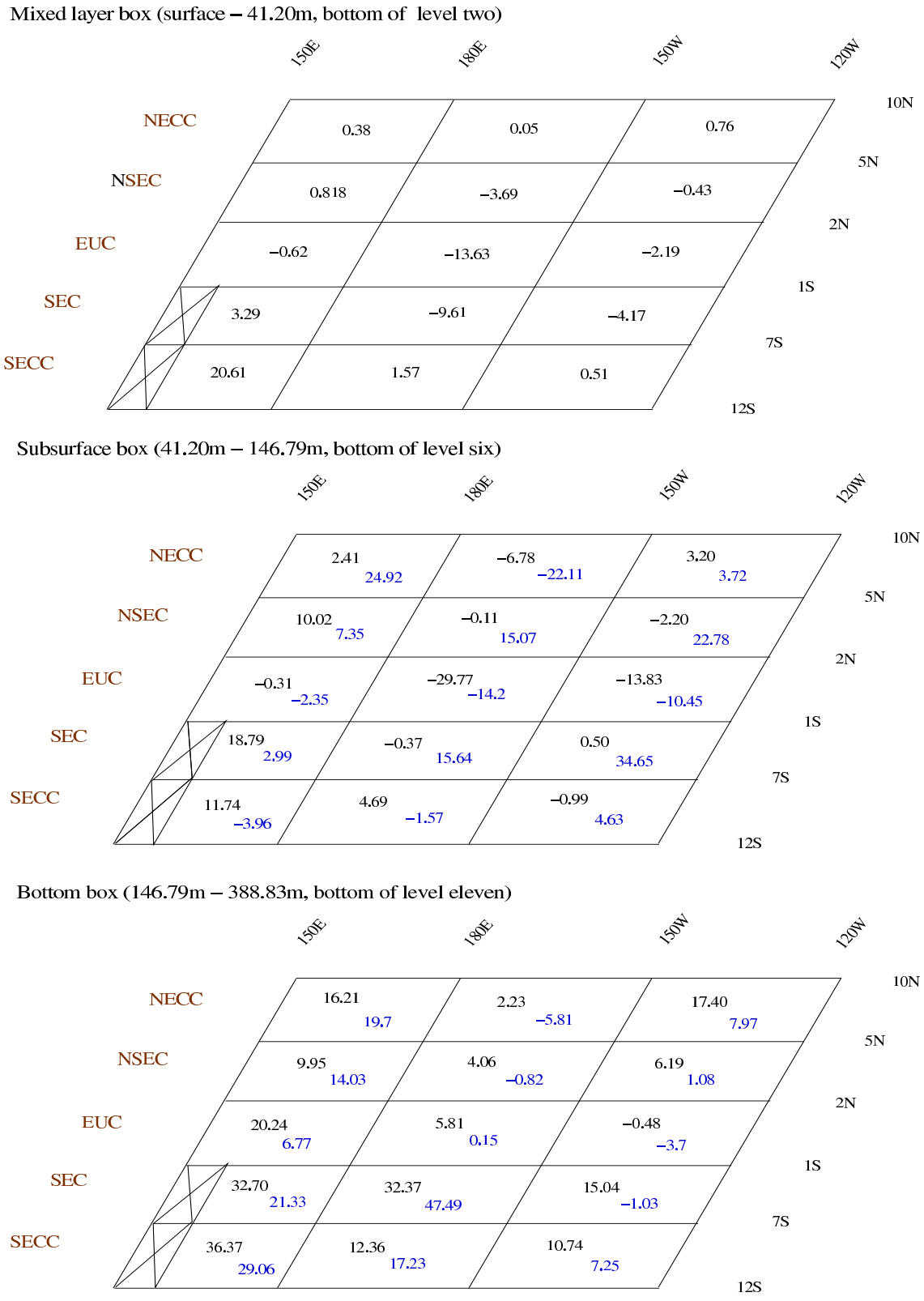

Figure 6.4: Rate of change of heat content (black numbers) and sum of heat flux due to advection and diffusion (blue numbers). Units $10^{12}W$.

both figures, it is observed that in the bottom boxes, the convergence of heat due to diffusion almost balances the divergence of heat due to advection. This is clearer in the east and centre regions.

Figure 6.4 shows the sum of such fluxes (blue numbers) and the rate of change of heat content (black numbers) for the subsurface and bottom boxes. The mixed layer box is not considered in this analysis, as this section deals mainly with processes below the direct influence with the atmosphere.

The figure shows that the sum of both terms is generally smaller than the rate of change of heat content, suggesting that there is not enough warming or cooling due to diffusion in some regions. Such discrepancy, as seen in last section, is explained by the estimate of the high frequency term.

6.2.5 Estimate of the high frequency term

Figure 6.5 shows the RMS of the estimate of the high frequency term (black) and the difference between the rate of change of heat content and the sum of the heat gain due to advection and diffusion (magenta). It shows that for most of the regions, in the subsurface and bottom boxes, the estimate of the error is of the same size as the actual analysis error. As mentioned in the last section, such a term is an important component of the heat balance in a closed region of the ocean, but it is a small contribution through each interface. Therefore, it is possible to study the individual components of the heat flux due to advection.

6.3 Components of the heat flow

The heat gain by the ocean from the atmosphere is redistributed by the current system. As mentioned in section 3.4, the heat flow due to advection can be split into the heat flux due to the mean flow and the fluctuations around it. Figure 6.6 shows the total heat flux due to the mean flow and the total heat flux due to fluctuations for each region under study, equation 3.58. (Note that here I consider the fluctuations with timescales of more than five days, not the shorter fluctuations considered earlier). The figure shows that both terms are of the same order of magnitude. At the equator, in all regions, there is a gain of heat due to the fluctuation term in the three vertical boxes, while away from it the fluctuations mainly contribute to cooling.

In the following sections I discuss the components of such heat fluxes.

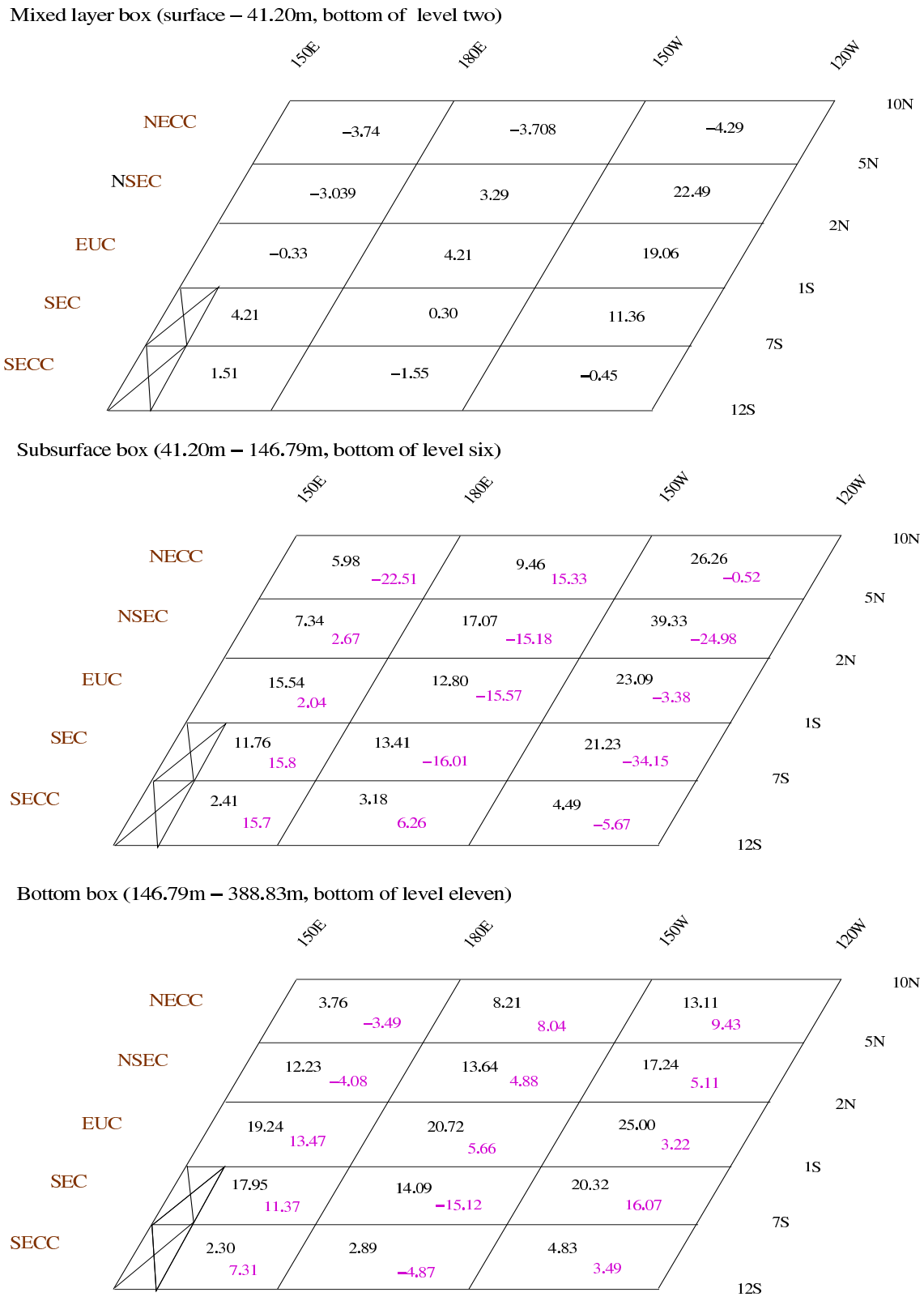

Figure 6.5: RMS of the estimate of the high frequency term for the regions under consideration (black numbers) and the difference between the rate of change of heat content and the sum of heat gain due to advection and diffusion (magenta numbers). Units $10^{12}W$.

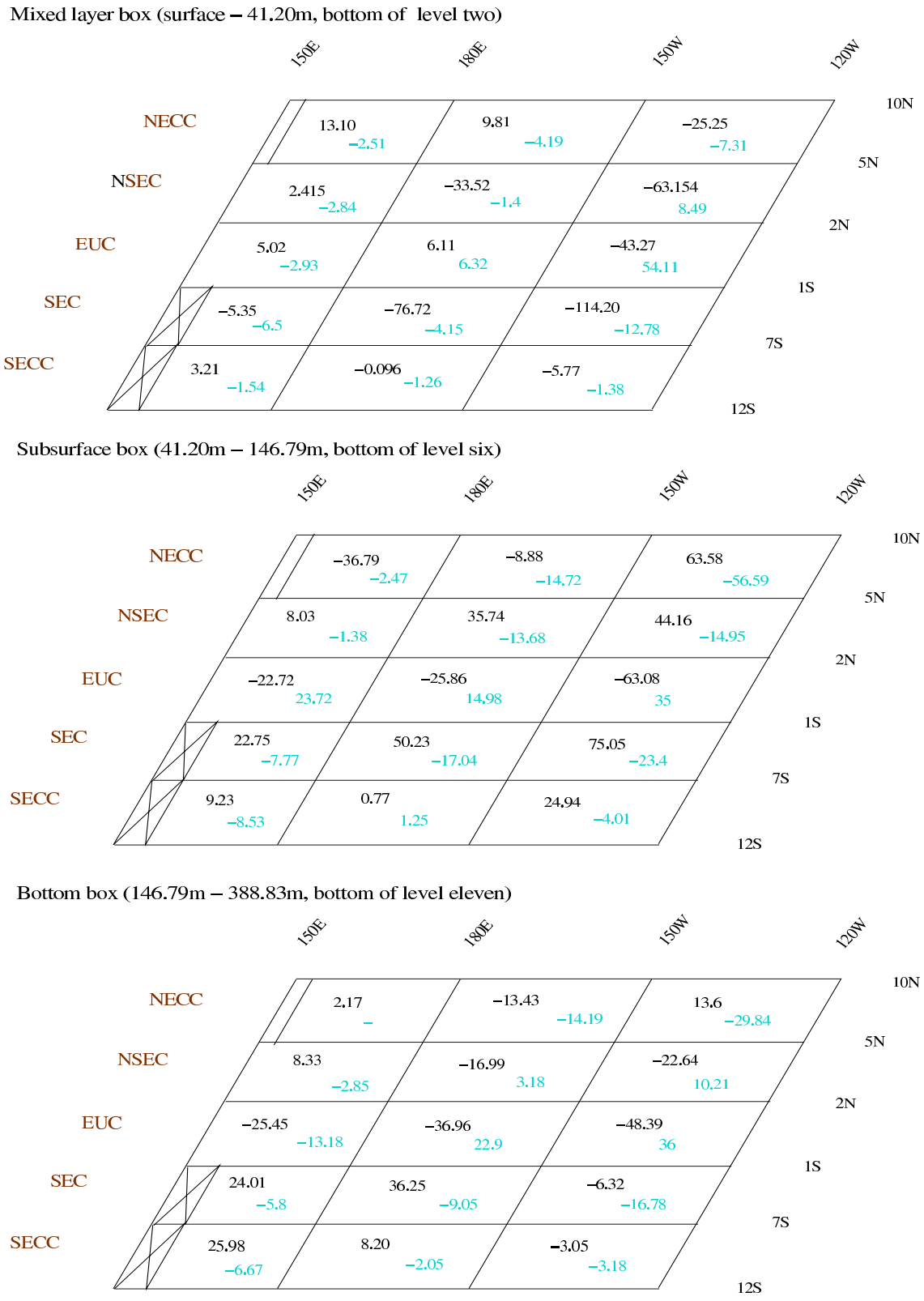

Figure 6.6: Heat gain by the mean flow (black numbers) and heat gain due to the fluctuations around the mean flow (blue numbers) for the regions under consideration (see text). Units $10^{12}W$.

6.3.1 Heat flux due to the mean flow

Figure 6.7 shows the total heat flux due to advection (blue numbers) and the heat flux due to the mean flow (black numbers) across each interface of the regions under consideration. Both terms are similar for most of the interfaces. However, in some areas they are considerably different, which means that the fluctuations around the mean are an important contribution to the heat due to advection.

It is important to notice that these fluxes are considerably bigger, compared with the heat gain by advection at each region. This makes it possible to study each individual flux, without having to allow for the contribution to the heat balance due to high frequency fluctuations of less than 5-days.

An important issue of this thesis is to understand which are the main processes, within the model, that produce changes in the heat flux due to advection. Although, figure 6.7 quantifies how much heat is lost or gained by the currents, it does not give information of which are the processes responsible for such changes. I then found convenient to study how the temperature of the main current system varies as the flow evolves.

6.3.2 Temperature analysis

To understand what is causing the gain of heat and the changes in the heat flux, I first study which parts of the current system experience significant change in temperature. To achieve this, I calculated the weighted temperature associated with the flux through each interface of the large analysis boxes. This is given by the equation:

$$\overline{T_l} = \frac{(\bar{u}\bar{T})_l}{(\bar{u}_A)_l} \tag{6.2}$$

where $(\bar{u}_A)_l$ is the volume transport in Sverdrups across the interface l. Figure (6.8) shows the volume transport across each interface of the regions under study and its corresponding weighted temperature.

In the eastern region of the Equatorial Undercurrent, the figure shows that at the subsurface box, the inflow is composed by: 9.60Sv across 150W and 20.4Sv due to meridional flow convergence, which are at around 22.38C; and by 5.23Sv across the bottom at 18.80C. Due to the eastward and upward motion of the EUC, the 5.23Sv leaves across 120W at 19.82C, demanding $23.23 \times 10^{12} W$ in order to raise its temperature; the rest of the outflow across 120W (6.64Sv) is provided by the meridional flow,

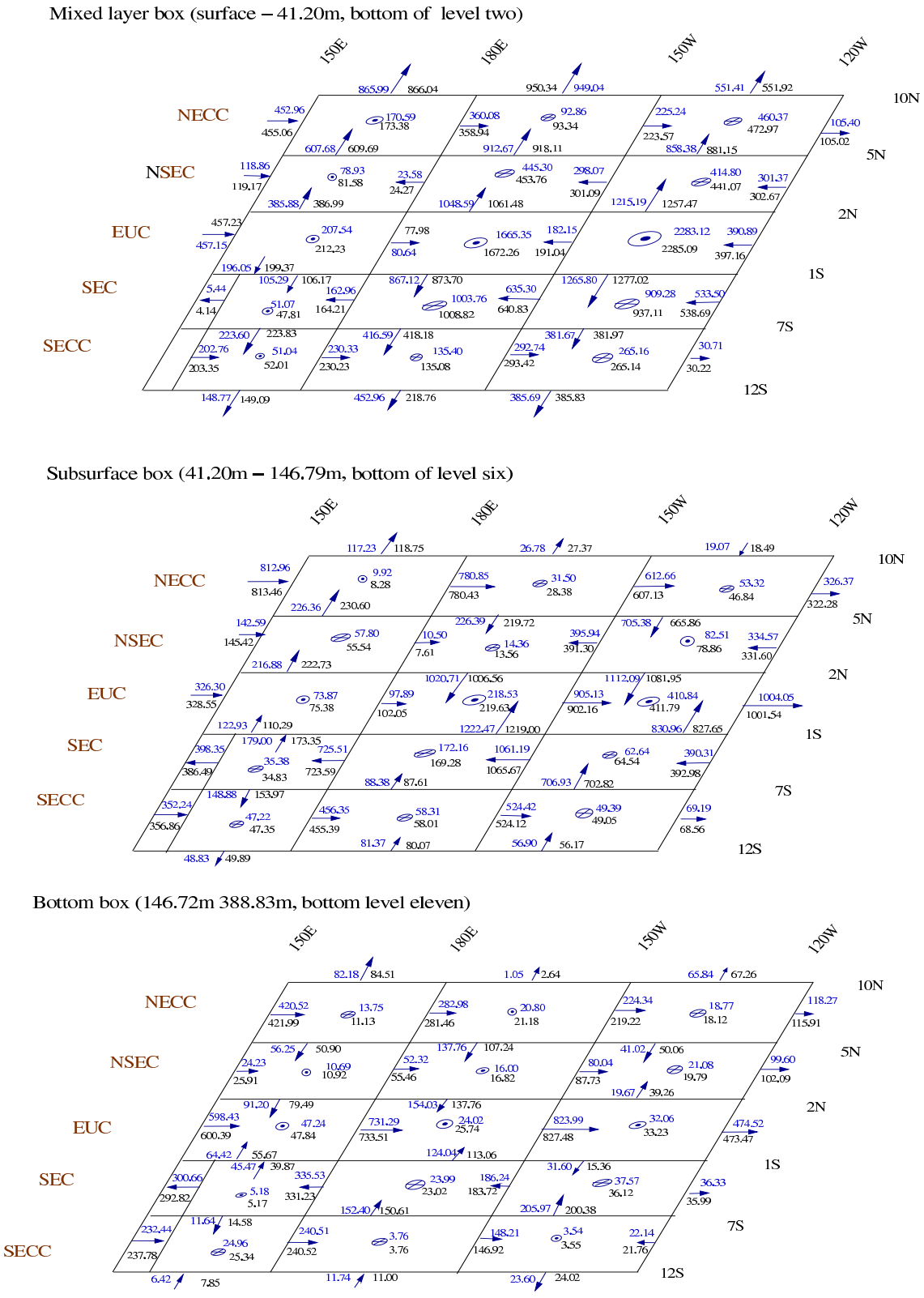

Figure 6.7: Components of the full advective heat transport (blue numbers) and of the mean flow (black numbers) for the regions under study. Units are 10^{12} watts.

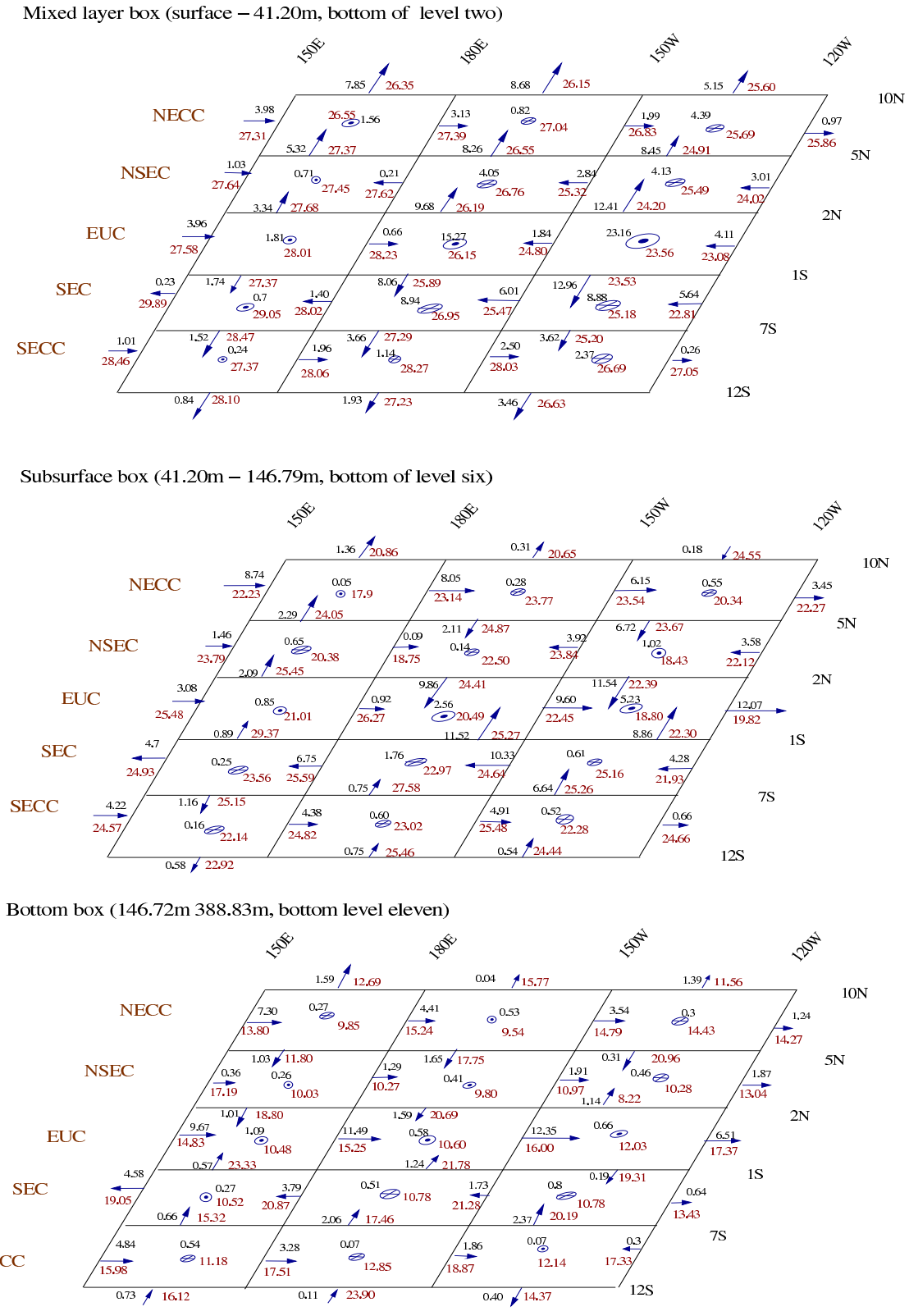

Figure 6.8: Volume transport (in Sv, black numbers) and its corresponding weight temperature (C, red numbers) at each interface for the regions under consideration (see text). The arrows represent the direction of the volume transport across the corresponding interface. The dot or cross in the middle of each box represents upwelling or downwelling, respectively, at the bottom of the box.

which reduces its temperature as it flows eastward, leaving $72.12 \times 10^{12} W$ in the system. The outward flow across the top comes from the 9.6Sv at 22.45C entering across 150W, which needs $44.58 \times 10^{12} W$ in order to leave at 23.56C, and from the rest of the meridional inflow, which demands $68.35 \times 10^{12} W$ to increase its temperature by 1.21C. The net heat gain in this box is of $63.08 \times 10^{12} W$, as shown in figure 6.2. Overall, most of the heat gain goes into heating the upwelling outflow. A similar situation holds in the central and western parts of the EUC region at this level.

In the bottom boxes, the heat gained by the EUC goes into increasing the temperature of the zonal and upward flow. In the central region, for example, the 12.35Sv of outward flow across 150W are formed by the meridional convergence, which reduces its temperature as it flows outward, leaving $61.15 \times 10^{12} W$; and by 8.93Sv of the flow across 180E, which increases its temperature by 0.75C, requiring $28.00 \times 10^{12} W$. On the other hand, $56.13 \times 10^{12} W$ are needed to warm the 2.46Sv of outflow at the top of the box and $13.10 \times 10^{12} W$ to heat the 0.58Sv from the bottom, which leave as eastward flow. The loss of heat of the meridional flow almost balances the gain of heat of the upward and eastward flow, having a net gain of heat of $36.96 \times 10^{12} W$, mainly due to the zonal gain of heat. A similar situation holds in the west part of the Equatorial Undercurrent at this level. In the east, the heat gain mainly goes into warming the flow across the top.

North and south of the Equatorial Undercurrent, in the subsurface box, there is downwelling from the mixed layer box, which generates convergence of heat. This implies that part of the inflow loses temperature as it leaves the region. The central and eastern regions are characterized by equatorward flow. In the central part of the northern branch of the South Equatorial Current (NSEC region), for example, the equatorward flow across 2N is formed by the 4.05Sv that downwell into the region at 26.76C, 3.92Sv across 150W at 23.84C and 1.97Sv of the 2.11Sv across 5N. The 3.92Sv needs $9.33 \times 10^{12} W$ to increase its temperature by 0.57C, meanwhile the downwelling flow leaves $39.80 \times 10^{12} W$ to reduce its temperature by 2.35C. The rest of the outflows reduce their temperature, leaving $5.14 \times 10^{12} W$ in the system. Overall, this region has a convergence of heat of $35.62 \times 10^{12} W$, where the main contribution is due to the cooling of the downward flow. The east region presents a similar behaviour.

In the SEC region the main contribution to the convergence of heat is also due to the cooling of the downward flow, which mainly flows equatorward. In this case, the westward flow across 150W, in the central part of the current, warms by $28.25 \times 10^{12} W$, as it contributes to the equatorward flow and continues its westward motion. This warming is partially compensated by the cooling due to the downwelling (around 4Sv)

and by the cooling of the flow from the south and east, as they flow downward for a total of $44.20 \times 10^{12} W$. The rest of the equatorward flow, which comes from the downwelling into the area loses $34.70 \times 10^{12} W$ to change its temperature by 1.68C. The net heat gain is then $-50.23 \times 10^{12} W$.

Away from the equator, in the North and South Equatorial Countercurrents (NECC and SECC) regions, the convergence of heat is also mainly due to the loss of temperature of the downwelled water, as it flows equatorward, and due to the cooling of the eastward flow. The convergence in the west and central regions of the NECC region is mainly due to the energy needed to warm the eastward flow.

The convergence of heat in the bottom boxes, south of the EUC region, is due to the loss of temperature of the downwelled volume flow, which flows equatorward. While the divergence in the north is due to the energy required to warm the zonal component of the flow that leaves equatorward.

This analysis quantifies how much heat is needed by the current system in order to leave colder or warmer from each region. But there is still the question of which are the processes that give or take energy from the system within the model. Such processes, below the direct influence of the atmosphere, can be due to the fluctuations around the mean flow, diffusion and the high frequency term.

6.3.3 Fluctuations in the mean flow

Figure 6.9 shows the contribution to the heat flux by the fluctuation term for each box interface. The figure shows important contributions equatorward across 1S, 2N and 5S, for the central and eastern region. On the other hand, figure 6.6 shows a gain of heat due to fluctuations at the EUC region and at the bottom boxes of the NSEC region. Figure 6.9 shows that such gain of heat comes mainly from the northern faces of the regions.

For example, the $35 \times 10^{12} W$ of heat gain at the east part of the EUC region, in the subsurface box is mainly due to the $30 \times 10^{12} W$ across the northern interface. North and south of the EUC the meridional fluxes in the subsurface box seem to balance, leading to a small total loss of heat across the top interface.

This term is of the same order of magnitude as the diffusion term, and therefore an important component of the heat balance.

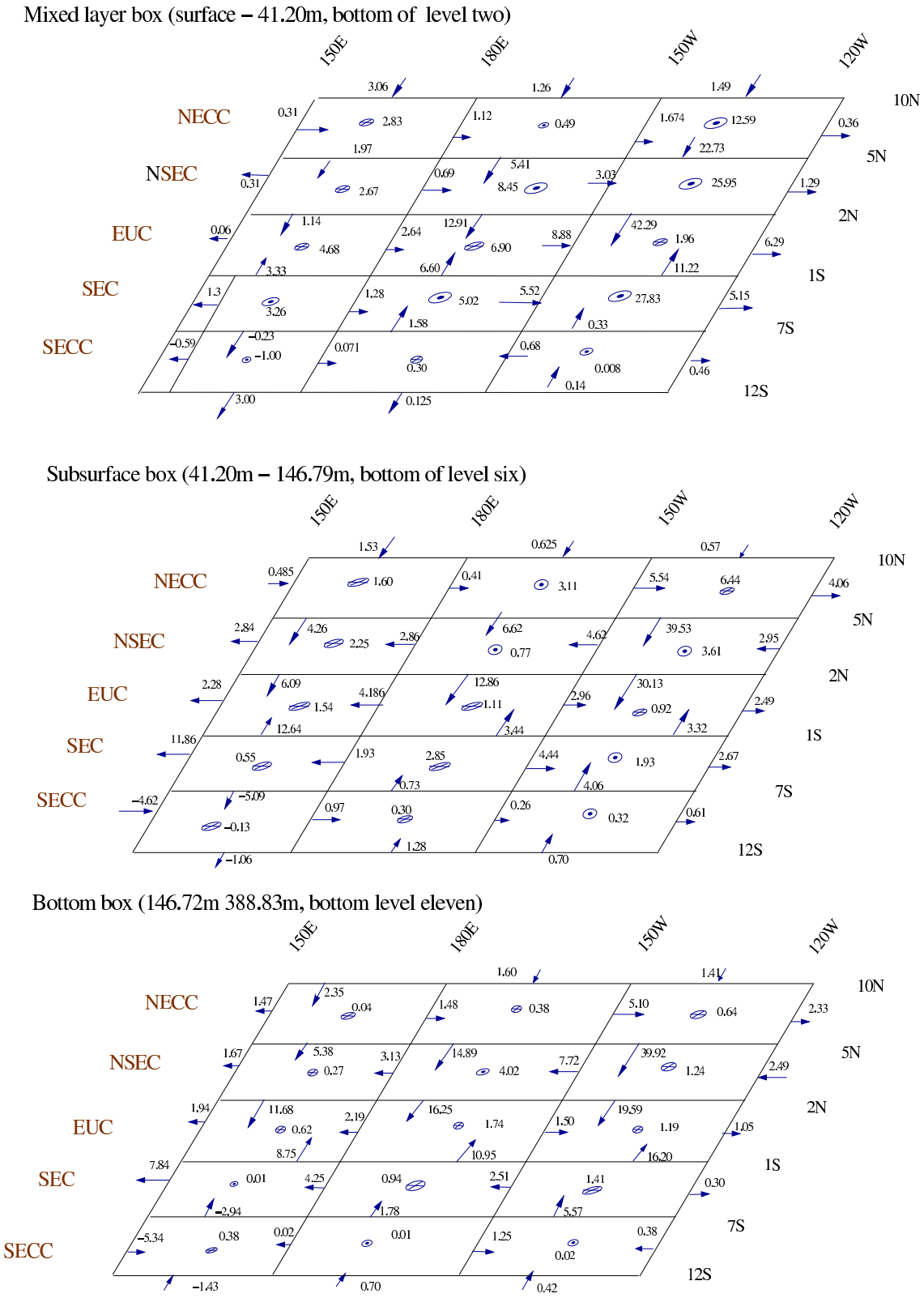

Figure 6.9: Heat flux due to fluctuations across each interface of the regions under consideration (see text). Units $10^{12}W$.

6.4 Heat flow due to diffusion

Figure 6.10 shows the heat flux due to diffusion at each interface of the regions under consideration. The light blue arrows, without a value, represent the direction of the diffusive heat flow of less than $0.1 \times 10^{12} W$. It shows that the vertical component is the dominant term in diffusive processes. However, there are small meridional contributions, mainly across 2N and 5N that are important for the total heat balance analysis.

It is important to notice that, in most of the regions, the heat flux due to diffusion increases from the bottom of level two to the bottom of level six. As a consequence, the heat gain by the region due to diffusive processes is negative (figure 6.3).

6.5 Heat balance between advection and diffusion

In section 6.3.2 I discussed how much heat is gained by the mean equatorial current system. Here, I study how much of this heat can be explained by diffusive and fluctuating processes and also due to the high frequency term.

For the region located in the east, in the subsurface box, the heat gain due to advection by the EUC is $-28.08 \times 10^{12} W$ (figure 6.2), which is formed by $-63.12 \times 10^{12} W$ demanded by the mean flow in order to leave warmer across the top and east interfaces (as seen in section 6.3.1); and by $35 \times 10^{12} W$ due to the heat gain by the fluctuations around the mean (figure 6.6). The latter heat flux is mainly an inflow from the northern interface (figure 6.9). The heat due to diffusion into the region is composed of: $31.05 \times 10^{12} W$ across the top and from an outflow of $14.41 \times 10^{12} W$ across the bottom. The diffusion across the top brings some of the heat needed by the upwelling to increase its temperature. Nevertheless, it requires $44.58 \times 10^{12} W$ to leave warmer. The heat flux due to fluctuations across the northern face seems to bring the rest of the necessary heat.

The rate of change of heat content is of $-13.83 \times 10^{12} W$, while the sum of heat fluxes is of $-10.45 \times 10^{12} W$ (figure 6.4). As discussed earlier, the extra heat is due to the high frequency term.

The east part of the NSEC region presents convergence of heat due to advection of $29.21 \times 10^{12} W$. This gain of heat is formed by $44.16 \times 10^{12} W$ due to the mean flow and $-14.95 \times 10^{12} W$ due to fluctuations around the mean. There is $-4.67 \times 10^{12} W$ of heat divergence in the region due to diffusive processes. The mean flow in this region mainly

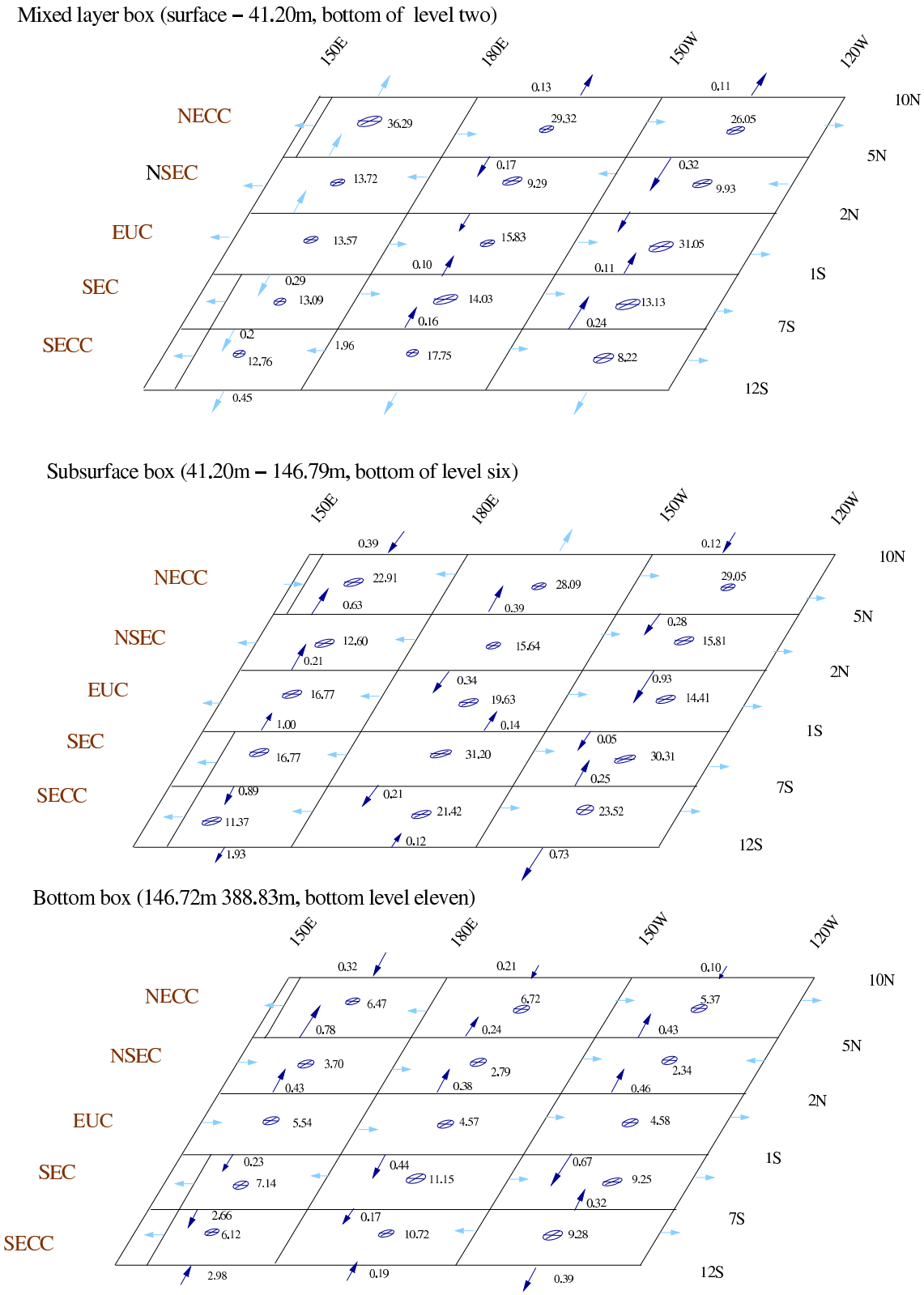

Figure 6.10: Heat flux due to diffusion across each interface for the regions under consideration (see text). The arrows represent the direction of the diffusive heat flux across the corresponding interface. The dot or cross in the middle of each box represents upwelling or downwelling, respectively, at the bottom of the box. Units $10^{12}W$.

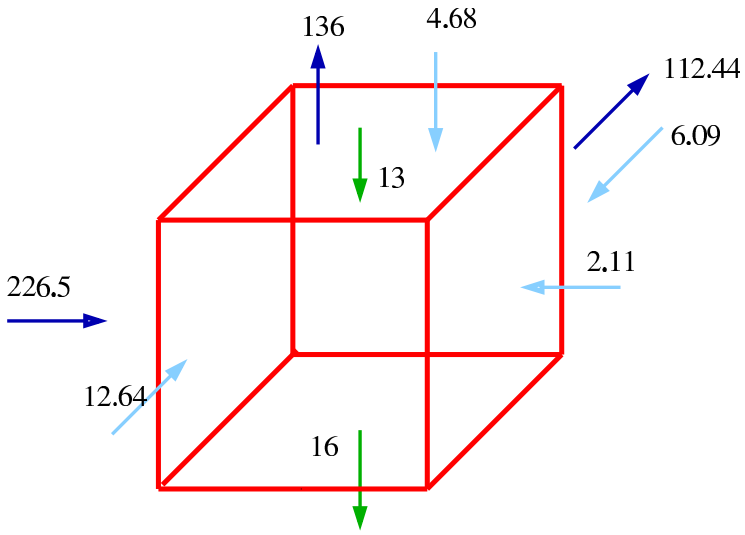

Figure 6.11: Figure showing the main components of heat flux into the region embedded in the Warm Pool (150E - 180E, 1S - 2N, 41.20m - 146.79m). Dark blue arrows correspond to the heat flux due to the mean flow, light blue arrows to the heat flux due to fluctuations around the mean and green arrows to heat flux due to diffusion. Units $10^{12}W$.

loses heat across the southern interface (toward the equator), which is mainly due to fluctuation processes, and across the bottom, which are due to diffusive processes.

The central part of the EUC demands $26.16 \times 10^{12}W$, of which $24.28 \times 10^{12}W$ is due to diffusive processes. In the west there is mainly outward diffusion, and just $13.57 \times 10^{12}W$ of the $22.72 \times 10^{12}W$ needed by the mean flow is due to diffusivity. At the bottom box the situation is similar, where just around half of the heat gained by the mean flow is due to diffusion, and the rest must come from other processes.

6.6 Summary and conclusions

Figure 6.11 is a summary of the main components of the heat flux for the box embedded in the warm pool (subsurface box in the west of the EUC region). It shows that the zonal heat inflow due to the mean flow is almost balanced by the meridional and vertical mean heat flow, leaving around $23 \times 10^{12}W$ in the region, which is balanced by the heat flux convergence due to the fluctuations around the mean, which sum to about $24 \times 10^{12}W$.

Godfrey and Lindstrom (1989) used CTD and Dopper profile data to estimate the turbulent heat flux through the western equatorial Pacific. They concluded that the ocean circulation in this region is too slow, and the temperature gradient too weak for either advection or mixing to carry any heat away from the region. This analysis shows

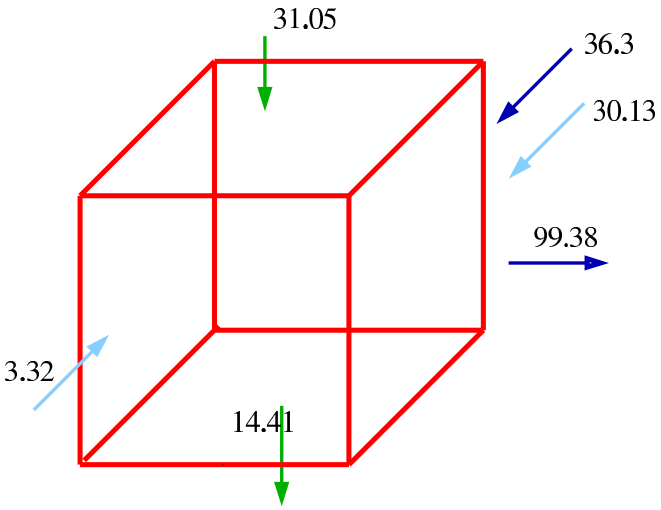

Figure 6.12: Figure showing the main components of heat flux into the region below the Cold Tongue (150W - 120W, 1S - 2N, 41.20m - 146.79m). Dark blue arrows correspond to the heat flux due to the mean flow, light blue arrows to the heat flux due to fluctuations around the mean and green arrows to heat flux due to diffusion. Units $10^{12}W$.

that although heat transport of the current system in the west is weak, there exists a heat transport divergence by the mean flow which is balanced by the fluctuations around the mean, leading to an almost zero net heating.

The vertical diffusion found by Godfrey and Lindstrom (1989) is about $10-16Wm^{-2}$ in the top 100m; figure 6.11 shows that in OCCAM at the top of the region (41m) the vertical diffusion is around $13Wm^{-2}$ and at the bottom (146.79m) is around $16Wm^{-2}$. If, as Godfrey and Lindstrom (1989) suggest, the net surface heat flux entering the region is near zero, the heat flow due to diffusion must transport downward the gain of heat at the surface, as the heat flux due to the mean flow and due to fluctuations around the mean almost balance in this analysis. The surface heat flux in this region (figure 6.2) is $4.64Wm^{-2}$. Therefore, the vertical diffusion transports the surface heat downward and the rest of the heat balance is associated with the high frequency term.

Figure 6.12 shows a summary of the main components of heat flux in the Cold Tongue region below the mixed layer. It shows that this region is characterized by zonal divergence in heat transport that is balanced by a strong inflow of heat due to the mean meridional flow, due to the meridional fluctuations around the mean flow and due to vertical diffusion. The latter fluxes almost balance the zonal component of the mean heat flux. There is a further outflow of heat at the bottom of the box due to diffusion.

The fluctuations around the mean are associated with the Tropical Instability Waves

that bring heat toward the equator. The latter has been studied by several authors. Swenson and Hansen (1999), for example, used satellite-tracked drifting buoys and VOS/XBT profiles to evaluate how the seasonal cycle of major oceanic processes redistribute heat in the Cold Tongue. They calculated the eddy heat flux as a residual, which provides convergence of heat into the core of the cold tongue. In their analysis, located in the mixed layer the mean meridional heat flux contributes to a divergence of heat. Wang and McPhaden (1999) used TAO buoy array to examine the surface-layer heat balance in the equatorial Pacific. They found that the meridional advection in the Cold Tongue warms the mixed layer; in their analysis, the meridional heat advection explicitly includes the contribution from the Tropical Instability Waves.

This analysis shows that in the mixed layer there is meridional divergence of heat due to the mean flow and convergence due to the fluctuations around the mean (TIWs). Below the mixed layer, the mean heat flow brings heat to the Cold Tongue, in the same direction as the fluctuations around the mean.

In the same analysis, Wang and McPhaden (1999) inferred the vertical heat fluxes out of the base of the mixed layer in the Cold Tongue region, which are comparable in magnitude to the surface fluxes in the east and central Pacific. This analysis shows that the heat flux out the mixed layer box is mainly due to vertical diffusion, around $31 W m^{-2}$, which is similar to the surface heat flux of $39 W m^{-2}$ calculated for this region (figure 6.2). This meridional heat convergence toward the equator and the vertical diffusion of heat are mainly increasing the temperature of the Equatorial Undercurrent as it flows eastward and upward.

Whereas diffusive processes explain part of the heat gain by the mean flow, the fluctuations about the mean are identified as an important process in the heat balance. In the context of this analysis the high frequency term also makes a large contribution to the heat balance.

Chapter 7

Variations in time

7.1 Introduction

The solar energy absorbed in the ocean is deposited in the upper levels of the sea and mixed downward by wind waves, convective overturning and turbulent processes. The vertical profile of temperature follows three main regimes: the near-surface mixed layer, where the gradients of temperature are small; the seasonal thermocline where the temperature changes relatively rapidly below the base of the mixed layer; and the deep permanent thermocline, where the temperature changes are more gradual with depth and vary slowly with time.

Turbulent or mixing processes affect not just the sea surface temperature but also the intensity of the equatorial currents. Crawford and Osborn (1981) stated that the energetics of the Equatorial Undercurrent is to some extent a balance between the work done by the zonal pressure gradient and turbulent dissipation. Small scale turbulence has a significant effect on the large-scale oceanic circulation.

The region below the core of the Equatorial Undercurrent is characterised by large vertical shear and small vertical gradients of temperature. Measurements of the vertical temperature gradients and horizontal velocity components reveal that turbulent dissipation is far higher near the equator than in extra equatorial latitudes, and is high even below the core of the Equatorial Undercurrent (Gregg, 1980; Gregg and Sanford, 1980; Gargett and Osborn, 1981). Vertical mixing is an important contribution to the heat balance in the equatorial region. A good parametrisation of it in ocean models is crucial for realistic heat budget analysis.

The vertical diffusion discussed so far is focused in its mean through the year under study. In this chapter I study, within the model, how it varies in time close to

the equator and in the instability region, where the Tropical Instability Waves occur. To achieve this I select three latitudes (1S, 1N and 4N) and make use of Hovmoller diagrams (longitude - time diagrams) at the east Pacific (120W - 150W), during the period of study for the first levels of the model.

7.2 Vertical diffusion analysis

7.2.1 Mixed layer variability

To study how the mixed layer varies within OCCAM, I analysed the gradient of temperature at the bottom of the first levels of the model, given by:

$$\frac{\Delta T_{i,j,k+\frac{1}{2}}}{\Delta z_{k+\frac{1}{2}}} = \frac{T_{i,j,k+1} - T_{i,j,k}}{z_{k+1} - z_k} \tag{7.1}$$

where z_k is defined at the centre of a model grid box at level k and $T_{i,j,k}$ is the temperature of the model grid box ijk. In the mixed layer, where mixing processes occur $T_{i,j,k} \approx T_{i,j,k+1}$. When the difference between $T_{i,j,k}\, and\, T_{i,j,k+1}$ is large the ocean is well stratified.

Figures 7.1, 7.2 and 7.3 show the Hovmoller diagrams of the gradient of temperature at 1S, 1N and 4N, respectively, at the bottom of the first six levels of the model (20.00m, 41.20m, 63.95m, 88.72m, 116.09 and 146.79m). Figures 7.1 and 7.2 show that the mixed layer is deeper at 1S, where it extends down to the bottom of level four, while at 1N, it extends down to the bottom of level three. The latter latitude shows a westward propagation of high values of the gradient of temperature at the bottom of level two during the first half of the year and during autumn from 120W - 150W. At both latitudes the mixed layer shallows to 20m from 120W to 130W during summer and from 150W to 130W during autumn. The rest of the time it extends down to 63.95m (bottom of level three). At deeper levels the ocean is weakly stratified mainly during the first half of the year.

At 4N (figure 7.3) the mixed layer also shows a vertical variability that propagates westward, which varies from 63.95m to 116.09m (levels three to five), during the first half of the year. This variability is characterised by a period of three months, a wavelength of around 1000km and an amplitude of 52m. Below level two there is also strong stratification during summer at this latitude. The rest of the year the mixed layer shows a vertical variability that propagates westward mainly at the bottom of levels three and four.

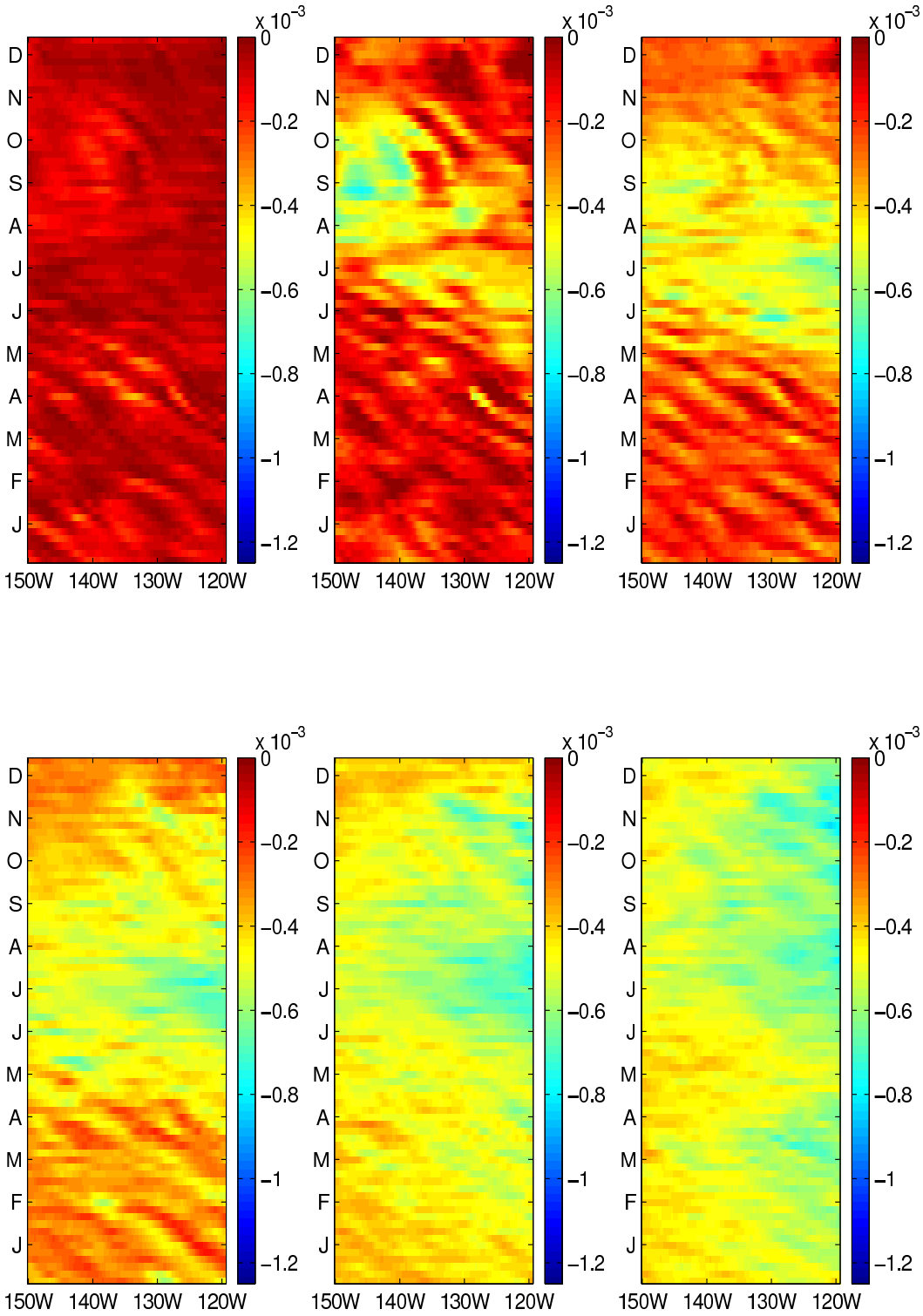

Figure 7.1: Gradient of temperature at 1S at the bottom of the first six levels of the model (20.00m, 41.20m, 63.95m, 88.72m, 116.09 and 146.79m, from top left to bottom right). Units $C\,cm^{-1}$.

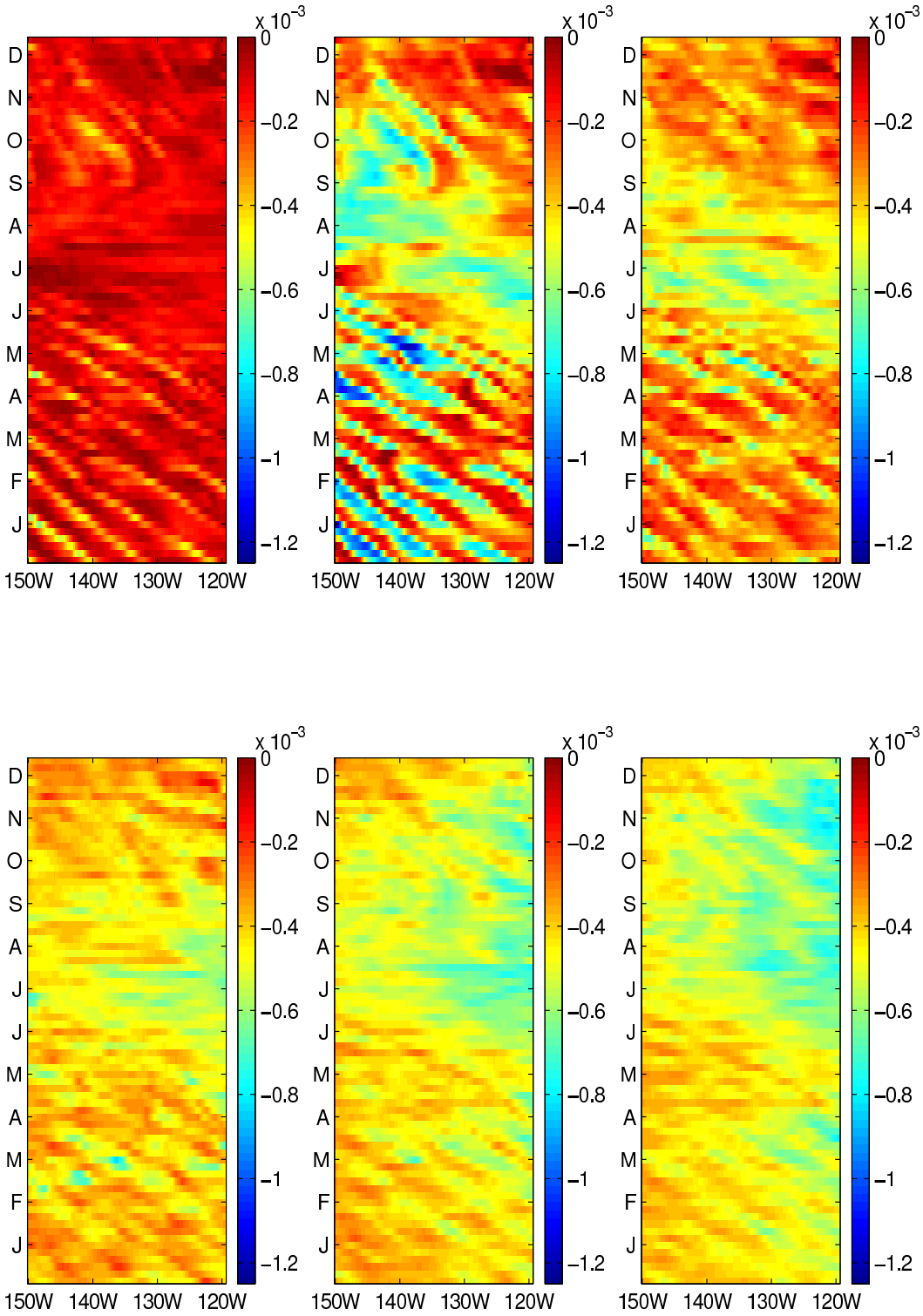

Figure 7.2: Gradient of temperature at 1N at the bottom of the first six levels of the model (20.00m, 41.20m, 63.95m, 88.72m, 116.09 and 146.79m, from top left to bottom right). Units $C\,cm^{-1}$.

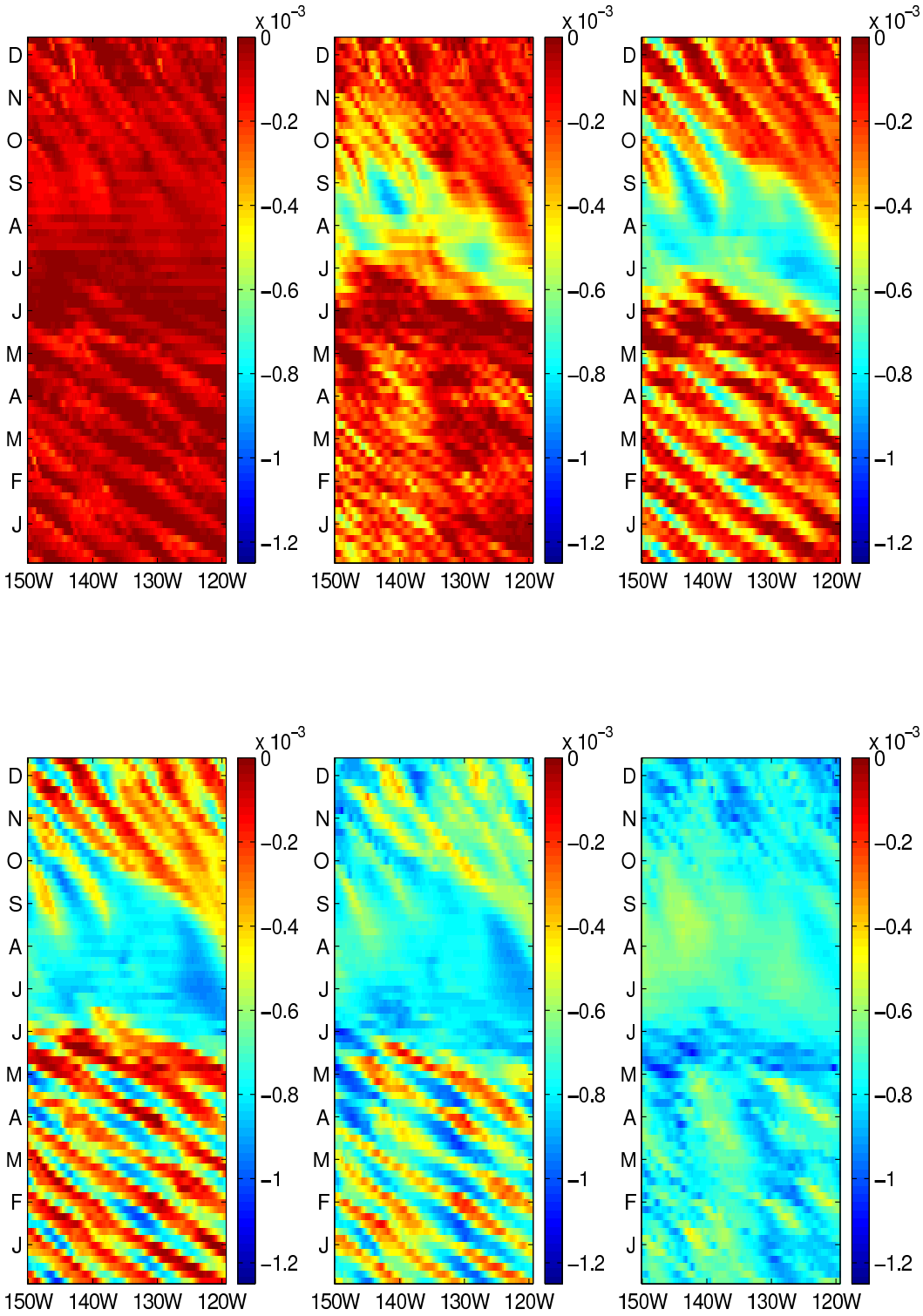

Figure 7.3: Gradient of temperature at 4N at the bottom of the first six levels of the model (20.00m, 41.20m, 63.95m, 88.72m, 116.09 and 146.79m, from top left to bottom right). Units $C\,cm^{-1}$.

In general, close to the equator, the ocean is constantly stratified during summer and part of autumn. For the rest of the year it shows a westward propagation of mixing mainly at 1N and 4N.

7.2.2 Vertical diffusion

The vertical diffusion depends on the gradient of temperature and on the coefficient of vertical diffusivity:

$$D_v = A_z \frac{\partial T}{\partial z} \tag{7.2}$$

Figures 7.4, 7.5 and 7.6 show the Hovmoller diagrams of the vertical diffusion at 1S, 1N and 4N, for the levels discussed earlier.

The figures show high diffusion at the three latitudes at the bottom of level one. At 1S and 4N the diffusion mainly follows the gradient of temperature (discussed in the last section), apart from some patchy events at the bottom of levels two and three. On the other hand, at 1N there is strong diffusion at the bottom of level two and during the first half of the year at level three, which does not come from the gradient of temperature. At deeper levels (four to six) the diffusion follows the gradient of temperature at the three latitudes under consideration.

7.2.3 Vertical mixing coefficient

In the cases when the vertical diffusion is high and does not vary with the gradient of temperature, the coefficient of vertical diffusivity is the main contributor. As mentioned in section 3.2.6, the model diffusivity is based on the Pacanowski and Philander (1981) scheme, where the coefficient of vertical diffusivity is given by (equation 3.29):

$$A_z = \frac{50}{(1 + 5R_i)^3} + 0.5 \tag{7.3}$$

Figures 7.7, 7.8 and 7.9 show the Hovmoller diagrams of the coefficient of vertical diffusivity at 1S, 1N and 4N, respectively, at the bottom of the first three levels of the model. The figures show high values of the coefficient of vertical diffusivity at the bottom of level one at all three latitudes.

At the bottom of level two, at the three latitudes, there is a westward propagation of the high values of the vertical coefficient of diffusivity, during the first half of the

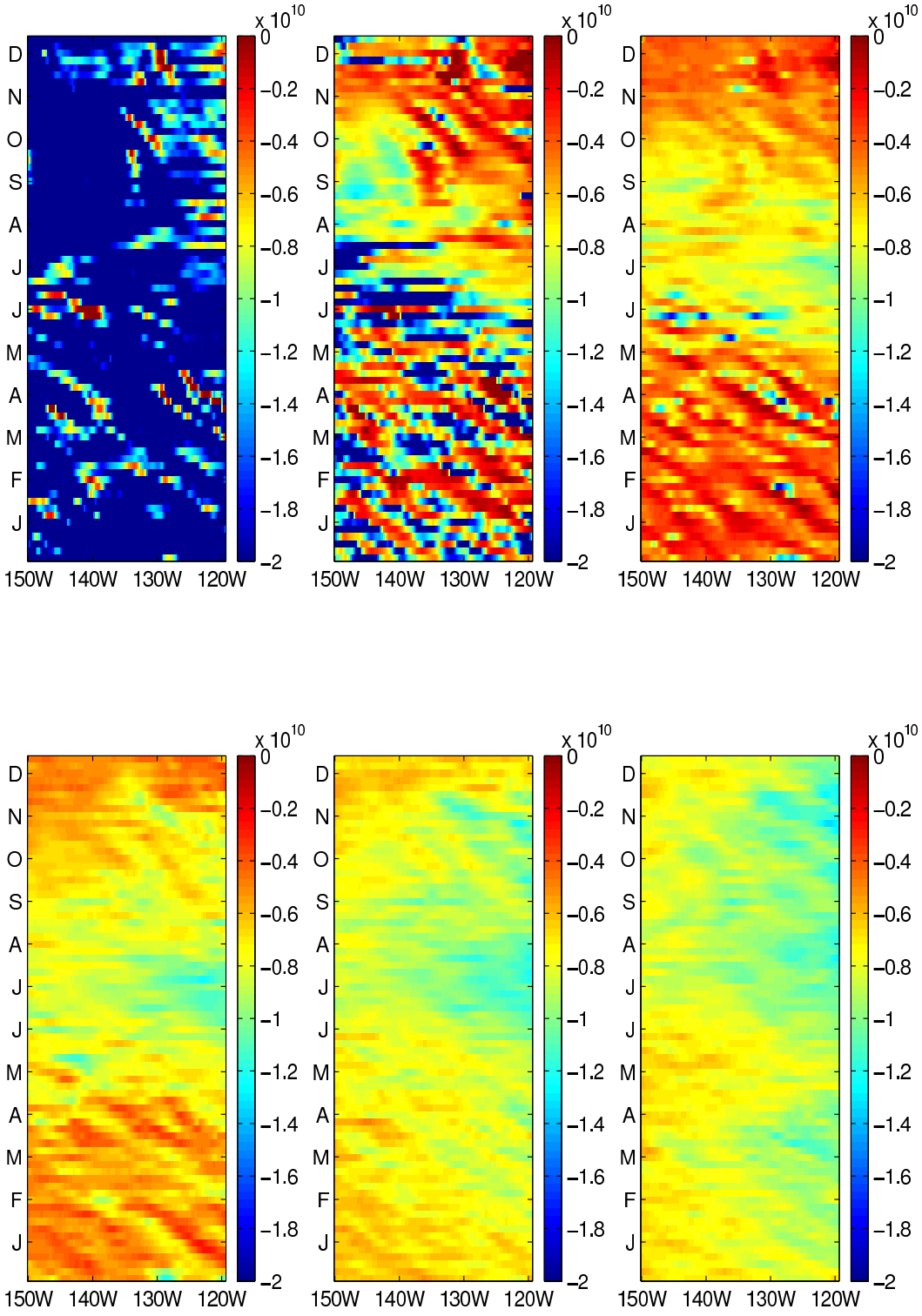

Figure 7.4: Vertical diffusion at 1S across the bottom of the first six levels of the model (20.00m, 41.20m, 63.95m, 88.72m, 116.09 and 146.79m, from top left to bottom right). Units W.

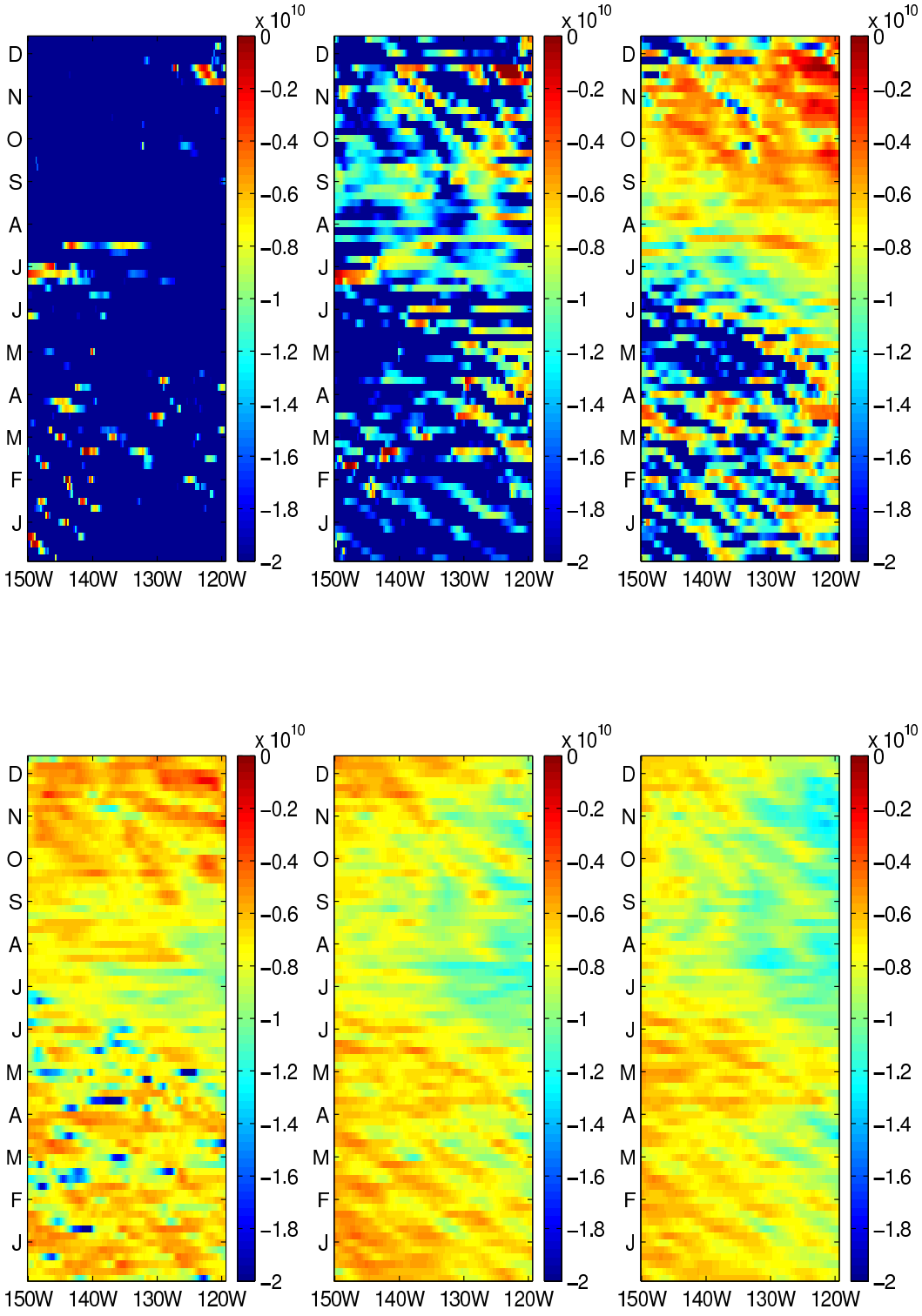

Figure 7.5: Vertical diffusion at 1N across the bottom of the first six levels of the model (20.00m, 41.20m, 63.95m, 88.72m, 116.09 and 146.79m, from top left to bottom right). Units W.

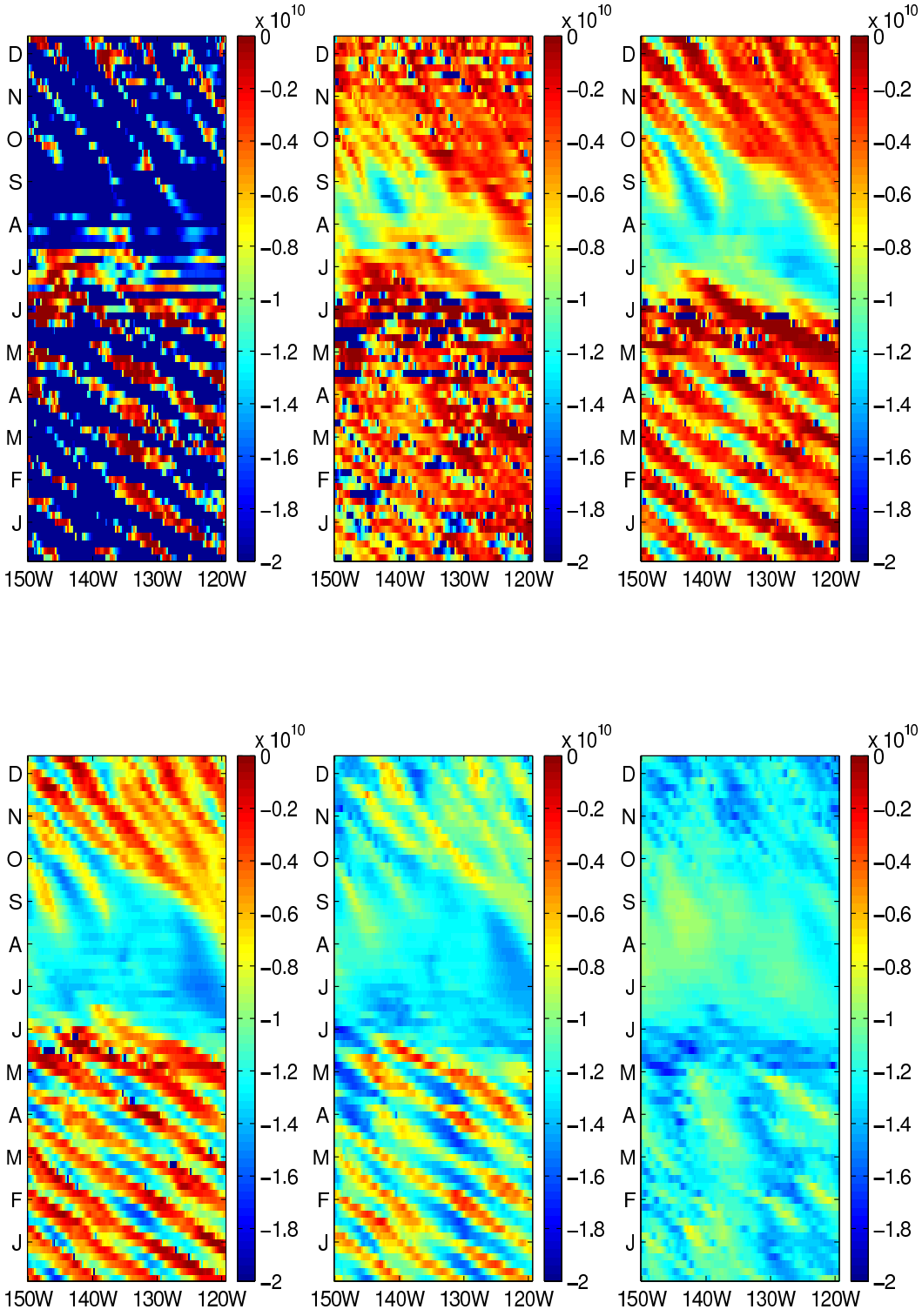

Figure 7.6: Vertical diffusion at 4N across the bottom of the first six levels of the model (20.00m, 41.20m, 63.95m, 88.72m, 116.09 and 146.79m, from top left to bottom right). Units W.

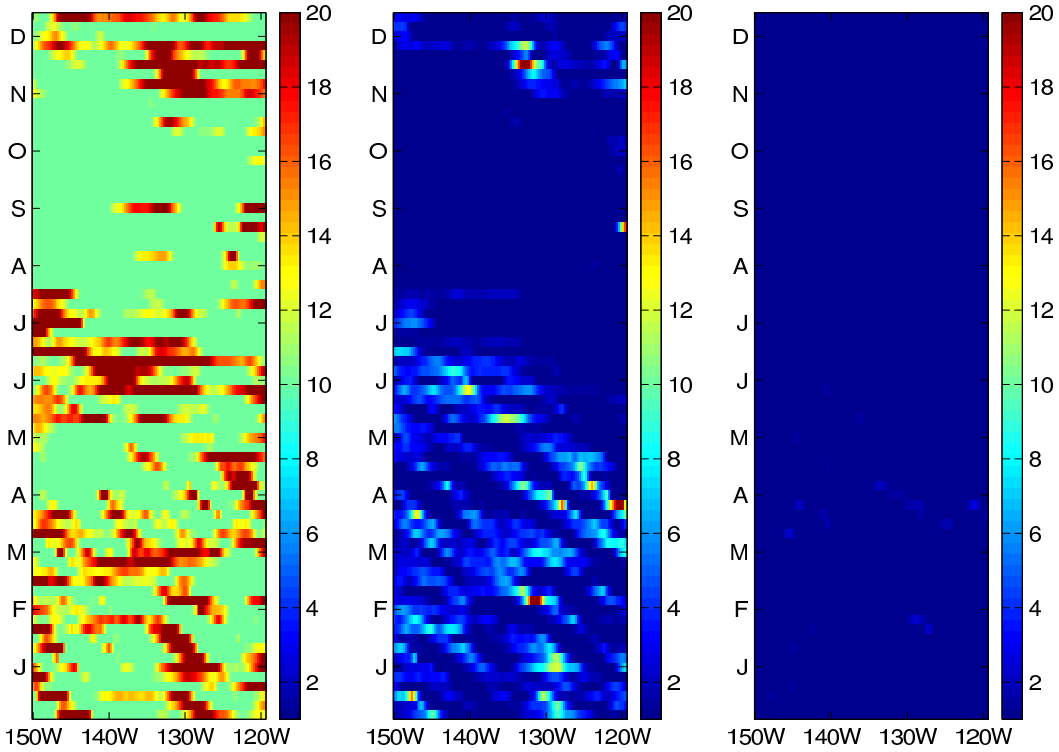

Figure 7.7: Coefficient of vertical diffusivity at 1S across the bottom of the first three levels of the model (20.00m, 41.20m and 63.95m). Units $cm^{-2}s^{-1}$.

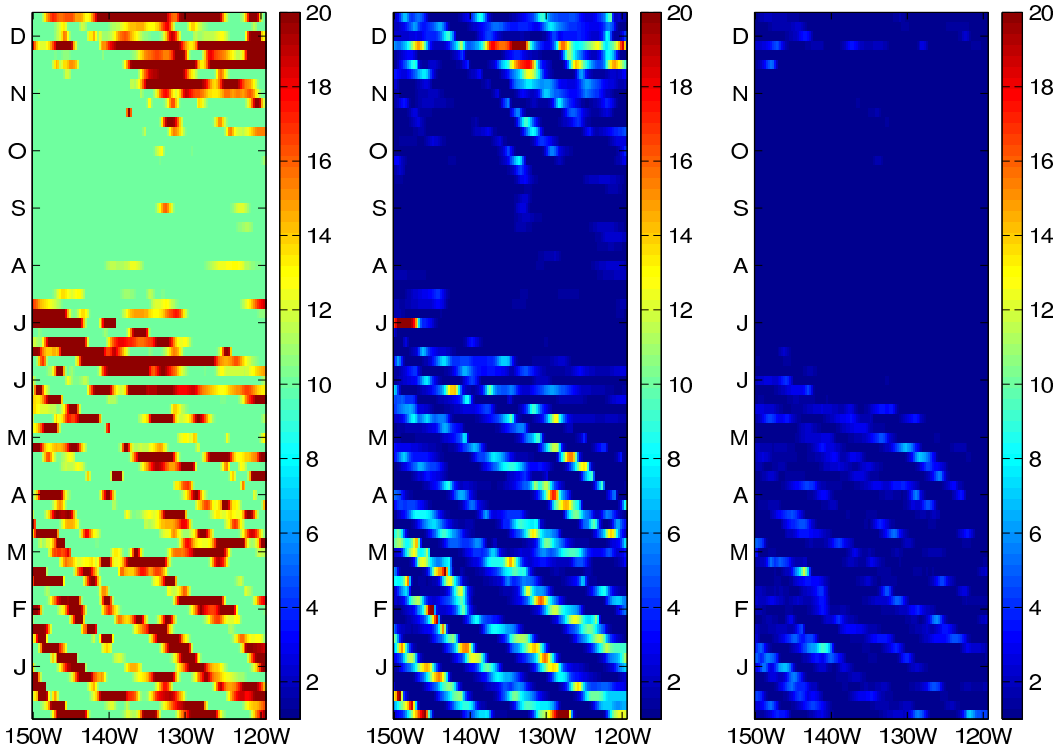

Figure 7.8: Coefficient of vertical diffusivity at 1N across the bottom of the first three levels of the model (20.00m, 41.20m and 63.95m). Units $cm^{-2}s^{-1}$.

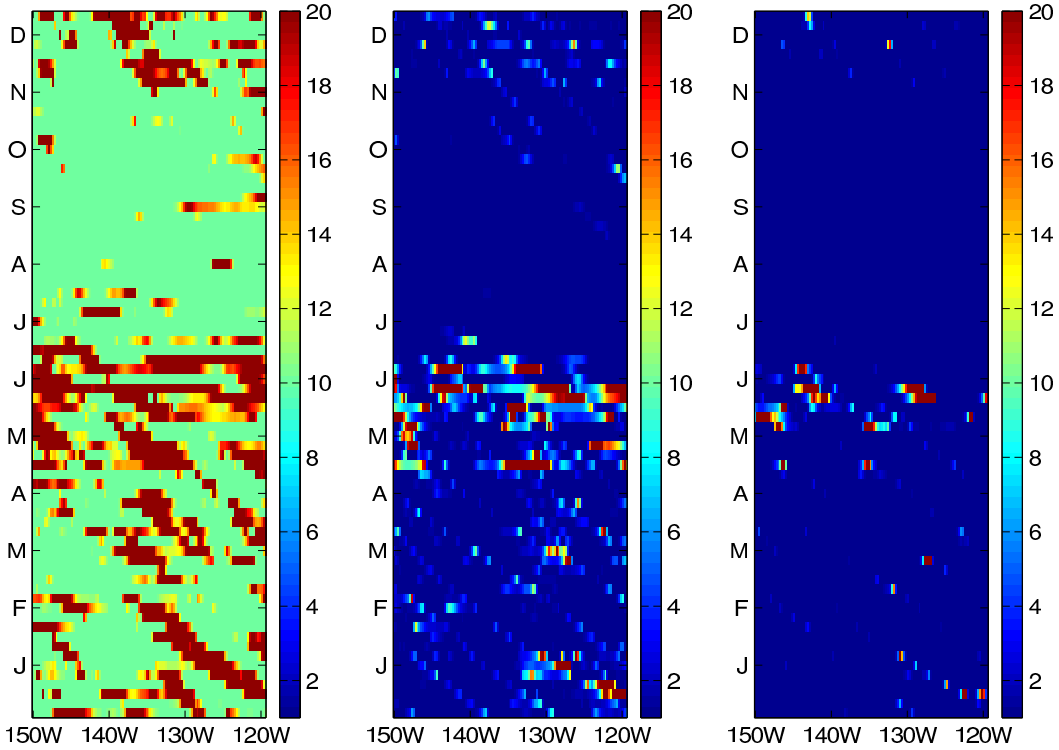

Figure 7.9: Coefficient of vertical diffusivity at 4N across the bottom of the first three levels of the model (20.00m, 41.20m and 63.95m). Units $cm^{-2}s^{-1}$.

year and at the end of the year. Figure 7.9 shows that at 4N there are further patchy events of high vertical coefficient mainly during May and June. The rest of the levels (not shown) have a negligible coefficient of vertical diffusivity.

7.2.4 Richardson number analysis

As shown in equation 7.3 the coefficient of vertical diffusivity depends on the Richardson number. Figures 7.10, 7.11 and 7.12 show the Richardson number at the bottom of the first three levels of the model at 1S, 1N and 4N respectively. The figures show the same patterns as those discussed for figures 7.7, 7.8 and 7.9, as small values in the Richardson number are associated to high values of the vertical diffusivity coefficient.

The Richardson number depends on the gradient of vertical temperature, velocity and salinity and can be expressed as:

$$R_i = \frac{-f}{\rho}\frac{\frac{\partial \rho}{\partial z}}{(\frac{\partial u}{\partial z})^2} = \frac{-g}{\rho}\frac{(\frac{\partial \rho}{\partial T}\frac{\partial T}{\partial z} + \frac{\partial \rho}{\partial S}\frac{\partial S}{\partial z})}{(\frac{\partial u}{\partial z})^2} \tag{7.4}$$

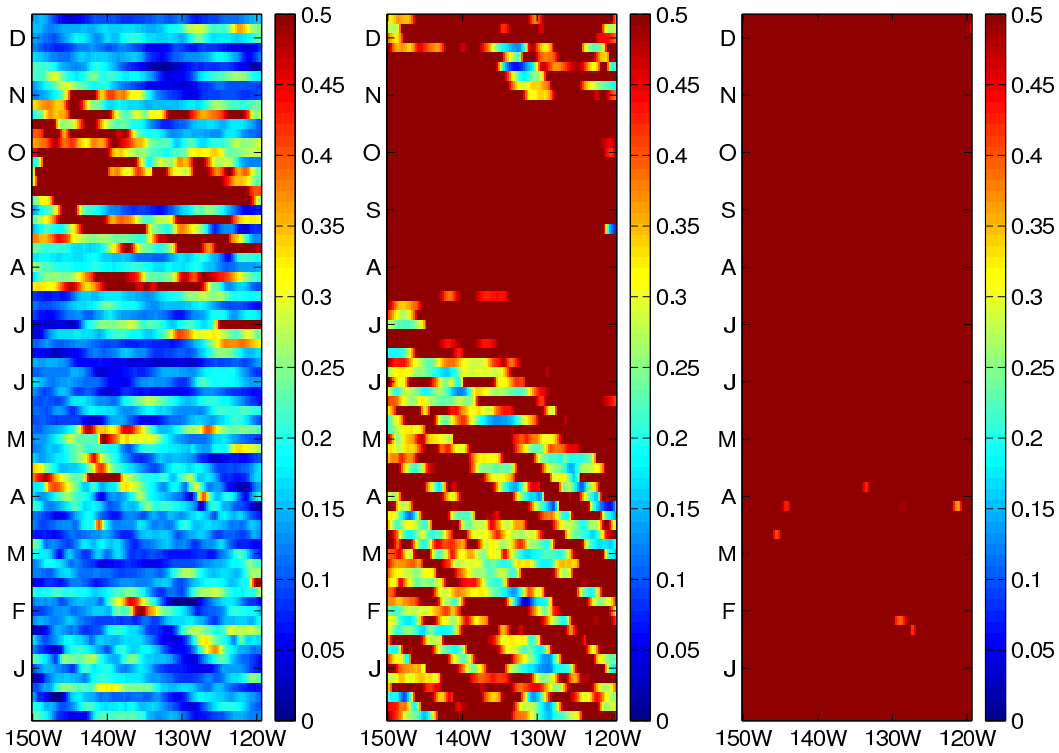

Figure 7.10: Richardson number at 1S across the bottom of the first three levels of the model (20.00m, 41.20m and 63.95m).

Considering $\frac{\partial S}{\partial z} \rightarrow 0$, equation 7.4 reduces to:

$$R_i = (\frac{-g}{\rho}\frac{\partial \rho}{\partial T})\frac{(\frac{\partial T}{\partial z})}{(\frac{\partial u}{\partial z})^2} \tag{7.5}$$

Within the model the coefficient $\frac{\partial \rho}{\partial T} \approx -0.2 \times 10^{-3}$, then the above equation just in terms of the gradients of temperature and velocity is:

$$R_i = C\frac{(\frac{\partial T}{\partial z})}{(\frac{\partial u}{\partial z})^2} \tag{7.6}$$

where $C = \frac{-g}{\rho}\frac{\partial \rho}{\partial T}$. A fluid with sufficiently large vertical shear will become unstable with respect of small wavelike perturbations. For instabilities to occur, the Richardson number must be less than 0.25 ($R_i < 0.25$). The above expression states that for high values of the vertical shear and small values of the gradient of temperature, instabilities occur and R_i is small.

Figures 7.13, 7.14 and 7.15 show the Hovmoller diagrams of the gradient of vertical velocity or vertical shear at 1S, 1N and 4N respectively, for the first six levels of the model, given by:

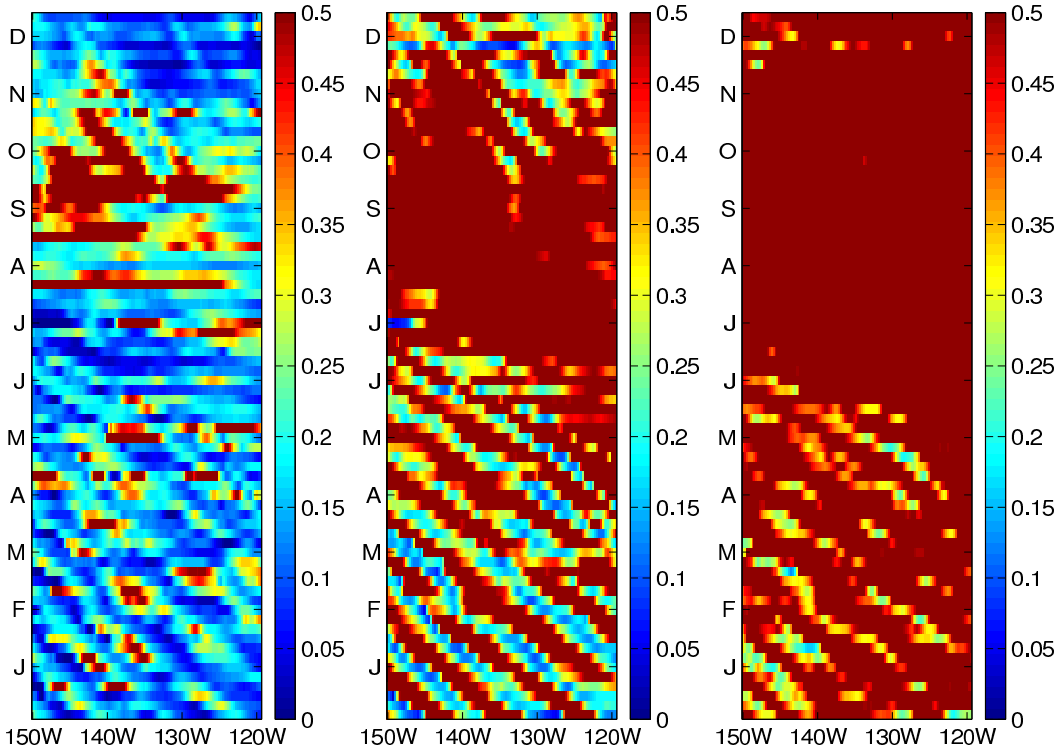

Figure 7.11: Richardson number at 1N across the bottom of the first three levels of the model (20.00m, 41.20m and 63.95m).

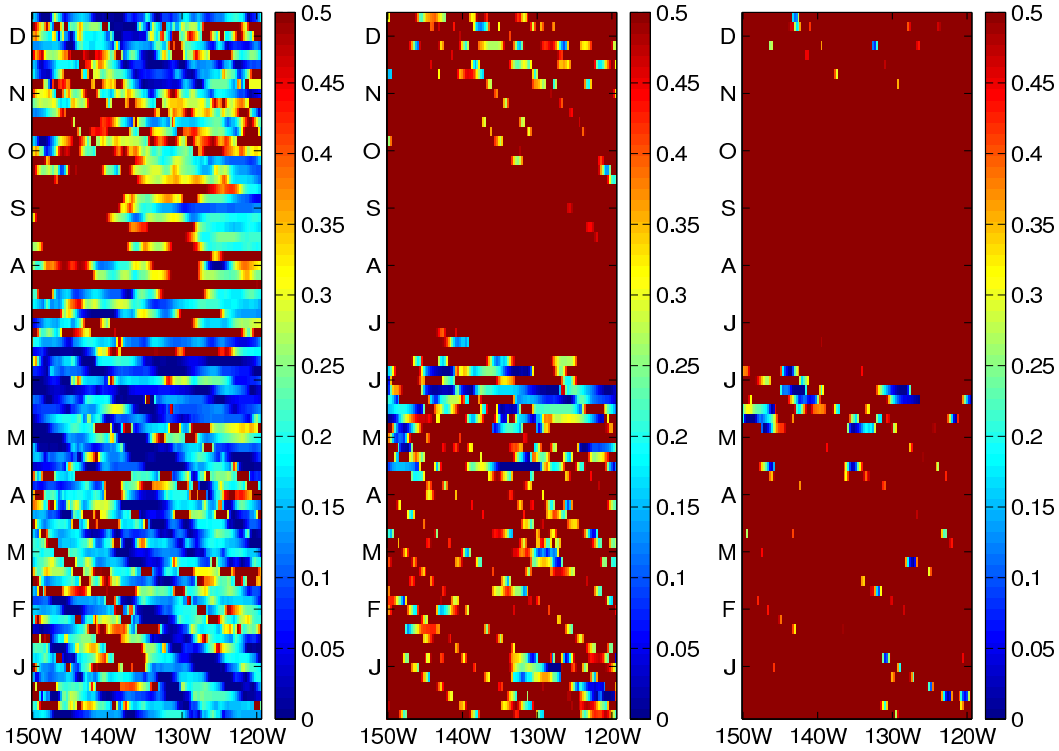

Figure 7.12: Richardson number at 4N across the bottom of the first three levels of the model (20.00m, 41.20m and 63.95m).

$$\frac{\Delta U_{ijk}^2}{\Delta z} = \frac{((u_{i,j,k} - u_{i,j,k+1})^2 + (v_{i,j,k} - v_{i,j,k+1})^2)}{z_{k+1} - z_k} \tag{7.7}$$

where u and v are the zonal and meridional components of the velocity defined at the centre of the model box.

The figures show high values of the vertical shear that propagate westward at the first three levels of the model. At the bottom of levels two and three the shear is high when the Richardson number is small (figures 7.10, 7.11 and 7.12). On the other hand, the Richardson number at the bottom of level one is small almost at all times. This suggests that even low values of shear at the bottom of level one are enough to generate mixing when the gradient of temperature tends to zero.

7.3 Discussion and conclusions

The above analysis shows that, within the model, there is a persistent westward wave propagation reflected mainly in the gradient of temperature and velocity and in the vertical diffusion. Such propagation is better seen at 4N and is characterised by a wavelength of 1000km and a period of three months during the first half of the year. Within the model, a cooling process brakes such propagation which lead to an stratified ocean during summer and beginning of autumn. The rest of the year presents further westward propagation mainly at 4N, which is associated to the TIWs.

In the model, at the latitudes under consideration, the main contribution to the vertical diffusion is due to the gradient of temperature below level one. At level one and during patchy events for the rest of the levels the vertical diffusion is generated by high values of the vertical shear, reflected in the Richardson number. The Richardson number analysis also shows that the small values of the vertical shear, at the bottom of level one, generate diffusion when the gradient of temperature is small.

Close to the equator, the mixed layer is deeper at 1S than at 1N. At the latter latitude the mixed layer shows a westward propagation at level two which may be associated with lateral mixing. At 4N the mixed layer has an stronger vertical variability, as it deepens from around 63.95m down to 116.09m during the first half of the year.

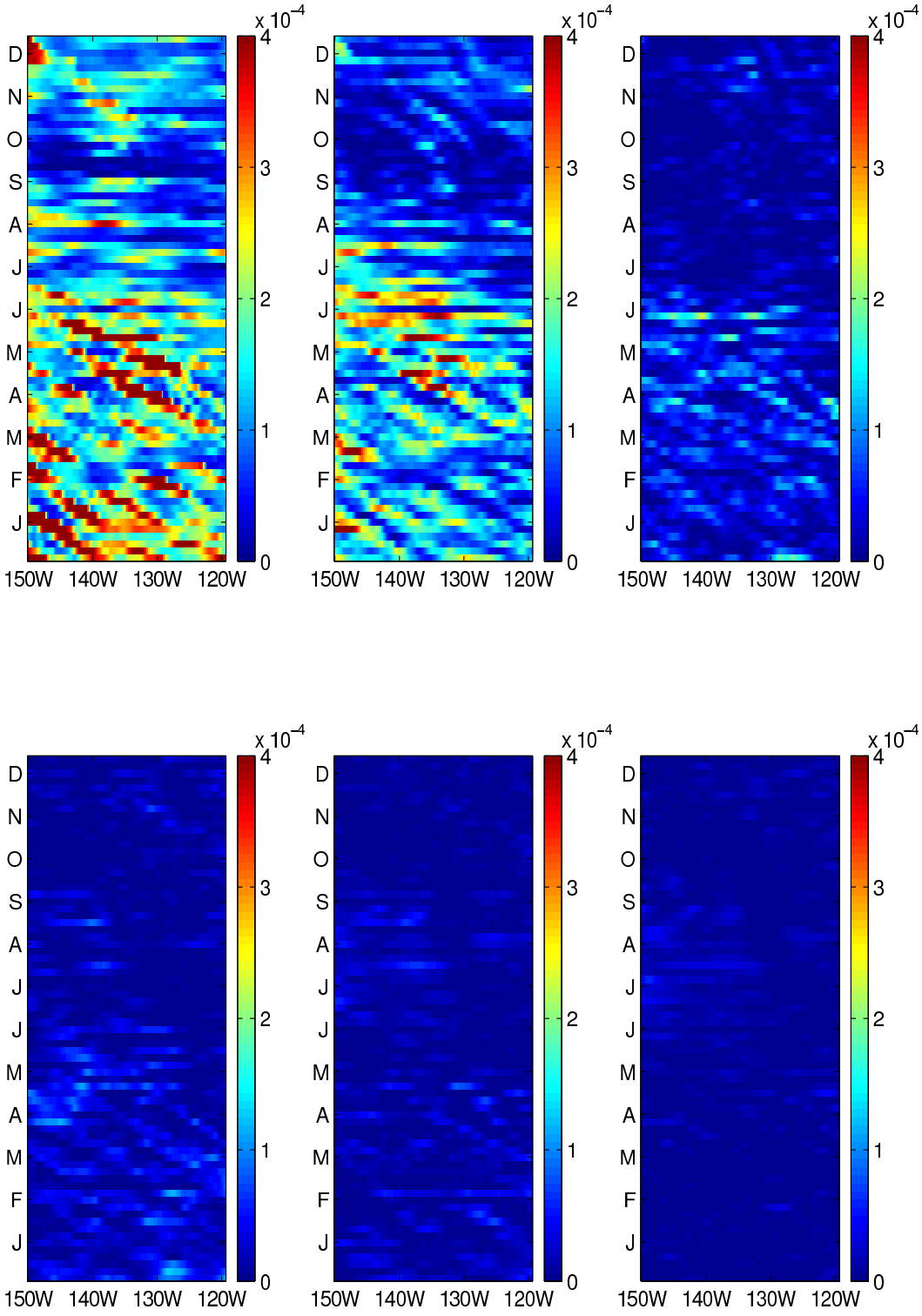

Figure 7.13: Gradient of velocity at 1S at the bottom of the first six levels of the model (20.00m, 41.20m, 63.95m, 88.72m, 116.09 and 146.79m, from top left to bottom right). Units $cm\,s^{-2}$.

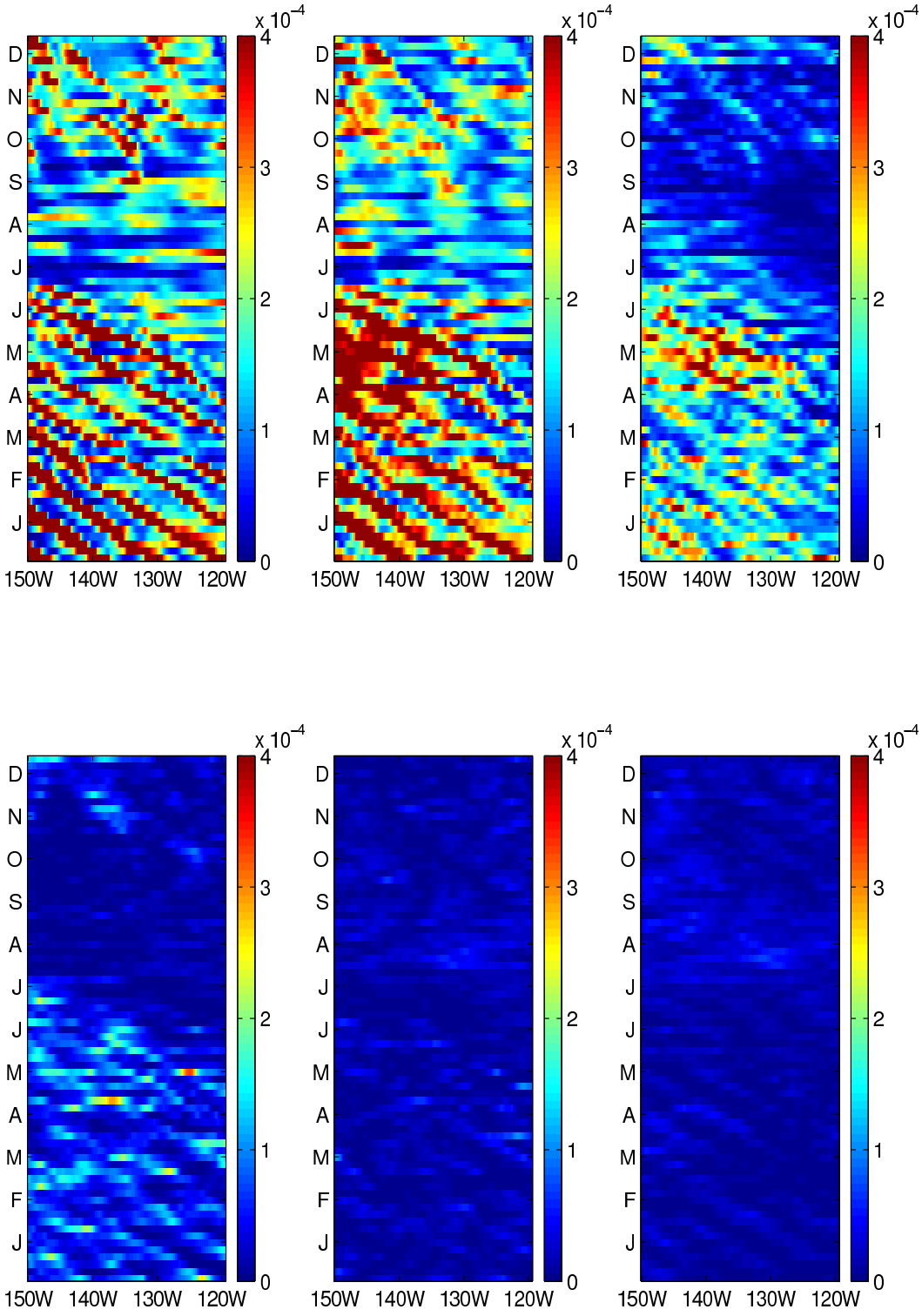

Figure 7.14: Gradient of velocity at 1N at the bottom of the first six levels of the model (20.00m, 41.20m, 63.95m, 88.72m, 116.09 and 146.79m, from top left to bottom right). Units $cm\,s^{-2}$.

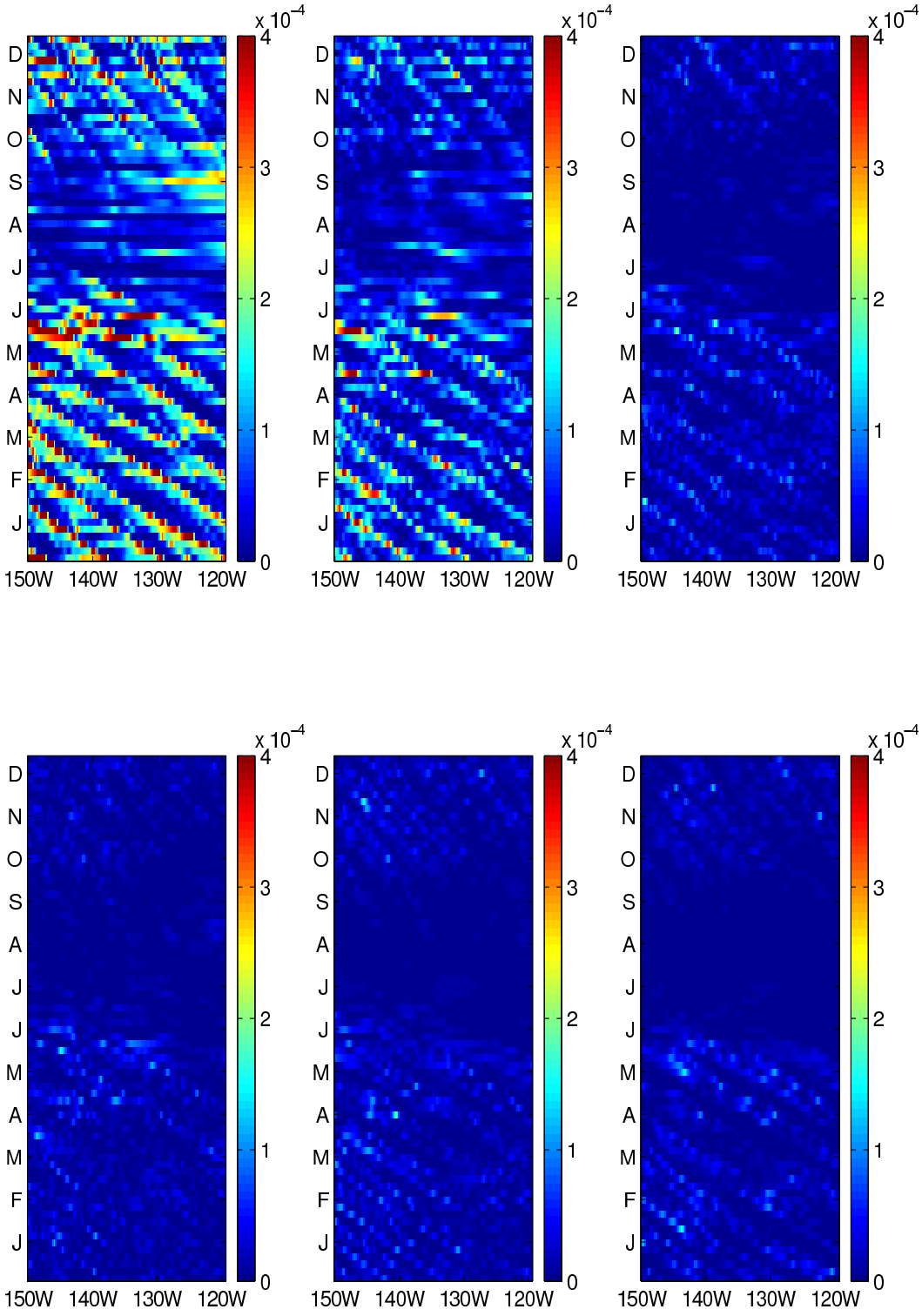

Figure 7.15: Gradient of velocity at 4N at the bottom of the first six levels of the model (20.00m, 41.20m, 63.95m, 88.72m, 116.09 and 146.79m, from top left to bottom right). Units $cm\,s^{-2}$.

Chapter 8

Conclusions

One of the main objectives of this thesis was to study the processes affecting the heat transport in the equatorial Pacific. To do this, I first described the mean circulation of the main equatorial current system in OCCAM.

Upwelling has been identified as a fundamental element of the circulation of the equatorial Pacific, which in OCCAM is around 38Sv across the bottom of level two (41.20m). This is in reasonable agreement with the figure found by Cromwell (1953), Knauss (1963) and Wyrtki (1981) of about 30-50Sv in the east-central Pacific. This upwelling, in the central and eastern equatorial Pacific, is the end result of the eastward and upward flow of the Equatorial Undercurrent across the equatorial Pacific as described by Bryden and Brady (1985). The region off the equator is characterized by downwelling, which is stronger in the central and eastern Pacific. Superimposed on this vertical circulation there is a meridional circulation, which at the surface is driven by poleward Ekman transport and below the influence of the wind is characterized by equatorial convergence.

An outstanding issue of this circulation is to quantify how much of the upwelling within the model is due to the upward sloping of the EUC and how much is due to the part of the meridional convergence that does not join the EUC. The main conclusion of this analysis is that the meridional convergence above the core of the EUC (levels three and four, 63.95m - 88.72m) in the Central Region sustains the EUC further east, whereas in the core of the current the upwelling is formed in part by the upward-sloping of the EUC and part by the meridional convergence. Below the core of the EUC the upwelling is entirely due to its tilt.

The vertical and meridional circulation form the Tropical Cells, which in the East Region recirculate around 80% of the downwelled water in both branches; in the Central

Region, the southern branch shows a strong recirculation of 100%, while the northern branch of the cell just recirculates 50%. The rest of the flow mainly joins the zonal currents.

The Tropical Cells in OCCAM show variability north and south of the equator. The northern branch shows downwelling concentrated in a region around 5N, while the southern branch shows constant downwelling from around 2S to 6S. This result is unexpected since previous analyses report almost symmetric branches. Such sharp downwelling at 5N, which is not entirely explained by Ekman convergence, suggests that terms such as friction, viscosity and pressure gradient in the equations of motion are important in controlling it within the model.

A further objective was to determine how well the OCCAM 5-day dataset captures the actual advective heat transport. The main finding of this analysis was that the use of the 5-day mean dataset generates a numerical error, which is associated with high frequency fluctuations with time scales less than 5 days. This error turned out to be an imbalance between the rate of change of heat content and the sum of heat due to advection and diffusion, in a closed region of the ocean. This term can represent an important contribution to the area-averaged heat balance analysis. However, it is small compared with the heat fluxes due to advection across each interface. This analysis allows an estiamtion of the individual heat fluxes. An important result is that, due to the high frequency term, errors can be large while working with mean datasets. This result from the model is certainly true for oceanic observations.

With all contributions to the heat transport described including the high frequency contribution, it is possible to investigate how much heat the main equatorial current system transports and which are the processes affecting it within OCCAM. As mentioned, regional the heat balance in OCCAM is affected by processes with time scales of less than 5-days, but it is still possible to study the individual components of the heat flux, because the high frquency fluxes are relatively small at each boundary. In particular, the Equatorial Undercurrent increases its temperature zonally due to vertical diffusive processes, but also due to meridional entrainment of heat due to advective mean heat flux, mainly due to the convergence of the Tropical Cells, and also from the fluctuations due to TIWs around the mean. As the Tropical Cells are part of a shallow circulation, the heat transport to deeper levels is mainly due to vertical diffusion.

On the other hand, the warm water that downwells off the equator mixes with the colder westward flow associated with the South Equatorial Current, decreasing its temperature as it joins the meridional convergence. The latter in general transports heat toward the equator.

The equatorward convergence of heat flux due to fluctuations persists at deeper levels in the Bottom Boxes studied. As the meridional convergence in these levels has weakened, the fluctuations can be due to the meandering of the currents. Vertical diffusion also contributes to the heat balance at these levels.

Vertical diffusion processes are an important component of the heat balance. Therefore, it is important to study how they vary throughout the year. An outstanding finding of this analysis is that the model shows instability processes during the first half of the year, which are mainly evident in the vertical gradients of temperature and velocity. Such instabilities have a higher frequency than the TIWs, which occur at the end of the year. Thus, this new instability is a different process from the TIWs and occurs at the a different time of the year.

Most of the time the vertical diffusion in the model is dominated by the gradient of temperature. However, there are patchy events in the top levels of the model, associated with small values of the Richardson number. The Richardson number analysis further shows that when the gradient of temperature tends to zero and the vertical shear has small values, mixing is generated within the model. The variation in depth of the mixed layer is strongly linked with the westward propagation of these gradients of temperature. The results here suggest that lateral mixing processes are occurring within the region.

This analysis shows that the balance of heat in a closed region of the ocean is restricted, not resolving the fluctuations with time scales of less than 5 days. Nevertheless, vertical diffusion and meridional fluctuations around the mean flow are the dominant processes that carry heat in the equatorial Pacific in the model. So a nearly complete analysis of the heat transport processes can still be made in the equatorial Pacific.

8.1 Future work

This work leaves several outstanding issues which need further consideration. The main ones are:

- In order to represent the heat flux through the surface into or out of the atmosphere in OCCAM, the temperature of the uppermost model layer is relaxed to the observed monthly mean Levitus et al. (1994) sea surface temperature. This work deals with the redistribution of heat within the model leaving out this term, which needs further consideration.

- It is unclear what mechanisms drive the instabilities during the first half of the year. For this, a study of the variability in time of the lateral mixing processes, the strength of the Tropical Cells and of the meridional advection must be made.
- To have a better insight of high frequency terms left out by the heat balance analysis, it is necessary to redo the analysis using instantaneous datasets. This would require storage of vast model data sets but the analysis done in this thesis could be done on such vast data sets in a straightforward manner.

Bibliography

Anderson, S. and Weller, R. A. (1996). Surface Buoyancy Forcing and the Mixed Layer of the Western Pacific Warm Pool: Observations and 1D Model Results. *Journal of Climate*, pages 3056–3085.

Arakawa, A. (1966). Computational design for long-term numerical integration of the equations of fluid motion: Two-dimensional incompressible flow. *J. Comput. Phys.*, 1:119–143.

Baturin, N. G. and Niiler, P. P. (1997). Effects of Instability Waves in the Mixed Layer of the Equatorial Pacific. *Journal of Geophysical Research*, 102:27771–27793.

Bjerknes, J. (1969). Atmospheric teleconnections from the equatorial Pacific. *Monthly Weather Review*, 97:163–172.

Bryan, K. (1969). A numerical method for the study of the circulation of the world ocean. *J. Comput. Phys.*, 4(3):347–376.

Bryden, H. L. and Brady, E. C. (1985). Diagnostic model of the three-dimensional circulation the upper equatorial Pacific Ocean. *Jorunal of Physical Oceanography*, 15:1255–1273.

Bryden, H. L. and Brady, E. C. (1989). Eddy momentum and Heat Fluxes and their effects on the circulation of the equatorial Pacific Ocean. *Journal of Marine Research*, 47:55–79.

Contreras, R. F. (2002). Long-term observations of Tropical Instability Waves. *Journal of Physical Oceanography*, 32:2715–2722.

Cox, M. D. (1984). A primitive equation 3-dimensional model of the ocean. Technical Report 1, GFDL Ocean Group Technical Report, Princeton Univ., Princeton, N.J. 08542, USA.

Crawford, W. R. and Osborn, T. R. (1979). Microestructure measurements in the Atlantic Equatorial Undercurrent during GATE. *Deep-Sea Res.*

Crawford, W. R. and Osborn, T. R. (1981). The control of equatorial ocean currents by turbulent dissipation. *Science.*

Cromwell, T. (1953). Circulation in a meridional plane in the central equatorial pacific.

Journal of Marine Research.

Cronin, M. and McPhaden, M. J. (1997). The upper ocean heat balance in the western equatorial Pacific warm pool during September-December 1992. *Journal of Geophysical Research*, (102):8533–8553.

Cronin, M. F., McPhaden, M. J., and Weisberg, R. H. (2000). Wind-forced reversing jets in the western equatorial Pacific. *Journal of Physical Oceanography.*

Delcroix, T., Eldin, G., McPhaden, M., and Moliere, A. (1993). Effects of Westerly Wind Bursts upon the Western Equatorial Pacific Ocean, February-April 1991. *Journal of Geophysical Research*, 98:16379–16385.

Feng, M., Hacker, P., and Lukas, R. (1998). Upper ocean heat and salt balance in response to a westerly wind burst in the western equatorial Pacific during TOGA COARE. *Journal of Geophysical Research*, 103(10289-10311).

Fine, R. (1983). Cross equatorial tracers transport in the upper waters of the Pacific Ocean. *Journal of Geophysical Research*, 88:763–769.

Flament, P. J., Kennan, S. C., Knox, R. A., Niiler, P. P., and Bernstein, R. L. (1996). The Three-Dimensional structure of an upper Ocean Vortex in the Tropical Pacific Ocean. *Nature*, 383:610–613.

Fofonoff, N. P. and Montgomery, R. B. (1955). The equatorial undercurrent in the light of the vorticity equation. *Tellus.*

Folland, C. K., Palmer, T. N., and Parker, D. E. (1986). Sahel rainfall and world-wide sea temperatures 1901-85. *Nature*, 320:602–607.

Gadgil, S., Joseph, P. V., and Joshi, N. V. (1984). Ocean-atmosphere coupling over monsoon regions. *Nature (London)*, 312:141–143.

Gargett, A. E. and Osborn, T. R. (1981). Small scale shear measurements during the fine and microstructure experiment. *Journal of Geophysical Research.*

Godfrey, J. S. and Lindstrom, E. J. (1989). The heat budget of the equatorial western Pacific surface mixed layer. *Journal of Geophysical Research*, 94:8007–8017.

Graham, N. E. and Barnett, T. P. (1987). Sea surface temperature, surface wind divergence and convection over tropical oceans. *Science*, 238:657–659.

Gregg, M. C. (1980). Temperature and salinity microstructure in the pacific equatorial undercurrent. *Journal of Physical Oceanography.*

Gregg, M. C. and Sanford, T. B. (1980). Signatures of mixing from the Bermuda Slope, the Sargasso Sea and the Gulf Stream. *Journal of Physical Oceanography.*

Griffies, S. M., Boning, C., Bryan, F., Chassignet, E., Gerdes, R., Hasumi, H., Hirst, A., Treguier, A., and Webb, D. (2000). Developments in ocean modelling. *Ocean Modelling.*

Hansen, D. V. and Paul, C. A. (1984). Genesis and effects of long waves in the equatorial Pacific. *Journal of Geophysical Research*, 89:10431–10440.

Hansen, D. V. and Paul, C. A. (1987). Vertical motion in the eastern equatorial Pacific inferred from drifting buoys. *Oceanol. Acta*, 6(27-32).

Harrison, D. E. (1984). The appearance of sustained equatorial surface westerlies during the 1982 Pacific warm event. *Science*, 224:1099–1102.

Harrison, D. E. and Giese, B. S. (1991). Episodes of surface westerly winds as observed from islands in the Western Tropical Pacific. *Journal of Geophysical Research*, 96:3221–3237.

Johnson, G. C. (2001). The Pacific Ocean subtropical cell surface limb. *Geophysical Research Letters*, 28(9):1771–1774.

Johnson, G. C. and McPhaden, M. (2001). Equatorial Pacific Ocean Horizontal Velocities, Divergence and Upwelling. *Journal of Physical Oceanography*, 31:839–849.

Keen, R. A. (1982). The role of cross-equatorial tropical cyclone pairs in the Southern Oscillation. *Monthly Weather Review*, 110:1405–1416.

Kennan, S. C. and Flament, P. J. (2000). Observations of a Tropical Instability Vortex. *Journal of Physical Research*, 30:2277–2301.

Killworth, P. D., Stainforth, D., Webb, D. J., and Paterson, S. M. (1991). The development of a free surface Bryan-Cox-Semtner ocean model. *Journal of Physical Oceanography*, 21:1333–1348.

Knauss, J. A. (1963). Equatorial current systems. *The Sea*.

Lau, K. M. and Chan, P. H. (1988). Intraseasonal and interannual variations of the tropical convection: A possible link between the 40-50 day oscillation and ENSO? *Journal of Atmospheric Sciences*, 45:506–521.

Leonard, B. P. (1979). A stable and accurate convection modelling procedure based on quadratic upstream interpolation. *Computer Methods in Applied mechanical Engineering*, 19:59–98.

Levitus, S. (1982). Climatological Atlas of the World Oceans. *NOAA professional Paper,Washington, D.C.*, page 173.

Levitus, S. and Boyer, T. P. (1994). World ocean altas 1994, temperature. *NOAA Atlas*, 4:177.

Levitus, S., Burgett, R., and Boyer, T. (1994). World Ocean Atlas 1994, Salinity. *NOAA Atlas*, 3:99.

Lu, P., McCreary Jr, P., and Klinger, B. (1998). Meridional Circulation Cells and the Source Waters of the Pacific Equatorial Undercurrent. *Journal of Physical Oceanography*, 28:62–84.

Lukas, R. and Lindstrom, E. (1991). The mixed layer in the western equatorial Pacific Ocean. *Journal of Geophysical Research*, 96:3343–3357.

Luther, D. S. and Johnson, E. S. (1990). Eddy energetics in the upper Equatorial Pacific during Hawaii-to-Tahiti Shuttle Experiment. *Journal of Physical Oceanography*, 20:913–944.

Ma, C. C., Mechoso, C. R., Robertson, A. W., and Arakawa, A. (1996). Peruvian stratocumulus clouds and the tropical Pacific circulation- a coupled ocean atmosphere GCM study. *Journal of Climate*, pages 1635–1645.

Madden, R. A. and Julian, P. R. (1971). Detection of a 40-50 day oscillation in the zonal wind in the Tropical Pacific. *Journal of Atmospheric Sciences*, 28:702–708.

Madden, R. A. and Julian, P. R. (1972). Description of global-scale circulation cells in the Tropics with a 40-50 day period. *Journal of Atmospheric Sciences*, 29:1109–1123.

McPhaden, M. J., Busalachi, A. J., Cheney, R., Donguy, J. R., Gage, K. S., Halpen, D., Ji, M., Julian, P., Meyers, G., Mitchum, G. T., P. P. Niiler, a. J. P., Reynolds, R. W., Smith, N., and Takeuchi, K. (1998). The Tropical Ocean-Global Atmosphere observing system: A decade of progress. *Journal of Geophysical Research*, 103:14169–14240.

Meehl, G. A. (1987). The annual cycle and interannual variability in the tropical Pacific and Indian Ocean regions. *Monthly Weather Review*, 115:27–50.

Merle, J., Rotschi, H., and Voituriez, B. (1969). Zonal circulation in the tropical western South Pacific at 170E. *Bull. Jpn. Soc. Fish. Oceanogr. Spec.*, pages 91–98.

Moura, A. D. and Shukla, J. (1981). On the Dynamics of Droughts in Northeast of Brazil: Observations, Theory and Numerical experiments with General Circulation Model. *Journal of Atmospheric Science*, 38:2653–2675.

Nakazawa, T. (1988). Tropical super clusters within intraseasonal variations over the western Pacific. *Journal of Meteorological Society of Japan*, 66:823–830.

Osborn, T. R. and Bolodean, L. E. (1980). Temperature microstructure in the Atlantic Equatorial Undercurrent. *Journal of Physical Oceanography*, 10:66–82.

Pacanowski, R. C. and Philander, S. G. (1981). Parameterization of vertical mixing in numerical models of tropical oceans. *Journal of Physical Oceanography*, 11:1443–1451.

Palmer, T. N. and Mansfield, D. A. (1984). Response of two atmospheric general circulation models to sea surface temperatures anomalies in the tropical east and west Pacific. *Nature*, 310:483–485.

Pezzi, L. P. and Cavalcanti, I. (2001). The relative importance of ENSO and Tropical Atlantic Sea Surface Temperatures Anomalies for Seasonal Precipitation over South

America: A Numerical Study. *Brazilian Journal of Geophysics*, 17:205–212.

Philander, S. G. H. (1976). Instabilities of zonal equatorial currents. I. *Journal of Geophysical Research*, 81(21):3725–3735.

Philander, S. G. H. (1985). El Niño and La Niña. *Journal of Atmospheic Sciences*, 42:2652–2662.

Philander, S. G. H. (1990). *El Niño, La Niña and the Southern Oscillation*. Academic Press.

Philander, S. G. H. (1992). Ocean-Atmosphere Interaction in the Tropics: A Review of Recent Theories and Models. *Journal of Applied Meteorology*, 31:938–945.

Philander, S. G. H., Gu, D., Halpern, D., Lambert, G., Lau, N. C., Li, T., and Pacanowski, R. C. (1996). Why the ITCZ is mostly north of the equator. *Journal of Climate*, 9:2958–2972.

Reynolds, R. W. and Smith, T. M. (1994). Improved global sea surface temperatures analysis using optimum interpolation. *Journal of Climate*, 7:929–948.

Richards, K. and Inall, M. E. (2000). The upper ocean heat content of the western equatorial Pacific: processes controlling its change during the Tropical Ocean-Global Atmosphere Coupled Ocean-Atmosphere Response Experiment. *Journal of Geophysical Research*, 105:19575–19590.

Robinson, A. R. (1966). An investigation into the wind as the cause of the Equatorial Undercurrent. *Journal of Marine Research*, 24:179–204.

Semtner, A. J. (1974). A general circulation model for the World Ocean. Technical Report 9, Department of Meteorology, University of California, Los Angeles.

Siefridt, L. and Barnier, B. (1993). Banque de Donees AVISO Vent/flux: Climatologie des Analyses de Surface du CEPMMT. Technical report, CEPMMT.

Slingo, J. M., Rowell, D. P., Sperber, K. R., and Nortley, F. (1999). On the predictability of the interannual behaviour of the Madden-Julian Oscillation and its relationship with El Niño. *Quart, J. Royal Meteorol. Soc.*, (125):583–609.

Sloyan, B., Johnson, G., and Kessler, W. (2003). The Pacific Cold Tongue: A Pathway for Interhemispheric Exchange. *Journal of Physical Oceanography*, 33:1027–1043.

Smyth, W. D., Hebert, D., and Moum, J. N. (1996a). Local ocean response to a multiphase westerly wind burst 1. Dynamic response. *J. Geophys. Res.*, 101:22495–22512.

Smyth, W. D., Hebert, D., and Moum, J. N. (1996b). Local ocean response to a multiphase westerly wind burst 2. Thermal and freshwater responses. *Journal of Geophysical Research*, 101:22513–22533.

Swenson, M. and Hansen, D. (1999). Tropical pacific ocean mixed layer heat budget: